

# Numerical modeling of cone cracking in ceramics via indentation

Ravi Shankar

Master of Science Thesis



# Numerical modeling of cone cracking in ceramics via indentation

MASTER OF SCIENCE THESIS

For the degree of Master of Science in Structural Engineering at Delft  
University of Technology

Ravi Shankar

12<sup>th</sup> April 2018

ifthenelse



Copyright © Computational Mechanics(CITG)  
All rights reserved.

DELFT UNIVERSITY OF TECHNOLOGY  
DEPARTMENT OF  
COMPUTATIONAL MECHANICS(CITG)

The undersigned hereby certify that they have read and recommend to the Faculty of  
Civil Engineering and Geosciences (CITG) for acceptance a thesis entitled

NUMERICAL MODELING OF CONE CRACKING IN CERAMICS VIA INDENTATION

by

RAVI SHANKAR

in partial fulfillment of the requirements for the degree of

MASTER OF SCIENCE STRUCTURAL ENGINEERING

Dated: 12<sup>th</sup> April 2018

Supervisor(s):

\_\_\_\_\_  
Prof.dr.ir. L.J. Sluys

\_\_\_\_\_  
Ir.Erik Simons

Reader(s):

\_\_\_\_\_  
Prof. Ir. J.M. Houben



---

# Table of Contents

<b>1</b>	<b>Introduction</b>	<b>1</b>
1-1	Historical Overview . . . . .	2
1-1-1	Armour Protection . . . . .	2
1-1-2	Molecular structure . . . . .	3
1-2	Cracking . . . . .	3
1-2-1	Types of cracking . . . . .	3
1-3	Material Modelling . . . . .	4
1-3-1	Micro-Mechanical Model . . . . .	4
1-3-2	Phenomenological damage model . . . . .	5
1-4	Conclusion and Problem Statement . . . . .	10
1-5	Research Objectives . . . . .	11
1-6	Outline of thesis . . . . .	11
<b>2</b>	<b>Standard Drucker Prager implementation</b>	<b>13</b>
2-1	Verification . . . . .	14
2-1-1	Softening . . . . .	15
2-1-2	Diltancy . . . . .	16
2-2	Validation . . . . .	17
2-3	Indentation . . . . .	19
2-3-1	Material Properties . . . . .	19
2-3-2	Mesh and Simulation Parameters . . . . .	20
2-3-3	Result . . . . .	22
2-3-4	Parameter study . . . . .	24
2-4	Conclusion . . . . .	36

<b>3</b>	<b>Pressure dependent softening</b>	<b>37</b>
3-1	Estimation of pressure - softening range . . . . .	37
3-2	DP Model modified for pressure dependent softening . . . . .	40
3-2-1	Yield function . . . . .	40
3-2-2	Plastic potential function . . . . .	41
3-2-3	Stress Integration . . . . .	41
3-2-4	Smooth return mapping formulation . . . . .	41
3-2-5	Consistent tangent matrix for smooth mapping return . . . . .	43
3-2-6	Apex return formulation . . . . .	44
3-2-7	Consistent tangent matrix for apex return . . . . .	45
3-3	Verification . . . . .	46
3-4	Indentation . . . . .	52
3-5	Conclusion . . . . .	55
<b>4</b>	<b>Modified Yield Function</b>	<b>57</b>
4-1	Yield function . . . . .	57
4-2	Verification . . . . .	59
4-2-1	Cohesion . . . . .	59
4-2-2	Angle of friction . . . . .	60
4-3	Yield Surface Comparison . . . . .	61
4-4	Indentation . . . . .	62
4-5	Conclusion . . . . .	63
<b>5</b>	<b>Mesh Sensitivity</b>	<b>65</b>
5-1	Viscoplasticity . . . . .	65
5-2	Integration of Viscoplasticity in DP Model . . . . .	65
5-3	Verification . . . . .	68
5-4	Indentation . . . . .	71
5-5	Conclusion . . . . .	72
<b>6</b>	<b>Conclusion and Recommendation</b>	<b>73</b>
6-1	Conclusion . . . . .	73
6-2	Recommendation . . . . .	74

---

# List of Figures

1-1	Cone crack under indentation[1]	1
1-2	Major types of cracking [2]	3
1-3	The inelastic mechanisms included in the constitutive model for. [3]	5
1-4	JH1 model[4]	7
1-5	JH2 model[4]	8
1-6	JHB model[4]	9
1-7	Outline of chapters	12
2-1	Drucker Prager Model - stress vs pressure	14
2-2	Unit test	15
2-3	Unit load test for varying Softening	16
2-4	Unit load test for varying angle of dilatancy	17
2-5	FEM mesh for Strip footing	17
2-6	Equivalent plastic strain for angle of friction ( $\phi = 30$ )	18
2-7	Load Displacement plot	19
2-8	Generic mesh for studying Indentation	20
2-9	Node to surface contact.[5].	21
2-10	Contact - Force application[5].	21
2-11	Contact - penetration[5].	22
2-12	Plastic strain for indentation in Alumina	22
2-13	Indentation depth - Crack Propagation	23
2-14	Converged State: Load Displacement Curve	24
2-15	Uni- Axial Strength for varying angle of friction ( $\phi$ )	25
2-16	Equivalent Plastic Strain with variation in $\phi$	26
2-17	Force v/s Displacement plots for varying angle of friction	27

2-18	Equivalent Plastic Strain for variation in dilatancy ( $\psi$ ) . . . . .	28
2-19	Force v/s Displacement plots for varying angle of dilatancy ( $\psi$ ) . . . . .	29
2-20	Equivalent Plastic Strain for variation in $\psi$ indentation depth of 25 $\mu\text{m}$ . . . . .	30
2-21	Equivalent Plastic Strain for variation in Softening at indentation depth of 25 $\mu\text{m}$ . . . . .	31
2-22	Maximum Equivalent Plastic Strain for variation in Softening at indentation depth of 40 $\mu\text{m}$ . . . . .	32
2-23	Force v/s Displacement plots for varying softening (h) . . . . .	32
2-24	Equivalent Plastic Strain with variation in confinement . . . . .	33
2-25	Force v/s Displacement plots for varying degree of confinement . . . . .	34
2-26	Equivalent Plastic Strain with variation in Mesh Size . . . . .	35
2-27	Force v/s Displacement plots for varying mesh size . . . . .	36
3-1	Softening modulus variation with pressure . . . . .	39
3-2	Softening modulus variation with pressure - zoomed . . . . .	39
3-3	Euler backward return[6] . . . . .	42
3-4	Apex return for Drucker Prager model [7] . . . . .	44
3-5	Cubic Polynomial function for pressure dependent strength . . . . .	46
3-6	Cubic Polynomial function for pressure dependent strength . . . . .	47
3-7	softening modulus vs pressure for Case 2 . . . . .	49
3-8	softening modulus vs pressure for Case 3 . . . . .	49
3-9	Equivalent stress vs pressure . . . . .	50
3-10	Equivalent stress vs pressure . . . . .	50
3-11	Load v/s Displacement . . . . .	51
3-12	Equivalent Plastic Strain to variable softening - Indentation depth 25 $\mu\text{m}$ . . . . .	52
3-13	Equivalent Plastic Strain to variable softening - Indentation depth 40 $\mu\text{m}$ . . . . .	53
3-14	Force v/s Displacement plots for varying softening (h) . . . . .	53
3-15	Equivalent Plastic Strain at Indentation depth 40 $\mu\text{m}$ . . . . .	55
4-1	Modified Yield function . . . . .	58
4-2	Original JHC model with Walker and Anderson failure surface [8] . . . . .	58
4-3	Unit load test on single cell (1 integration point) for varying cohesion and zero softening . . . . .	59
4-4	Unit load test for varying angle of friction( $\phi$ ) . . . . .	61
4-5	Yield function comparison between Literature and simulation[9] . . . . .	61
4-6	Indentation with varying softening for the modified yield surface DP(2) . . . . .	62
4-7	Indentation with varying softening for the modified yield surface DP(1) . . . . .	63
5-1	Mesh for bar in tension . . . . .	68
5-2	plastic strain for tension bar with standard DP model . . . . .	68
5-3	Plastic strain variation along the length of tension bar . . . . .	69

---

5-4	plastic strain for tension bar with standard DP model . . . . .	70
5-5	Max plastic strain along the height of bar. . . . .	70
5-6	plastic strain for variation in mesh size . . . . .	71
5-7	plastic strain for variation in mesh size with 40 divisions . . . . .	72



---

## List of Tables

2-1	Mechanical Properties . . . . .	19
2-2	Computation time variation with mesh size . . . . .	34
3-1	Co-efficient for cubic polynomial . . . . .	48
3-2	Comparative details of cone cracks for constant and pressure dependent softening	54



---

# Acknowledgement

The completion of this challenging project as my master thesis would not have been possible without some external support. I would like to express my deepest gratitude to my supervisor, dr.ir. Bert Sluys for providing me the opportunity to work on this research topic. I would also like to thank him for his continuous support and guidance throughout the project.

I would extend my gratitude to ir. Erik Simons my daily supervisor for his invaluable comments and guidance throughout the project which helped me to improve my work. Finally, I would like to express my deepest gratitude and love towards my family and friends for providing unconditional support, love, and having faith in me.

Delft University of Technology  
12<sup>th</sup> April 2018

Ravi Shankar



---

# Abstract

Ceramic is a hard and brittle material with little ductility. It has wide applications in diverse industries viz. metallurgy, atomic energy, electronics, communication, space, military, insulation, biomechanical appliances etc. It is preferred material for armour protection due to its high strength-weight ratio. Its plastic deformation and failure behavior have, therefore, become a subject of extensive research in the recent past. Consequently, several material models were formulated in the second half of the nineteenth century by researchers such as Johnson- Holmquist, Rajendran-Grove, Deshpande-Evans etc. to study ceramic response under high-velocity impact. But these models are complex and require extensive calibration, while the Drucker-Prager (DP) Model is easy to implement. It was developed for study in soil and rock and is chosen to analyze ceramic quasi-plastic and tensile behaviour as part of research through the current thesis.

Tensile ring and cone cracks, first observed by Hertz, are one of the modes of failure in brittle materials like ceramic. The prime objective of the thesis is the study of ceramic failure as well as cone crack initiation and its propagation through the ceramic body under the influence of varying material parameters such as cohesion, friction angle, dilatancy and softening of ceramics besides confinement by indentation. The Drucker Prager model is employed to study indentation by simulation through numerical methods in JEM JIVE FEM library. Verification of the model was done through simulation of unit cubes subjected to unidirectional stresses at prescribed displacements. Suitable modification for pressure dependent softening behaviour of the ceramic is also made into the model and simulations undertaken in order to get insight into the nonlinear strength degradation of the ceramic post-elastic limit. Since the DP criterion tends to overestimate material strength, a suitable mechanism to limit the material strength is integrated with DP yield function and also to facilitate the comparison of results arrived through DP and modified yield functions.

The results obtained by a simulated indentation in accordance with the DP formulation suggest that ceramic having high dilatancy, low friction angle and small softening modulus under confined conditions is more suited for use as armor protection. The pressure dependent softening behavior of ceramic is favorable for it being a good armor protection material. The DP Yield function modified to limit the material strength to a finite value, did not have any significant impact on crack initiation though the zone of compressive plastic strain grew

in size during indentation. The DP based numerical model suffered from mesh sensitivity. The introduction of viscoplasticity to the numerical model was observed to have a positive influence in mitigating mesh sensitivity.

---

# Glossary

## List of Symbols

### Abbreviations

$\delta, \Delta$	deflection
$\dot{\epsilon}$	strain rate
$\epsilon$	strain
$\epsilon_p$	plastic strain
$\epsilon_e$	elastic strain
$\lambda$	plastic multiplier
$\mu$	coefficient of viscoplasticity
$\nu$	poisson's ratio
$\Phi$	damage
$\phi$	angle of friction
$\psi$	angle of dilatancy
$\sigma$	stress
$\sigma_1, \sigma_2$	components of stress
$\sigma_f$	failed strength
$\sigma_i$	intact strength
$\sigma_{eq}$	equivalent stress
$c$	shear strength
$c'$	cohesion
$C_{ct}$	consistent tangent matrix
$C_{shear}$	velocity of shear wave

$D$	stiffness matrix
$f$	yield function
$G$	shear modulus
$g$	plastic potential
$h$	softening
$I$	identity matrix
$K$	bulk modulus
$p$	pressure
$P_{HEL}$	hugonit elastic limit
$p_{lim}$	limiting pressure
$T$	maximum permissible tensile pressure
$t, \Delta t$	time, increment in time
$Y, \sigma_y$	strength of material

---

# Chapter 1

---

## Introduction

Besides its application in diverse fields, ceramic is being used increasingly for armour protection since the 1970s due to its high hardness and toughness. The key to the development of effective ceramic protective cover lies in understanding its failure mechanism. The cracking is one of the common modes of failure of ceramic. The crack types are discussed in detail in section 1-2. A cone of fracture with radial and circumferential cracks occurs, when ceramic is subjected to the impact by high-velocity projectiles[10], [11]. Cone cracking is chosen for study via indentation through numerical modelling in the current thesis works. It was first observed by Hertz a century ago in glass lenses. Hertzian fracture starts as a surface ring, which develops into a truncated cone as it propagates downward and flares outwards as shown in Figure 1-1.

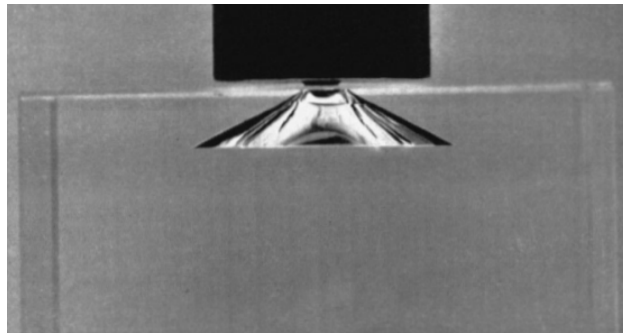


**Figure 1-1:** Cone crack under indentation[1]

Impact and indentation are the common methods to study failure mechanism of ceramic. It is difficult to measure stress, strain etc. accurately to determine damages in impact experiments conducted in the laboratory. Indentation is a relatively simple test. It is also less time consuming and cost-effective. The other major advantage of indentation over impact test is its flexibility in controlling the test conditions. The failed material can also be easily recovered in an indentation test [12]. Numerical simulation with the advent of powerful and high-speed computers has become an important tool to investigate ceramic failure subjected

to indentation. It has allowed integration of larger numbers of variables and parameters into the indentation process for a more insightful study. Simulated indentation by numerical methods is used in the current studies to get insight into cone cracking and to investigate the effect of key parameters such as internal friction, dilatancy and softening on the ceramic failure by cone cracking during indentation.

The current chapter introduces a historical overview of ceramics, molecular structure and crack types in brief. It is followed by a detailed section on popular computational models currently used to simulate ceramic failure and discussions on the selection of an appropriate model for present studies. Lastly, the research objectives of the thesis are laid out.

## 1-1 Historical Overview

Humans have been using ceramic potteries since Neolithic times. The word ceramic' has its origin in Greek word Keramikos' meaning of pottery' or for pottery.' Figurines and potteries, dating back to 24000 BC made of clay and burnt in kilns, have been found at the sites of old Eurasian civilizations [13]. The use of ceramic diversified from simple pottery in ancient times to bricks, tiles, porcelain, refractory lining etc. by medieval times. The heat resistant ceramic as refractory lining had made possible a quantum jumps for the growth of metallurgy; one of the key factors which kick-started the industrial revolution. The second half of the twentieth century saw rapid growth in ceramic technology and ceramic use in diverse fields such as atomic energy, electronics, communication, space travel, military, electrical and thermal insulators, semiconductor, superconductivity and biomechanical appliances [14].

Ceramic as an armor protection was discovered in 1918 by Major NM Hopkins [13]. But the discovery was not put to any practical application till the 1950s. The erstwhile Soviet Union developed the first armor made of ceramic mixed silicon oxide. Subsequently, the British, US and Germans developed new ceramic armours during the 1970s and 1980s and these are used in several modern-day tanks. The interest in advance research for newer ceramic armour technology has not abated in the present days.

### 1-1-1 Armour Protection

The armour industry extensively uses ceramics for protection against bullets and projectiles. Ceramic is a hard and brittle material with little ductility, exhibiting much higher compressive strength than tensile strength. Its hardness makes it attractive for amour protection. Ceramic provides effective resistance to penetration by high-speed ammunition warheads by absorbing substantial projectile energy and thereby acting as a front-line defence to the back plates, placed behind the ceramic protective layer. Since ceramics are lightweight in comparison to the traditional armour plates, the ceramic coating facilitates a reduction in back plate thickness i.e. the weight of armoured vehicles also gets reduced considerably resulting in the higher manoeuvrability of armoured platforms at less cost. The use of ceramics for armour started in the 1970's by the US military. The ceramic is also widely used as a substitute of steel for the protection of helicopters and armed personal against bullets, mortar etc. [8]. New generation ceramic armour have curved profiles to provide a snug fit around the body. To achieve capability against multiple projectiles hits, the designers started moulding ceramics

into 50 x 50 mm or 100 x 100 mm tiles woven in a matrix of carbon composite and fibres like Kevlar. During late 1980's tank armour was made from curved profiles of multiple sheets of ceramic stacked on the back of steel plate.

### 1-1-2 Molecular structure

The ceramics used in armour are Boron carbide ( $B_4C$ ), Silicon Carbide ( $SiC$ ), Silicon Nitride ( $SiN$ ), Alumina ( $Al_2O_3$ ) and Alumina Nitride ( $AlN$ ). These have crystalline or amorphous structure. The bonds in ceramic are of either ionic or covalent in nature. These bonds are very strong under compression making ceramic very hard and rendering it with large compressive strength. However, the molecular structure tends to become unstable and fractures rapidly under tensile load at very low deformation making the material brittle and prone to cracking.

## 1-2 Cracking

Brittle materials develop cracks in tension inhomogeneities in the form of small and micro-cracks culminating in complete failure of the material. Cracks are classified as inter-granular and trans-granular. The major factors affecting growth and propagation of cracks are loading rate, the degree of confinement and the geometry of projectile. Indentation and other impact tests produce five major types of cracks [15] as shown in the Figure 1-2 and explained below:

### 1-2-1 Types of cracking

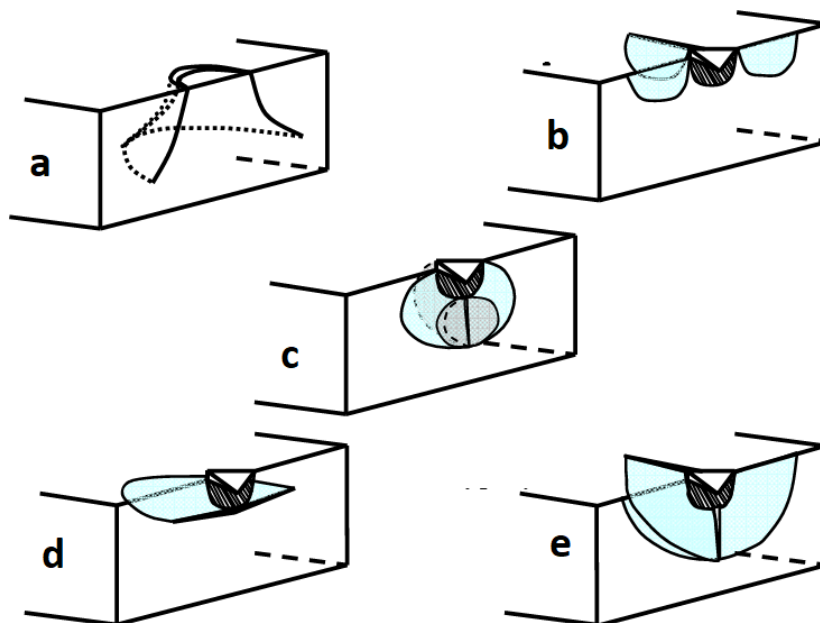


Figure 1-2: Major types of cracking [2]

1. Cone cracks: These were first observed by Hertz in glass on indentation by spherical glass balls in late nineteenth century. They develop in ceramics when indented by spherical or flat punch type indenter. The deformation in the material forms cone cracks. Ring cracks are formed in the tension zone near the edge of contact. On further loading, ring cracks propagate along the line of maximum tensile stress into cone cracks as shown in Figure 1-2a.
2. Palmquist / Radial cracks: Indentation by sharp or blunt indentors beyond Hertzian regime tend to produce radial crack (Figure 1-2b) in materials harder than glass like carbides and Zircona. Indenter forms impression on the ceramic due to the plastic flow induced by tensile hoop stress. The radial crack propagates parallel to the axis of the load from the edge of zone of the plastic flow under the indenter.
3. Median cracks: Wedging action of the pyramidal indenter creates plastic deformation zone. Median cracks (Figure 1-2c) develop below this plastic deformation zone and run parallel along the axis of loading.
4. Lateral cracks: These cracks mostly occur during unloading, although in some cases they are found in the loading as well as the cyclic loading cycles. They propagate due to post indentation residual stresses. They are located beneath the plastic deformation zone and propagate almost parallel to surface of loading as shown in Figure 1-2d and are followed by an upward turn, chipping the surface in the process.
5. Half penny cracks: These cracks (Figure 1-2e) start either from a radial crack, moving downward or from a median crack moving upward or a mixture in between the two. This type of crack occurs mostly during unloading.

## 1-3 Material Modelling

A material model incorporates failure mechanism and predicts the response of a body under external loads. The material response, which is a function of its microstructure and macro-mechanical properties, is defined by stress-strain constitutive relationships. The magnitude, direction and distribution of stress and strain tensors within a body are influenced by these properties and can be determined both analytically and through experiments such as triaxial tests. The multiplicity of material properties and heterogeneous nature of real material due to manufacturing defects make the process of understanding of material response rather complex [4]. The residual strength post material failure adds another dimension to this problem [3]. Therefore, the models have been developed on few simplifying assumptions made on the basis of the specific objectives of problem-solving. Consequently, the predictions of material response by models need to be in conformity with the experimental results. There are two types of dynamic constitutive models for ceramic [3] 1. Micro-mechanical model: 2. Phenomenological damage model.

### 1-3-1 Micro-Mechanical Model

The mechanical properties such as elasticity, plasticity, brittleness etc. are intricately related with the molecular structures and lattice arrangement, chemical bond strength and type etc.,

which have a direct bearing on the standard properties such as grain size, toughness and hardness. The micromechanical models incorporate micro properties for understanding the elastic and plastic deformation of the material under influence of load. The stress-strain relationship is indirect output to changes into a deforming material occurring at microstructure level. They provide insight into the deformation phenomena and are affected little by the boundary conditions as they are based on the basic natural laws which are universal. They are not very popular due to their large computational costs [3]. Deshpande-Evans (DE) Model described below is a micro-mechanically motivated type.

### Deshpande and Evans (DE) Model

The behaviour of ceramic while undergoing plastic deformation is influenced by three separate mechanisms at the micro level as shown in Figure 1-3 [3]. These are lattice plasticity, microcracking and granular plasticity. They happen to occur both simultaneously as well as one after the other in that order in parts. The damage to the material is considered to be complete when the material becomes granular under the combined influences of all three. The physical laws governing these mechanisms plus elasticity are integrated together to form the constitutive DE model. The results of indentation tests on armour grade alumina, when compared results of simulation of DE model reveal that the latter predicts larger damage and surface uplift than the actual obtained by experiments.

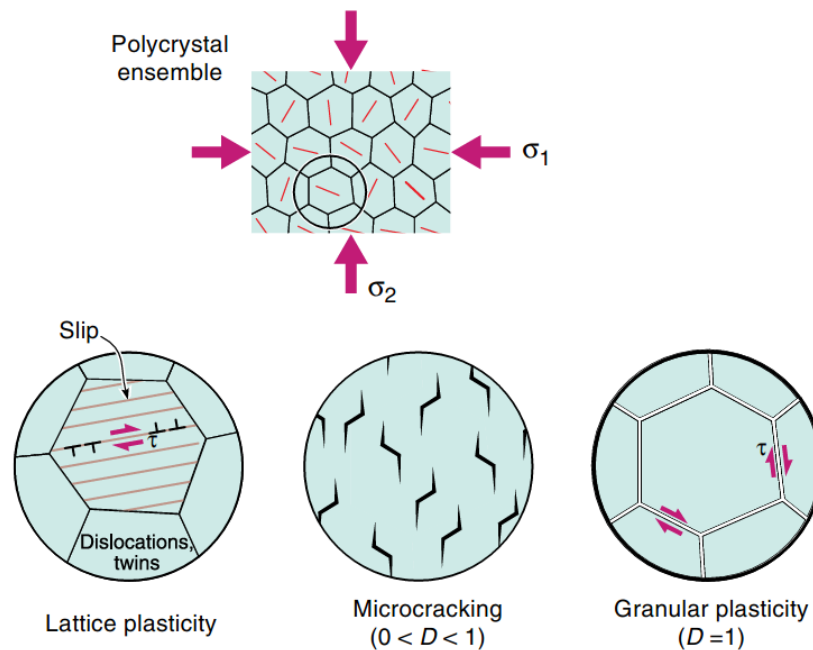


**Figure 1-3:** The inelastic mechanisms included in the constitutive model for. [3]

### 1-3-2 Phenomenological damage model

The constitutive relationships governing phenomenological models are empirical but are consistent with the fundamental laws associated with specific phenomena defined by such rela-

tionships. These are not derived from first principles of natural science unlike the constitutive relationships of micromechanical models. The manner in which the variables considered in such models interact is not explained fully but the model gives outputs consistent with experimental data. Like the micromechanical models, the constitutive relationships governing phenomenological models also have several coefficients and constants which are determined through the painstaking calibration process. Separate boundary condition or protocol requires separate calibration as the constitutive relationships do not factor material microstructure. Therefore, the results obtained from phenomenological damage models for one protocol often fail to predict the results for the other unless recalibrated for the changed scenario. This is its main drawback. But they are economical for large-scale computation. Models proposed by Johnson-Holmquist, Wilkins, Walker-Anderson etc. are among the more widely used models for ceramic study in this class

### Wilkins and Anderson Ceramic Model:

Wilkins developed his model with an emphasis to study the development of conoids in thin sheets of ceramics. According to his tensile failure model, fracture in the computation cell occurs when the maximum principal stress of a cell exceeds the tensile stress criterion ( $\sigma > \sigma_f$ ) [8]. The fracture propagates at some fraction of the wave speed from the surface (including material interface), weakening the cell pressure up to the complete fracture of the cell. Fracture then propagates to the neighbouring cell on the computational grid like a crack.  $\Psi$  denotes the damage and has a value of 0 (no damage) to 1 (complete damage). In terms of time steps fracture is complete at:

$$\Phi_f^{n+1} \approx \Phi_f^n + \Delta\Phi_f \quad \Phi_f^{n+1} = 1, \quad (1-1)$$

where

$$\Psi_f \approx f_i \frac{C_{shear} \Delta t^n}{X} \quad 0 \leq f \leq 1,$$

and

$$C_{shear} = \sqrt{\frac{G}{\rho}} \text{ - shear wave speed,}$$

where  $C_{shear}$  is the shear velocity of wave in material,  $\Phi$  is the damage and  $t$  denotes the time.  $X$  is the characteristic length of the cell. The progressive softening of the cell is given by  $Y = (1-\Phi)Y_{intact}$ . The Wilkins model does not account for the strength of the powdered ceramic. In 1991, Walker and Anderson improved the Wilkins model by incorporating the Drucker Prager model, characterising a slope  $\beta$  and a cap  $\bar{Y}$ .

$$Y = (1 - \Phi_f) Y_{intact} + \Phi_f Y_{fail}, \quad (1-2)$$

where the failed strength is defined as

$$Y_{fail} = \begin{cases} 0 & \text{for } P < 0 \\ \beta P & \text{for } 0 \leq P \leq \bar{Y}/b \\ \bar{Y} & \text{for } P \leq \bar{Y}b \end{cases}$$

The main drawback of the model is that it does not provide good estimate about the residual projectile length, dwell and residual velocities even for the over matched conditions.

### Johnson Holmquist Model

The JH model was developed as a part of the heavy armour research initiative at DARPA, USA. Since then, it is widely used for ceramic materials in the armour and ballistic research field [8]. Johnson and Holmquist developed the model by observing the response of ceramic impacted by high velocity penetrators. Failure is measured in terms of plastic accumulated plastic strain, represented by a damage variable  $D$ .

JH models use multiple curves to depict intact ( $D < 0.0$ ), failed ( $D=1.0$ ) and intermediate ( $0.0 < D < 1.0$ ) state of material. The JH2 model gradually softened the strength curves as damage accumulates.

### JH 1 model

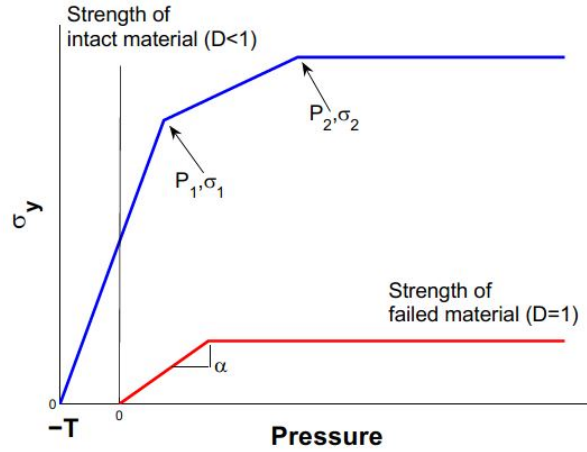


Figure 1-4: JH1 model[4]

Intact and failed strength, and the transition between them are quantified by damage accumulation, and are functions of pressure [16]. The intact strength and failed strength are shown in red and blue lines in the Figure 1-4. The available strength is defined as

$$\sigma = \sigma_o (1 + C3 \ln \dot{\epsilon}^*) \quad (1-3)$$

where  $C3$  is the strain rate constant. The damage ( $D$ ) is expressed as

$$D = \Sigma \frac{\Delta \epsilon^P}{\epsilon_f^P} \quad (1-4)$$

where  $\epsilon^P$  is the plastic strain during a cycle of integration and  $\epsilon_f^P$  is the plastic strain for fracture under a constant pressure. Figure 1-4 shows the maximum permissible hydrostatic tension as  $T$ . The hydrostatic pressure prior to fracture is

$$P = K1\mu + k2\mu^2 + k3\mu^3 + \Delta P \quad (1-5)$$

where,  $K1$ ,  $K2$  and  $K3$  are material constants and  $\mu = \rho/\rho_o - 1$  for current density  $\rho$  and initial density  $\rho_o$ . At fracture ( $D=1$ ) an additional term is added to pressure to account for the bulking. Bulking increases the volumetric strain and hence pressure. The increase in pressure is denoted by  $\Delta P$

$$\Delta P = -K1\mu_f + \sqrt{(K1\mu_f)^2 + 2.\beta K1\Delta U} \quad (1-6)$$

where  $\beta$  accounts for the effect of bulking,  $\Delta U$  is the loss of elastic energy and  $\mu_f$  is the final density of the failed material.

Drawbacks: A brittle material like Boron Carbide shows gradual softening during flyer plate impact tests. However, JH 1 model considers the damage to be invariant with respect to pressure as shown in Figure 1-4. The material has zero softening until  $D = 1$ , and then instantaneously softens. Furthermore, results are very sensitive to constants used in the model. The constants are also difficult to evaluate. The implementation of the JH model is tricky due to the jump condition between fractured and intact material. Eventually, JH 1 model was superseded by the JH 2 model to overcome its downsides.

## JH2 model

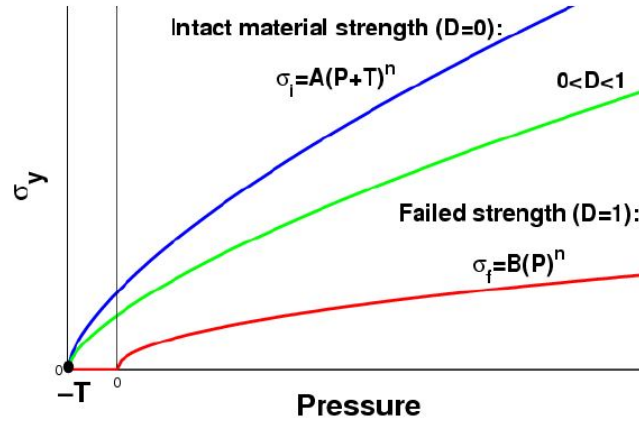


Figure 1-5: JH2 model[4]

The Figure 1-5 shows the available strength in the material with the accumulation of damage. The material gradually softens with the accumulation of damage [16]. The damage is a function of the increasing plastic strain. The blue line shows the intact strength ( $D=0$ ), while the red line shows the failed strength at ( $D=1$ ), and the green line shows the available strength in the material at an intermediate damage ( $0 < D < 1$ ). The strength and pressure are normalised by strength and pressure components of HEL. The parametric variation of the constants in a systematic fashion is achieved by making the strength and damage analytical functions of pressure and other state variables. The strength is smoothly varied as a function of intact strength, fracture strength, strain rate and damage.

$$\sigma^* = \sigma_i^* - D (\sigma_i^* - \sigma_f^*) \quad (1-7)$$

where  $\sigma_i^*$  denotes the normalised intact equivalent stress,  $\sigma_f^*$  denotes the normalised fracture stress and  $D$  is the damage varying from 0 to 1. The normalised equivalent stress ( $\sigma^*, \sigma_i^*, \sigma_f^*$ ) have a general form of

$$\sigma^* = \frac{\sigma}{\sigma_{HEL}}$$

The normalised intact strength is given by

$$\sigma_i^* = A(P^* + T^*)^N (1 + C \ln \epsilon^*) \quad (1-8)$$

and the normalised fracture strength is given by

$$\sigma_f^* = B(P^*)^M (1 + C \ln \epsilon^*)$$

$M, N, A, B$  and  $C$  are material constants. The damage ( $D$ ) is expressed as

$$D = \Sigma \frac{\Delta \epsilon^P}{\epsilon_f^P} \quad (1-9)$$

where  $\epsilon^P$  is the plastic strain during a cycle of integration and  $\epsilon_f^P$  is the plastic strain for fracture under a constant pressure  $P$ .

$$\epsilon_f^P = D_1 (P^* + T^*)^{D_2} \quad (1-10)$$

where  $D_1$  and  $D_2$  are again constants. The normalised pressure ( $P^*$ ) and cutoff tension ( $T^*$ ) are defined as,

$$P^* = \frac{P}{P_{HEL}}$$

$$T^* = \frac{T}{P_{HEL}}$$

Where  $P_{HEL}$  is the pressure at HEL.

### JohnsonHolmquistBeissel Model

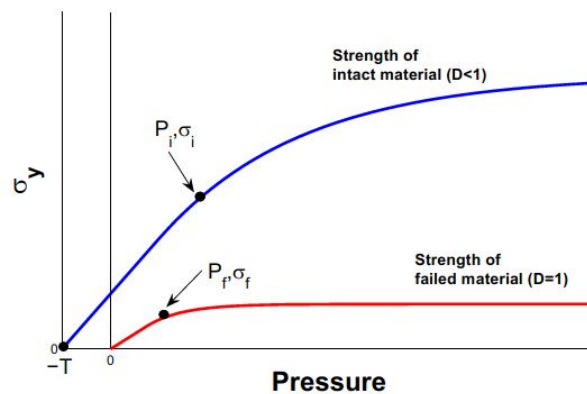


Figure 1-6: JHB model[4]

Johnson, Holmquist and Beissel developed the model by formulating material strength and damage as pressure dependent variables, similar to JH -2 model. However the sudden and abrupt decrease in material strength at complete damage ( $D = 1$ ) is comon with JH-1 [17]. The intact strength of the material is given by

$$\sigma_{intact} = \sigma_i + [\sigma_{max}^i - \sigma_i] [1.0 - \exp(-\alpha_i (p - p_i))] \quad (1-11)$$

where

$$\alpha_i = \frac{\sigma_i}{(\sigma_{max}^i - \sigma_i) (p_i + T)}.$$

Here  $\sigma$ ,  $\sigma_{max}^i$  and  $P_i$  are material parameters, where the subscript  $i$  indicates intact material. Pressure,  $p$ , is defined as  $p = \frac{1}{3} tr(\sigma)$ .  $T$  is the maximum tensile stress of the ceramic. Equation 1-11 holds for a pressure greater than  $p_i$ . For smaller pressures, the strength is a linear function from  $\sigma(p = -T) = 0$  to  $\sigma(p = p_i) = \sigma_i$ . In Figure 1-6 the intact material strength is shown with blue.

The strength of failed material is represented in a similar way as intact material. For pressures greater than  $p_f$ , failed material strength is defined by

$$\sigma_{failed} = \sigma_f + [\sigma_{max}^f - \sigma_f] [1.0 - \exp(-\alpha_f (p - p_f))] \quad (1-12)$$

where

$$\alpha_f = \frac{\sigma_i}{p (\sigma_{max}^i - \sigma_i)}.$$

where  $\sigma_f$ ,  $\sigma_{max}$  and  $p_f$  are material parameters where, the subscript  $f$  denotes the failed material. For pressures smaller than  $p_f$  the failed strength is a linear function from  $\sigma(p = 0) = 0$  to  $\sigma(p = p_f) = \sigma_f$ . In Figure 1-6 the failed material strength is shown with red.

## 1-4 Conclusion and Problem Statement

Ceramic being a brittle material experiences little ductility, and its strength is highly dependent on pressure. Ceramics are much stronger in compression than tension. Cone cracking among the various failure mechanism discussed above has been chosen to be studied through indentation via simulations. Material models by Johnson and Holmquist [16], Deshpande and Evans [3], as well as Walker and Anderson [8], are frequently used for simulating the ceramic failure. The results obtained from these material models match with one particular set of experimental results, but often fail to predict the results obtained from a different set of experiments. These models have features like plasticity, dilation, softening common with Drucker Prager model. Drucker-Prager (DP) Model is easy to use and implement through numerical methods. The constitutive relationships in DP formulation are simple.

An Analogy can be taken from the soil and rock mechanics as the characterization of ceramic under impact is not limited to the intact material but also the comminuted particles which behave more or less like rocks fragments showing dilatant behaviour. Drucker Prager (DP) model is most widely used for understanding the rock like behaviour and cone cracks are also seen in rocks during indentation [18], [19], [20]. In view of this commonality and its simplicity,

the DP model can be employed to analyze cone cracking and tensile failure in ceramic. Based on the discussions above, the standard Drucker Prager (DP) Model, which also captures the effect of comminution, is selected as a promising starting point for understanding the ceramic failure mechanism through simulated indentation by numerical methods in JEM JIVE FEM library

## 1-5 Research Objectives

Cone cracking is one of the prominent failure modes of ceramic. Therefore, it is important to understand the circumstances leading to such failure in order to design superior armour protection. Keeping this broad aim in view, the following are set as objectives of the present thesis works.

1. The prime objective is to understand the effects of material parameters such as cohesion, friction angle, dilatancy and softening of ceramics besides confinement on ceramic failure by ring and cone cracking through simulated indentation by the DP formulation.
2. The DP model does not consider pressure dependent softening which gets manifested by the brittle nature of ceramic. It also tends to overestimate the compressive strength of the material. Hence the second objective is to introduce necessary remedial mechanisms into the model to overcome these deficiencies.
3. Often it is difficult to obtain objective results out of simulations of material models due to mesh sensitivity. Viscoplastic integrated elements incorporated into the material model formulation have been found to be effective in solving mesh sensitivity issues in past research works. Accordingly, the third objective is to modify the DP model suitably to examine the possibility of controlling mesh sensitivity.

## 1-6 Outline of thesis

To achieve the objectives mentioned above, the current study is organized as shown in the flow chart given in Figure 1-7. In Chapter 2, the effects of material parameters viz - angle of friction, dilatancy, softening on cone crack formation and propagation is studied. The consequences of confinement and mesh sensitivity are also covered. Chapter 3 focuses on modifying the standard DP model to capture the pressure dependent softening. Chapter 4 explores the limiting the yield function in the standard DP model and its effect on the quasi plastic deformation in the ceramics. Chapter 5 examines viscoplasticity to mitigate the mesh sensitivity. The DP model is suitably modified by integrating viscoplasticity in this regards. Perzyna based viscoplasticity. In Chapter 6 the report concludes the findings of the studies carried out vis a vis research objectives besides listing recommendations for future work.

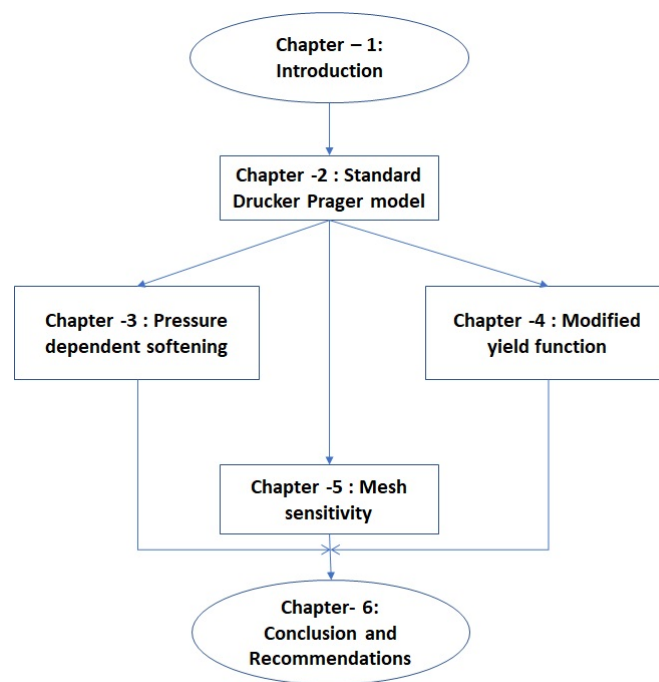


**Figure 1-7:** Outline of chapters

# Standard Drucker Prager implementation

The DP model was proposed by Drucker and Prager in 1952 [21]. It was developed to study the failure mechanism of pressure-sensitive materials such as rock, soil and concrete. The yield function ( $f$ ) is defined as

$$f = \sqrt{3J_2} - \eta p - \zeta \quad (2-1)$$

where  $p$  is the pressure and  $J_2$ , the constants  $\eta$  and  $\zeta$  are defined as

$$J_2 = \frac{1}{2} \sigma^T \mathbf{P} \sigma \quad (2-2)$$

$$\eta = \frac{6 \sin \phi}{3 - \sin \phi} \text{ and } \zeta = \frac{6 c \cos \phi}{3 - \sin \phi} \quad (2-3)$$

$c'$  is the cohesion of the material and  $\mathbf{P}$  is defined as

$$\mathbf{P} = \begin{bmatrix} \frac{2}{3} & -\frac{1}{3} & -\frac{1}{3} & 0 & 0 & 0 \\ -\frac{1}{3} & \frac{2}{3} & -\frac{1}{3} & 0 & 0 & 0 \\ -\frac{1}{3} & -\frac{1}{3} & \frac{2}{3} & 0 & 0 & 0 \\ 0 & 0 & 0 & -2 & 0 & 0 \\ 0 & 0 & 0 & 0 & -2 & 0 \\ 0 & 0 & 0 & 0 & 0 & -2 \end{bmatrix}, \quad (2-4)$$

where  $\phi$  is the angle of friction, and the shear strength  $c$  of the material is defined as

$$c = c' \left( 1 + h \epsilon_p^{eq} \right) \quad (2-5)$$

where  $h$  is the material softening and  $\epsilon_p^{eq}$  is the equivalent plastic strain. The plastic potential function ( $g$ ) is defined as

$$g = \sqrt{3J_2} - \bar{\eta} p \quad (2-6)$$

where  $\eta$  is defined as,

$$\bar{\eta} = \frac{6 \sin\psi}{3 - \sin\psi}$$

with  $\psi$  as the angle of dilatancy and it determines the flow direction from trial state to the yield surface as shown in Figure 2-1. The direction of flow is at an angle equal to dilatancy ( $\psi$ ) from the vertical as per the postulates of DP Model. Associated flow condition is attained provided angle of friction equals dilatancy angle. If the angle of dilatancy in the non-associative flow is zero, the flow reduces to the Prandtl - Reuss regime that predicts volume preserving flow. The plastic strain rate  $\dot{\epsilon}$  is defined by

$$\dot{\epsilon}_p = \dot{\lambda} \left( \frac{\partial g}{\partial \sigma} \right) \quad (2-7)$$

$\lambda$  is the plastic multiplier.

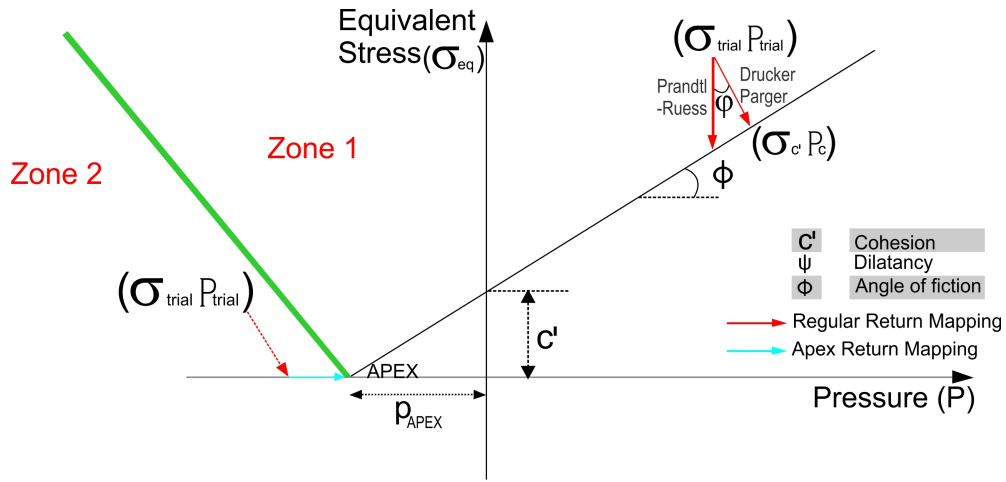


**Figure 2-1:** Drucker Prager Model - stress vs pressure

A straight line is obtained by plotting the yield surface on the  $p$  vs  $\sigma_{eq}$  plane, as shown in Figure 2-1. The point  $(p_{apex}, 0)$  represents the vertex of the Drucker Prager cone, the minimum allowed pressure state. The cohesion is the shear strength at pressure ( $p=0$ ). The angle of friction ( $\phi$ ) is the slope of the yield surface. A singularity exists in the DP yield surface at the apex. The stress integration is done by Backward Euler algorithm. Two separate mapping schemes have been used to arrive at the yield surface from trial stress - smooth mapping scheme for the Zone 1 [6] and apex return for zone 2 [7] in the stress - pressure space. The stress algorithm and consistent tangent matrix have been discussed in detail in section 3-3.

## 2-1 Verification

The verification of the Drucker Prager material model is done through unit cube test. It involves simulated uni-directional compression and tension via prescribed displacements. The sample is confined in all directions, except one as shown in Figure 2-2a. Displacement of  $50 \mu\text{m}$  is prescribed in 100 load steps with an increment of  $0.5 \mu\text{m}$ , followed by unloading, in

equal numbers of load steps. All simulations are based on values of  $E = 220$  GPa and  $\nu = 0.3$ . Plane strain condition has been assumed. Pressure vs equivalent stress plot for the simulations is obtained to understand the effects of dilatancy, cohesion, angle of friction and softening under tension and compression. The consistent tangent matrix is checked by splitting the cube into an unsymmetrical mesh as shown in Figure 2-2b. The results so obtained are vetted against the ones obtained from original unit cube test. The correct implementation of Euler Backward return and the apex return formulations are checked through a series of simulations by varying the parameters. The effects of variations in softening and dilatancy on the results of unit tests to tension are found to be significant and discussed in further detail.

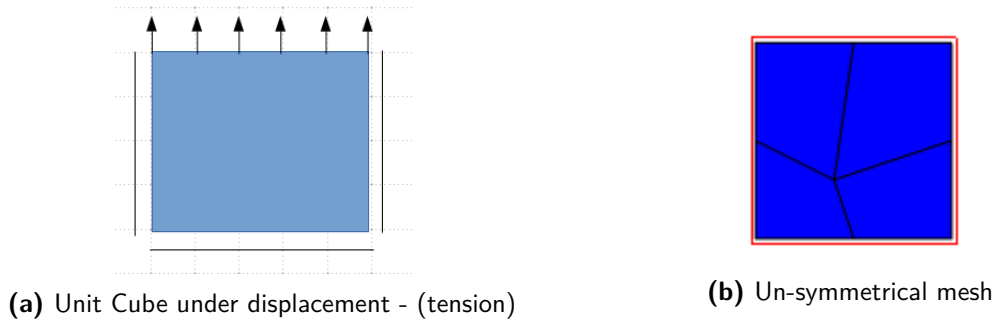


**Figure 2-2:** Unit test

### 2-1-1 Softening

The results of unit cube test under tension corresponding to a range of softening values are presented in 2-3. The friction angle and dilatancy are both fixed at  $10^\circ$  during the test. The negative sign assigned to the softening values is to highlight the fact that the material strength decreases. Therefore, an increase in softening/softening modulus is depicted by the mod of softening values rather than the negative values themselves in conventional terms. Since the softening modulus is a measure of the degree of softening, the two are considered to be synonyms in this study.

The plots between pressure and equivalent stress for different values of softening modulus are presented in Figure 2-3. The generic path followed by all the plots is OABOC. Point B, O and C represent sets of points containing apex, the start of unloading and unloaded state respectively. The plots between pressure and equivalent stress for different values of softening are the same within the elastic limit represented by point A in Figure 2-3. On further loading, plastic flow starts and the material begins to lose its strength, as shown in the plots corresponding to different softening values by the decrease in equivalent stresses. Reduction in the strength of the material is observed with increase in softening from zero in subsequent iterations.

The apex return algorithm is applied to find the apex - cutoff pressure during loading, as depicted by point B in the plot. The pressure - stress state travels along the pressure axis on further loading until unloading starts. The material loses its complete strength during the loading cycle for the value of  $h = -8$  or more and the unloading starts from the origin.

The consistent tangent matrix is a null matrix on arriving at the origin. This indicates that as the stress state arrives at the origin O in the plot, it remains there until unloading or neutral loading occurs. The apex return mapping is not able to bring the stress-pressure state to the apex on further increase in softening and directly takes the stress to its final position which is the origin. The plots for unloading are in plastic domain. The differences in slopes of plots (Figure 2-3) corresponding to different softening values are very small and hence they are not parallel although they seem to be so. Unit test results indicate that the residual strength decreases with increasing softening. Furthermore, for softening  $h=-8$  MPa or more, the material completely softens i.e it has no residual strength. Tests carried out at smaller magnitudes of softening ( $h=-1$  and  $-2$  MPa), results into a gradual strength decrease. Similar behavior is also noticed in ductile material. Brittleness is exhibited by samples at larger magnitude of softening.

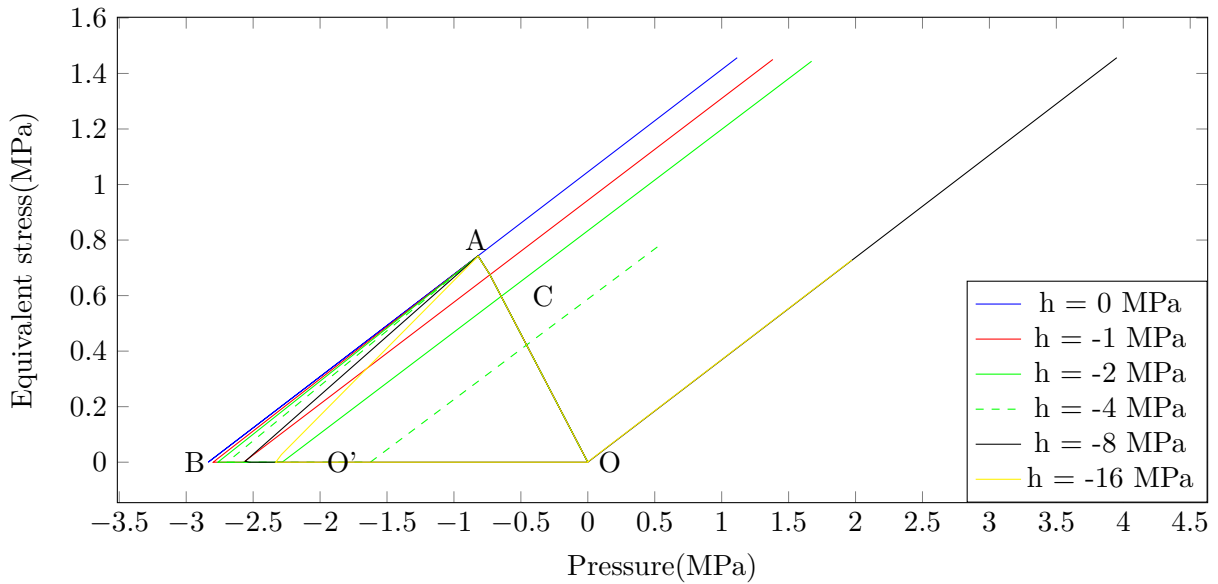


**Figure 2-3:** Unit load test for varying Softening

### 2-1-2 Diltancy

The angle of dilatancy modifies the direction of return from the trial state to the yield surface via plastic potential function. As the the model is simulated while introducing dilatancy, the plastic flow no longer remains volume preserving and the hydrostatic component of stress continues to increase the pressure further with increase in angle of dilatancy for a given trial strain. The  $p$  vs  $\sigma_{eq}$  plots corresponding to varying diltancy from  $5^\circ$  to  $30^\circ$  at constant softening of  $-10$  MPa and friction angle of  $30^\circ$  are presented in Figure 2-4. Every simulation follows the same path till the elastic limit denoted by line OA. However, the peak values are not the same. This indicates that the selected load step during unit test is large. Selection of smaller load step during simulation could lead to convergence of peak to a single value which is ideally expected. Stress is observed to decrease with increase in pressure during plastic flow represented by AB. Increase in resistance of the material, is also observed with increase in

dilatancy at constant softening. This is attributed to the fact that the pressure increases much faster with increase in dilatancy as explained earlier. It is concluded that larger dilatancy increases the residual strength at the end of the loading-unloading cycle, thus perform better in resisting the load.

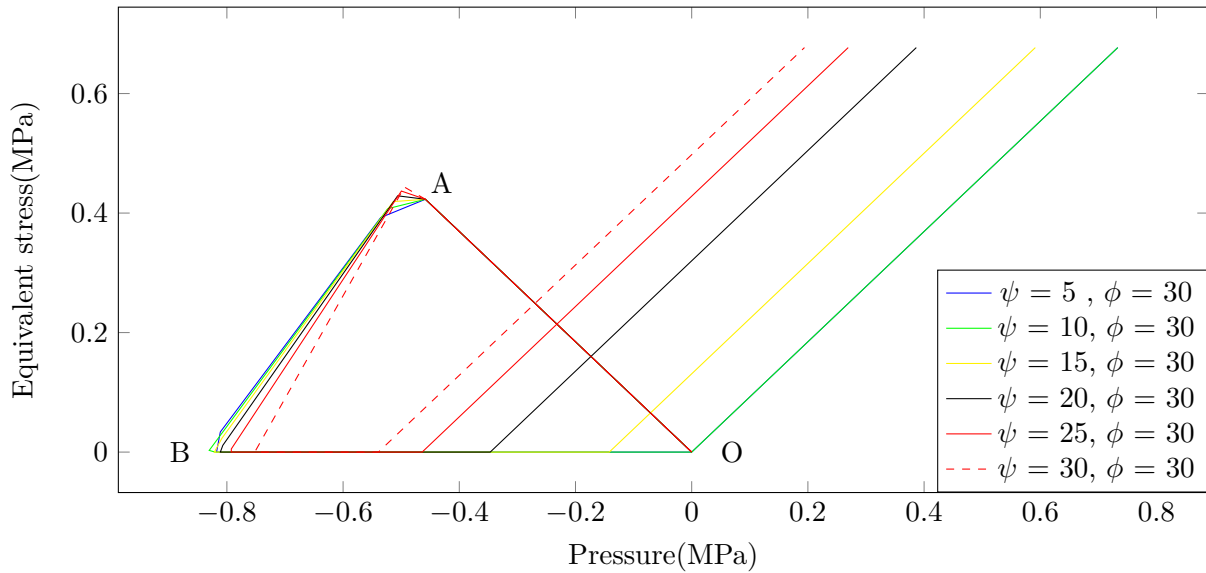


Figure 2-4: Unit load test for varying angle of dilatancy

## 2-2 Validation

The validation of the Drucker Prager model is done with results available in the literature. Strip footing test is one of the common validation for the Drucker Prager model. The strip footing as shown in Figure 2-5 from the publication from Hijaj, Fortin and Saxce [22] is used as the benchmark to validate the material model.

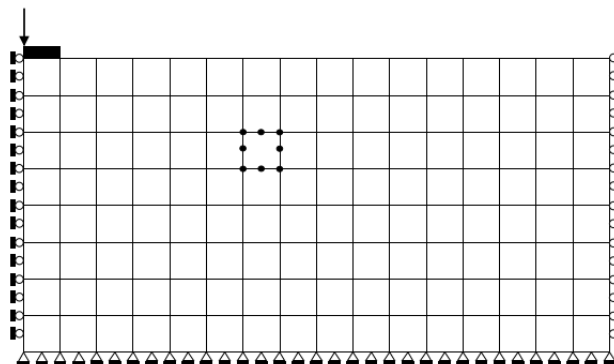
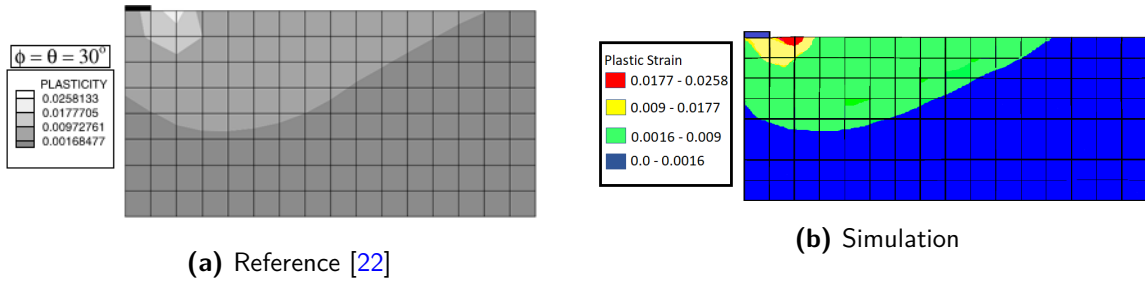


Figure 2-5: FEM mesh for Strip footing

The strip footing is simulated. A soil mass of size 50 m x 100 m is modelled. The Young's

modulus is 2.5 GPa, the Poissons ratio is  $1/3$  and the cohesion is 2.0 MPa. Displacement control till 0.05m is prescribed as loading on the left node of the rigid elastic plate shown in Figure 2-5. The discretisation of the soil mass in the simulation is done via 4 noded quad elements. The simulation in the referred literature uses 8 noded elements. The mesh contains 128 elements. Quadrilateral elements with  $2 \times 2$  integration scheme have been used. The domain of the footing is taken large enough to avoid any interaction with boundary. Plane strain formulation is implemented. The boundary has been constrained on the left, right and bottom edges. The input data for the simulation has been referred from the publication by B Hijaj, Fortin and Saxce [22].



**Figure 2-6:** Equivalent plastic strain for angle of friction ( $\phi = 30$ )

Equivalent plastic strain contours developed from the footing load in soil mass in simulation and literature are shown in Figure 2-6b. Equivalent plastic strain contours have concentric zones with reducing strain. The use of 8 noded elements in the literature could be a possible reason for the variation in the contours. The maximum plastic strain develops at the top edge of soil adjacent to the loaded area. The force-displacement diagrams are shown in Figure 2-7 for the simulation and the reference article are plotted together. The plots corresponding to simulation and literature are in the firm and dotted lines respectively for various dilatancy angles. Force attains similar peak values for both the plots from the simulation and literature, but the simulation curves are much more gradual as adaptive load step is used, while there are only 8 load steps to achieve 0.05mm displacement in the reference. Associative flow conditions, which results in maximum force to any given displacement, develops when the angle of dilatancy becomes equal to the angle of friction. A similar situation occurs when the input value of  $\psi$  is raised to  $30^\circ$  and this causes the force to grow to a maximum as seen in Figure 2-7.

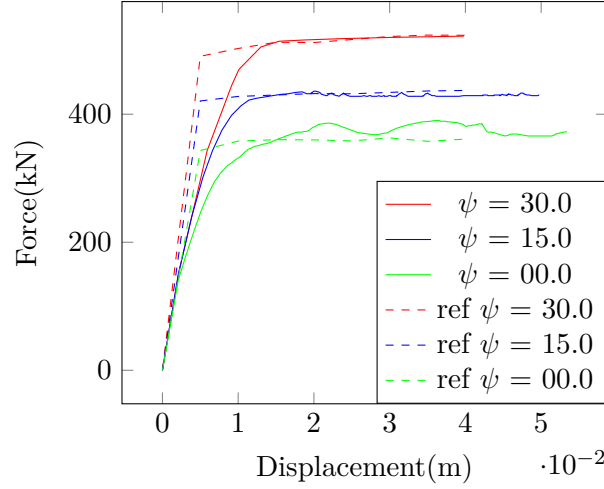


Figure 2-7: Load Displacement plot

## 2-3 Indentation

### 2-3-1 Material Properties

The indentation simulation comprises of an indenter and a target as shown in Figure 2-8. The material chosen for the indenter is diamond, while alumina is chosen as the target. The mechanical properties are listed in Table 2-1.

Table 2-1: Mechanical Properties

	Indenter	Ceramic Target
Size (mm)	4mm dia	100mm x 100mm
Material	Diamond	Alumina
Density (gm / $cm_3$ )	7.80	3.51
Youngs Modulus (GPa)	1120	370
Poissons ratio	0.07	0.2
Tensile Strength (MPa)	-	200
Angle of friction ( $\phi$ )	-	70
Angle of dilatancy ( $\psi$ )	-	15
softening ( $h$ )	-	-30

Past studies and publications have been referred to understand realistic values of parameters for Alumina. Maijangos and Kelly use parameter values evaluated from triaxial test[23]. The cohesion evaluated varies from 11-15 MPa, and the angle of friction lies in the range of 43° to 49°. Gamble and Compton consider the angle of friction ( $\phi$ ) as 60°, and the angle of dilatancy ( $\psi$ ) as one fourth the value of  $\phi$  being 15° for 98% Alumina [24]. Deshpande and Evans (DE) considers even large value of angle of friction ( $\phi = 70^\circ$ ) for 99% Alumina [3]. Keeping these broad facts in view, the high value of the angle of friction ( $\phi = 70^\circ$ ) and dilatancy ( $\psi = 15^\circ$ ) at about quarter of friction angle, are considered for simulation purposes in the present

studies. The max tensile pressure of 0.2 GPa is referred from the Johnson and Holmquist paper [25].

### 2-3-2 Mesh and Simulation Parameters

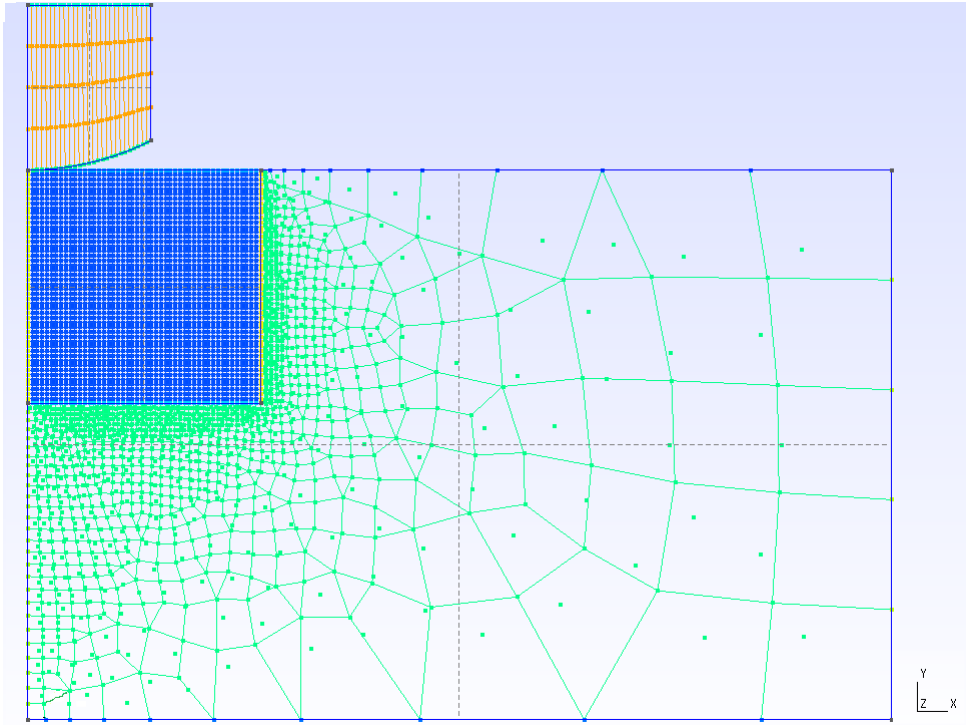


**Figure 2-8:** Generic mesh for studying Indentation

An assembly of spherical diamond indenter and ceramic tile is shown in Figure 2-8. In order to reduce the computational effort, segments of ceramic tile and spherical indenter at and around the contact are considered for modelling. The mesh is generated using GMSH. The ceramic target is split into two segments shown in blue (1.7 cm x 1.7 cm) and green mesh. Structured quadrilateral mesh in blue, with 60 divisions is adopted, in the zone of contact with the indenter, to study crack propagation accurately. The rest of the ceramic target has a non-structured quadrilateral mesh in green, with the mesh size increasing in the directions away from the contact zone. A total of 2163 element and 2256 nodes are used. The left and the bottom boundary of the target mesh has been fixed while the right edge is free. The nodes on the left edge of the indenter are also constrained. Indentation is performed till indentation depth of 40  $\mu\text{m}$  is reached in indentation experiments [26]. Axis - symmetric formulation is used for the simulation. The value of Coulomb friction is taken as 0.5. Penalty stiffness contact model is used. Penalty Stiffness of the order of  $10^4$  in the normal direction prohibits penetration without creating convergence complications. Penalty stiffness of 100 is assigned in the tangential direction. The penalty stiffness is much larger in the normal direction as it is the direction of prescribed displacement. Adaptive load step and contact model used for the indentation are explained in detail.

### Adaptive step size

The adaptive step size code developed by Erik Simons is used to decrease computation time and obtaining convergence with ease. It helps in getting convergence at critical points of crack closing and opening. The algorithm checks for the number of iterations required for obtaining convergence in the current load step. The algorithm has an inbuilt mechanism for increasing or decreasing the change in prescribed displacement by the adaptive load multiplier depending upon the no. of iteration is smaller or greater than its limiting value. In cases, where the no. of iteration is exactly equal to the limiting value, the load step from the previous iteration is carried for the next load step.

### Contact Model

Penalty stiffness method is used to treat contact between the ceramic target and indenter. Penalty stiffness algorithm adds a very large number to the stiffness matrix and restoring force vector to impose a prescribed displacement. The algorithm develops node to surface contact as shown in Figure 2-9.

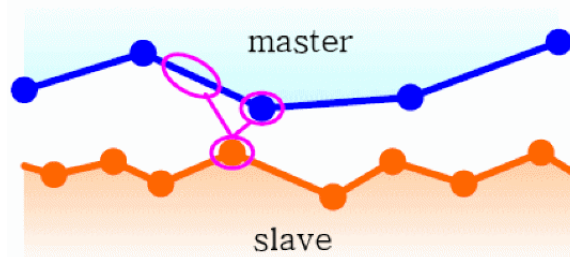


Figure 2-9: Node to surface contact.[5].

The contact model finds nodes with minimum distance from the surface to search for a possible contact ( 1% of element length). Contact force by increasing the stiffness is applied as shown in Figure 2-10 for violated segment / nodes.

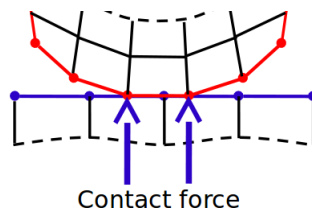


Figure 2-10: Contact - Force application[5].

The usual norm is to set the rigid surface as master and the curved surface as the slave as shown in Figure 2-10, hence the ceramic target is set as slave and the indenter as master.

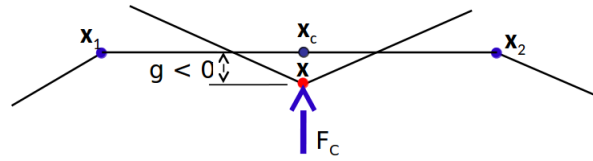


Figure 2-11: Contact - penetration[5].

Figure 2-11 shows the penetration of the indenter node in the target surface. Large contact stiffness reduces penetration but causes problems in convergence. The stiffness multiplier in the normal direction is set at a much larger value ( $10^4$  to  $10^8$ ) in comparison to the tangential direction (100). The residual penetration is shown as  $g$ . Initial gap between the indenter and the target is avoided as it has the potential to render the stiffness matrix singular.

### 2-3-3 Result

During indentation, plastic damage occurs below the indenter. A drop shaped zone of plastic strain under the combined action of compressive and shear stresses is developed under the indenter. Outside this zone, there is tensile stress. The maximum tensile stress develops at the free edge near the point of contact, and it falls gradually with increasing radial distance. The decrease in tensile stress is rapid with a decrease in depth below the ceramic surface.

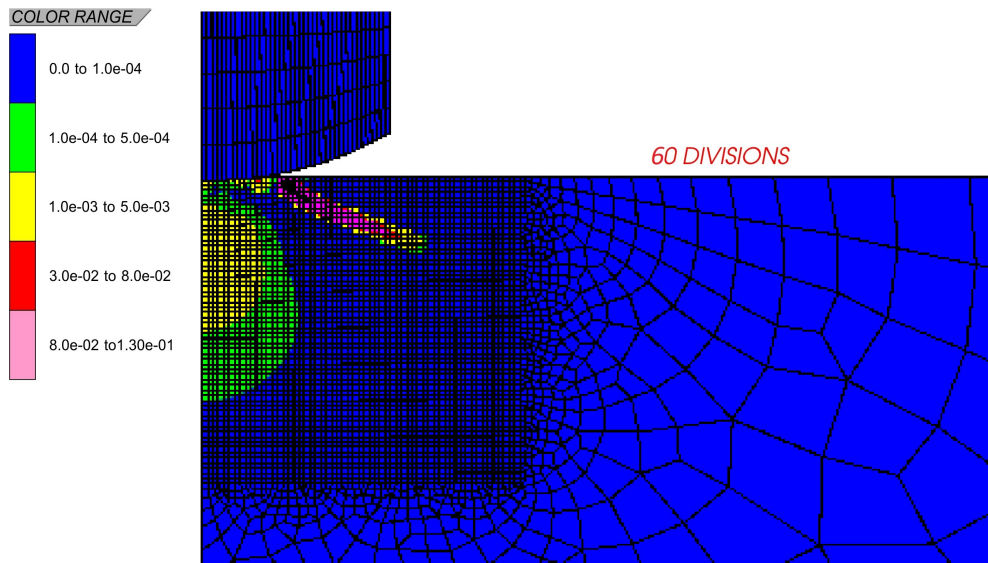


Figure 2-12: Plastic strain for indentation in Alumina

The radial stress creates the cone cracks in the brittle material. Poisson's effect produces a compression strain field within the entire ceramic mass, thus neutralizing a part of tensile strain outside the drop-shaped compressive strain zone and diminishing the chances of the tensile crack formation to some extent. In the Figure 2-12, well developed cone crack can be seen for  $\phi = 70^\circ$  and  $\psi = 15^\circ$ .

### Crack Propagation

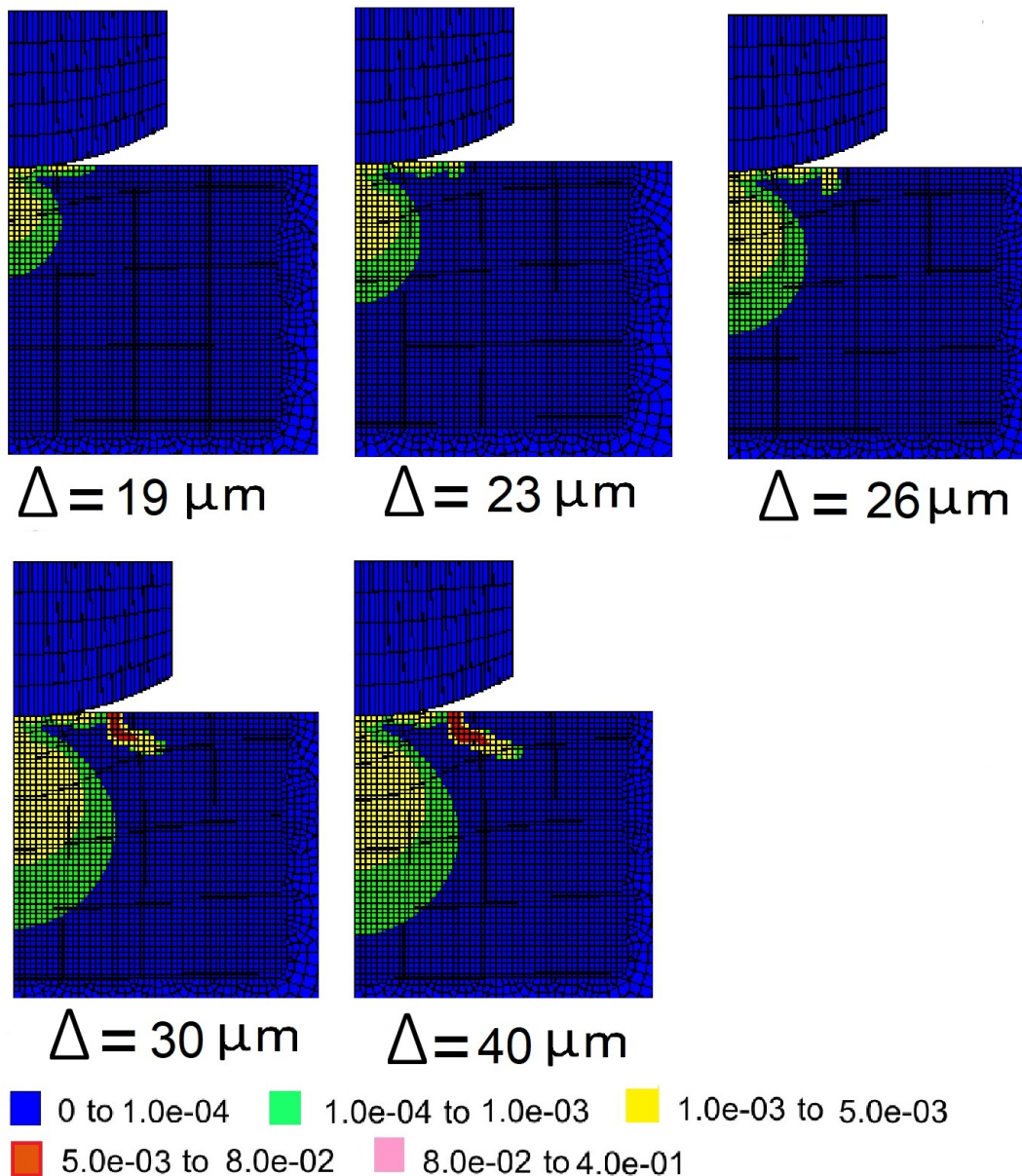
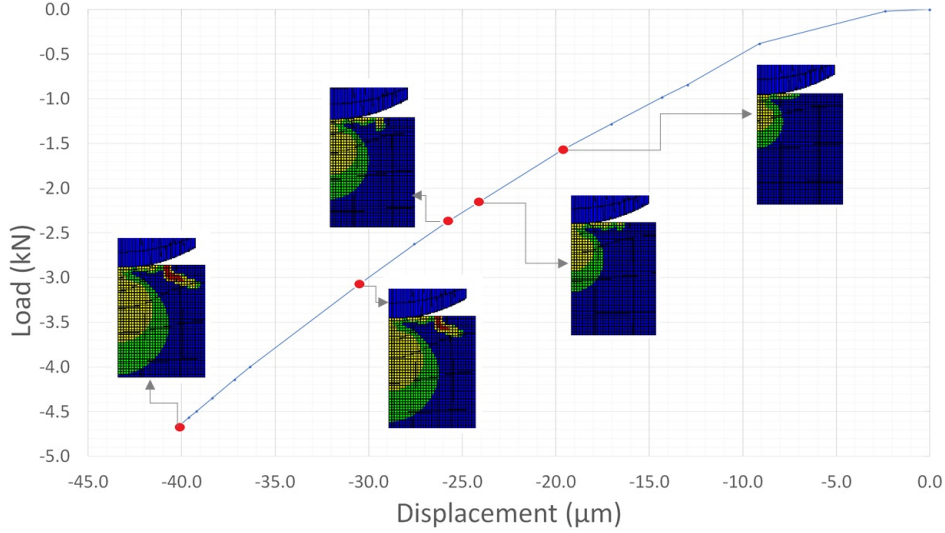


Figure 2-13: Indentation depth - Crack Propagation

The material parameters viz. angle of friction -  $70^\circ$ , the angle of dilatancy -  $15^\circ$ , softening -30, have been used with a mesh size of 60 elements in the zone of fine mesh for the simulation. The ring crack starts to form at an indentation depth of  $26 \mu\text{m}$ . It transforms into a cone crack while growing in size at an indentation depth of  $30 \mu\text{m}$  and becomes pronounced and

distinct from its earlier version of ring type. The cone crack size continues to increase for larger indentation depths. The zone of larger strain represented in pink colour is surrounded by zones of smaller strains in red, yellow and green colours. The entire sequence of crack propagation vis a vis indentation depth is shown in Figure 2-13.



**Figure 2-14:** Converged State: Load Displacement Curve

The cone crack half apex angle is about 63 degrees from vertical. Another phenomenon which occurs simultaneously with the ring/cone crack formation is the gradual but continuous increase in the zone of plastic strain below the indenter.

The Force-displacement diagram of the indentation process is presented in Figure 2-14. The slope of the curve is gradually increasing with increasing indentation depth implying that the rate of increase in force with respect to indentation depth is increasing, which is understandable. The red dots in the diagram denote indentation depths considered in the unit test. The plastic strain contours corresponding to the respective indentation depths are also shown in the diagram. It can be seen that cracks development is non linear and starts at a depth of 30  $\mu\text{m}$ . This is in accordance with the brittle nature of ceramic.

#### 2-3-4 Parameter study

The effects of angle of friction, the angle of dilatancy, softening, mesh size and confinement are determined through parametric studies. The parameter, the effect of which is to be determined, is varied during simulation process while keeping the rest of parameters fixed. The indentation depth of 40  $\mu\text{m}$  is considered for parametric study unless otherwise mentioned.

##### 1. Angle of Friction

The equivalent plastic strain contours developed during indentation is presented in Figure 2-16. Iteration has been done for  $\phi = 45^\circ, 50^\circ, 60^\circ, 65^\circ, 70^\circ, 75^\circ$  and  $80^\circ$ . During

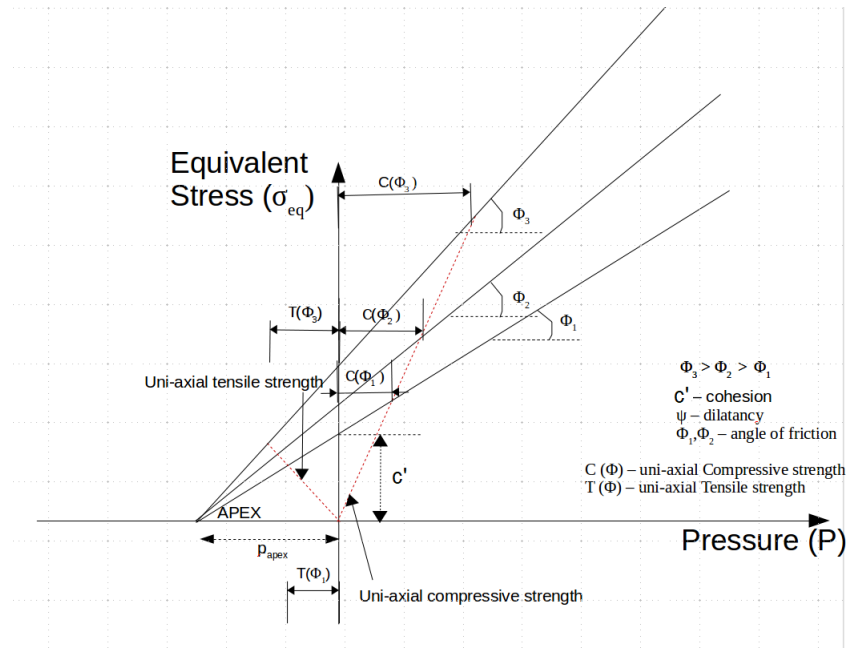


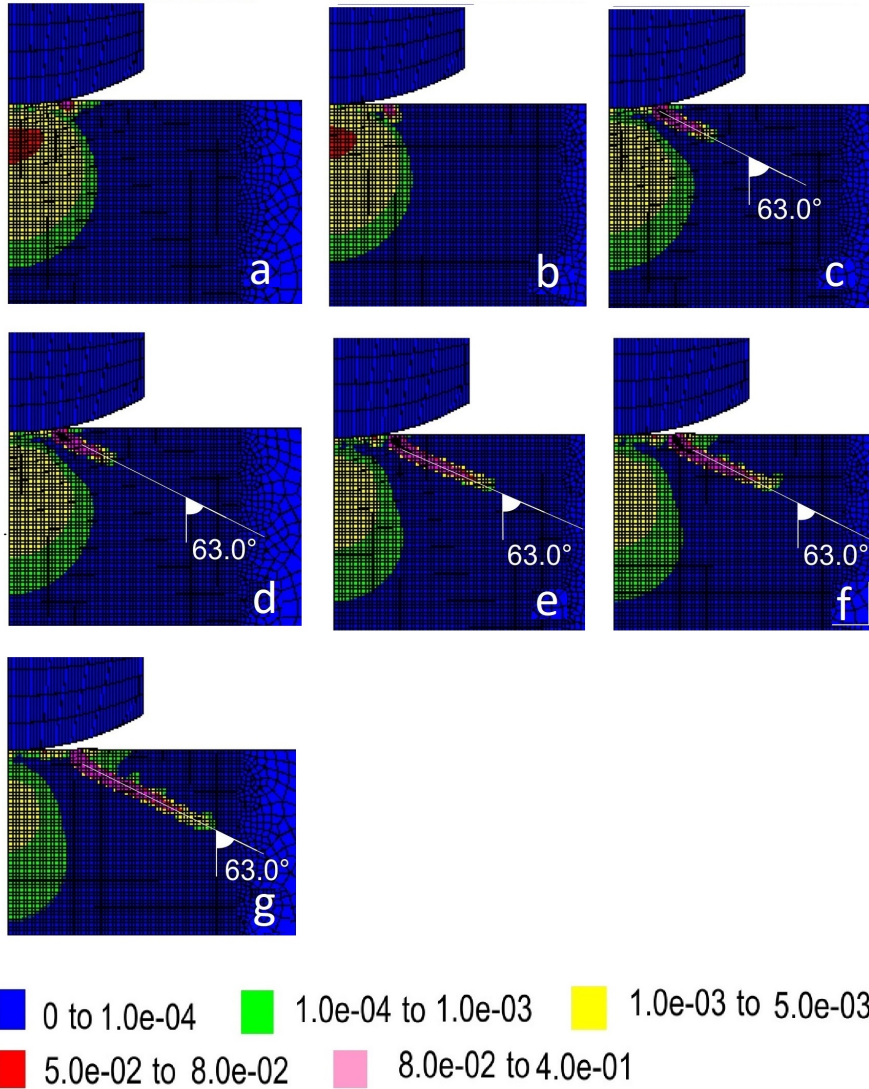
**Figure 2-15:** Uni- Axial Strength for varying angle of friction ( $\phi$ )

the simulation, the apex pressure is also updated with changing the angle of friction. For large values of  $\phi$  (nearing  $80^\circ$ ), the strength is much larger in compression than in tension for a given value of pressure as shown in Figure 2-15. The simulation studies with regards to the varying angle of friction ( $\phi$ ) throw some very interesting results. The bulbous zone of compressive plastic strain underneath the indenter (refer to Figure 2-16) is seen to decrease in size while the angle of friction of target material is increased. There is a significant reduction in bulb size corresponding to  $\phi = 80^\circ$  when compared to  $\phi = 50^\circ$ .

The first glimpse of ring crack representing plastic tensile strain is observed at  $\phi = 50^\circ$  degrees. The area under plastic tensile strain grows in size with the increase in angle of friction and consequently, the ring crack tends to develop into cone crack distinct from the neighbouring zone of bulbous compressive strain beneath the indenter. Distinctly elongated cone cracks are noticed at angles of friction equal to or more than  $60^\circ$  degrees. The cone crack gains in size with increase in angle of friction and the half apex angle is  $63^\circ$  degree. This is very close to  $68^\circ$  observed in quasi-static ball indentation in literature [27].

The location of initiation of cracks at indenter - target interface is observed to be gradually shifting away from the point of contact between indenter and target, as  $\phi$  increases. This results in an increase in the volume of the material resisting the load increases and thus better performance. The development of larger forces in the target for a particular value of prescribed displacement as seen in Figure 2-17 also validates the same. Cusps are formed in the load displacement diagram due to the representation of circular surface with elements in discrete finite element formulations. The most important outcome of the study is that angle of cohesion greater than  $60^\circ$  produce cone

crack and its increase produces larger cracks.



LABEL	Angle of friction	Crack No	No. of mesh	Mesh size	Distance	Angle
(a)	$\phi=49$	-	-	-	-	-
(b)	$\phi=50$	-	-	-	-	-
(c)	$\phi=60$	1	15	0.034	0.510	63
(d)	$\phi=65$	1	15	0.034	0.510	63
(e)	$\phi=70$	1	18	0.034	0.612	63
(f)	$\phi=75$	1	18	0.034	0.612	63
(g)	$\phi=80$	1	18	0.034	0.612	63

**Figure 2-16:** Equivalent Plastic Strain with variation in  $\phi$

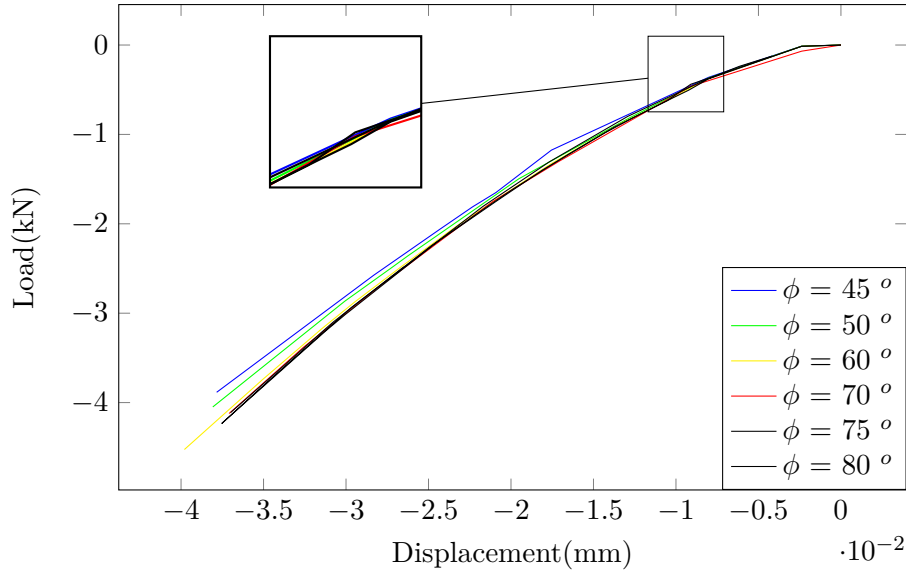
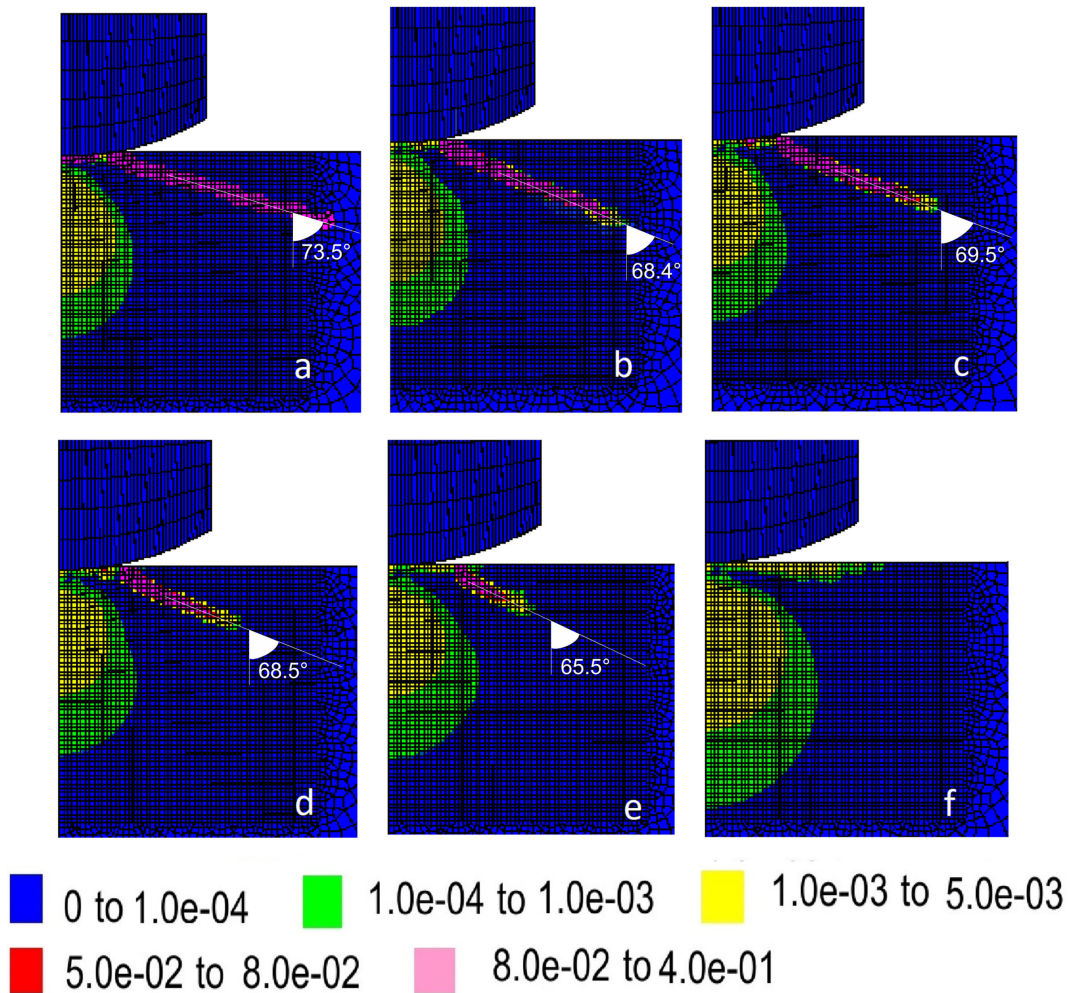


**Figure 2-17:** Force v/s Displacement plots for varying angle of friction

## 2. Dilatancy

The return path from the trial stress to the yield surface after Prandtl -Reuss plasticity [20] is modified in the DP Model via the plastic potential function (Figure 2-1). While the Prandtl -Reuss return path is vertical, the path as per DP Model is at an angle equal to  $\psi$  from the vertical. Therefore the DP model exhibits larger pressure increase while returning from trial stress to yield surface. Larger dilatancy results in a larger pressure increase. Therefore, the compressive bulbous zone of plastic strain grows with increasing dilatancy. Simulation results of indentation presented in Figure 2-18 prove this contention as correct. The growing zone of plastic compressive strain has a detrimental impact on the growth of tensile strain in its vicinity. Hence, the possibility of cone crack formation requiring large tensile strains diminishes with increasing dilatancy. The simulation results also show that the cone cracks size decrease gradually with increase in dilatancy. In fact, cone crack formation stops all together at  $\psi = 20^\circ$  corresponding to indentation depth of  $40 \mu\text{m}$  (Figure 2-18) and at  $\psi = 16^\circ$  corresponding to indentation depth of  $25 \mu\text{m}$  (Figure 2-20). These results indicate conclusively that dilatancy suppresses cone cracks. similar to the findings of LaSalvia and McCauley [11]. The  $\Delta$  in the Figure 2-20 shows the depth of penetration at which the strain contour has been plotted. The orientations of cone cracks corresponding to different dilatancy angles and indentation depths are nearly the same. Another interesting result of the simulation is the decrease in size of plastic tensile strain zone with decreasing indentation depth for the same dilatancy.



LABEL	DILATANCY ( $\psi$ )	Crack No	$\Delta$ ( $\mu\text{m}$ )	No. of mesh	Mesh size	Distance	Angle
(a)	0	1	32	14	0.034	0.476	
(b)	4	1	32	15	0.034	0.510	
(c)	8	1	40	16	0.034	0.544	
(d)	12	1	40	16	0.034	0.544	
(e)	16	1	40	16	0.034	0.544	
(f)	20	-	40	-	-	-	-

**Figure 2-18:** Equivalent Plastic Strain for variation in dilatancy ( $\psi$ )

Convergence becomes difficult as  $\psi$  approaches zero till an indentation depth of 40  $\mu\text{m}$

(Figure 2-18 a and b) is reached. Convergence is achieved till an indentation depth of  $32 \mu\text{m}$  for  $\psi = 0^\circ$  and  $4^\circ$ . But the cone cracks are comparatively longer than those corresponding to larger dilatancy (Figure 2-18 and 2-20). Well developed cone cracks for  $\psi \cong 0$  is explained by the fact that the return from the trial state never attains the apex for very small angles of dilatancy (Figure-2-1), resulting in very low material strength close to zero. Besides this, the bulbous zone of plastic strain is also comparatively smaller, thus exerting less influence on the growth of tensile strain in the surrounding volume. An aberration is observed as the compression failure zone is observed to remain almost the same in (Figure 2-18 : a, b and c) although the indentation depth increased from  $32 \mu\text{m}$  to  $40 \mu\text{m}$ . This can be due to the adaptive load step, which allows variation in indentation depth and the exact depth of  $40 \mu\text{m}$  might not be achieved during simulated indentation. No such aberration is noticed at indentation depth of  $25 \mu\text{m}$  as observed in Figure 2-20.

The force-displacement plot has been shown in Figure 2-19. The plots for all values are similar and smooth. The discrepancy shown in the box can be attributed to the variation in load steps imposed by the adaptive loading algorithm in the simulations and the numerical approximations in solving for equilibrium.

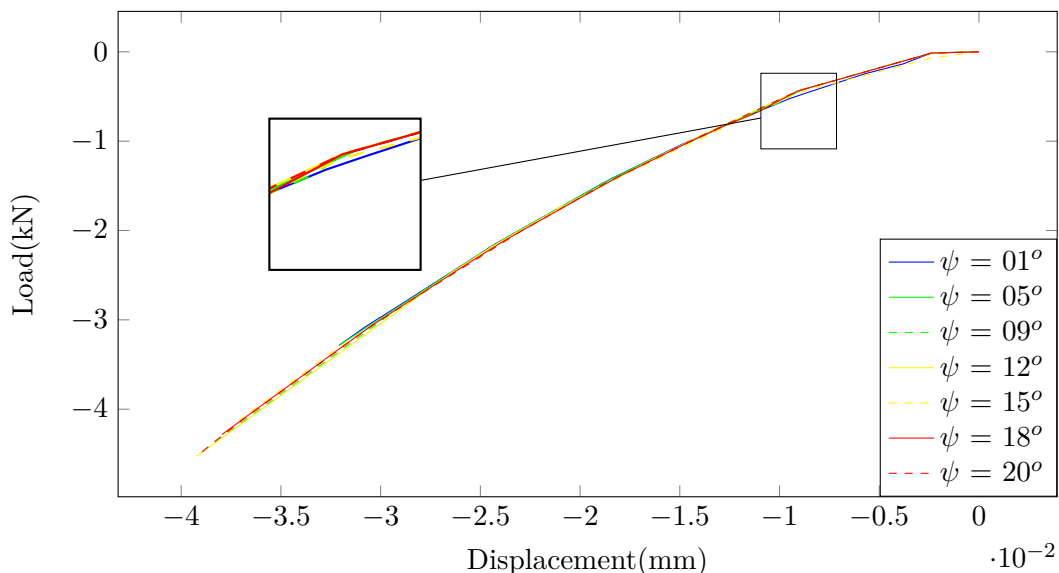
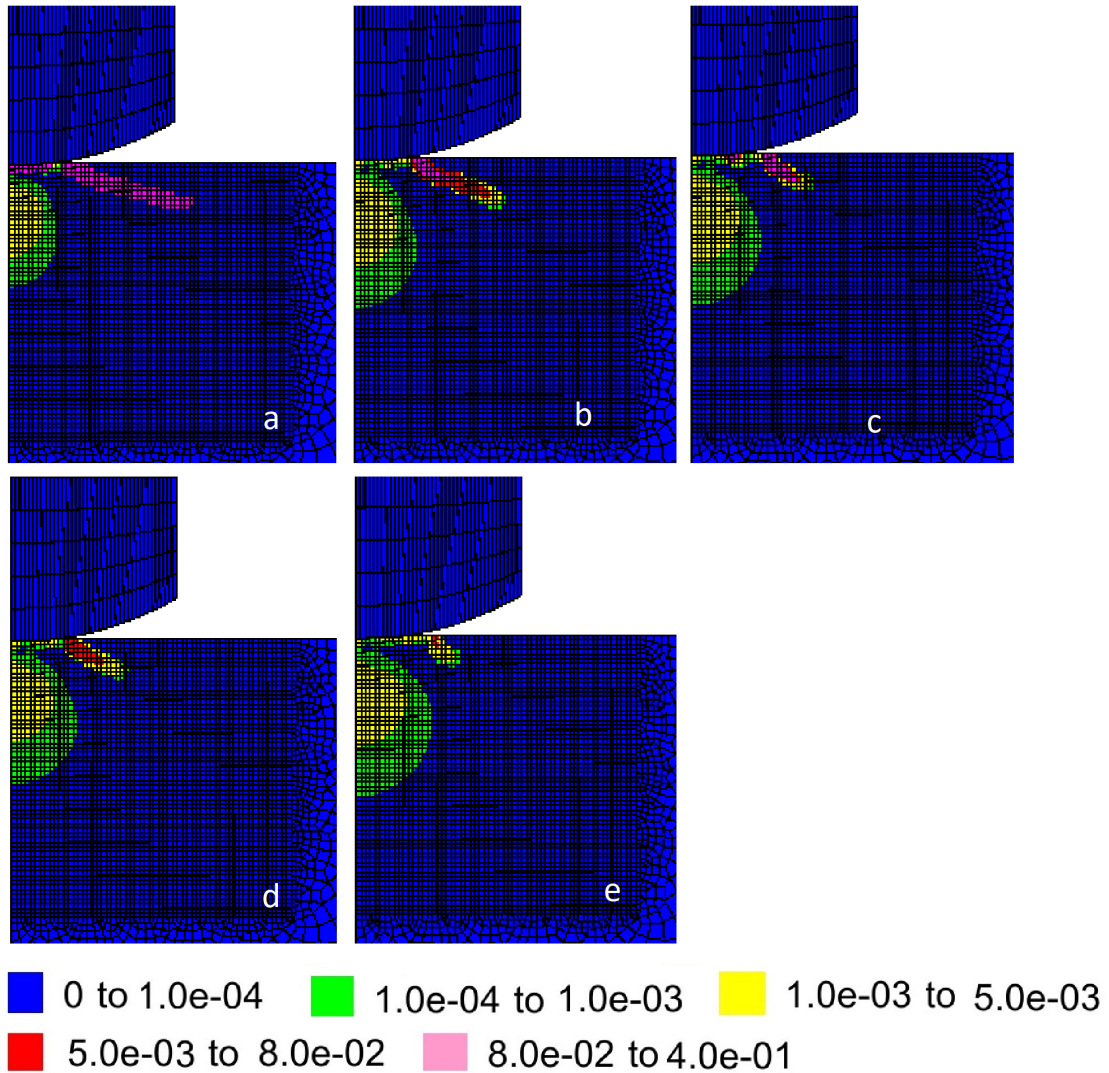


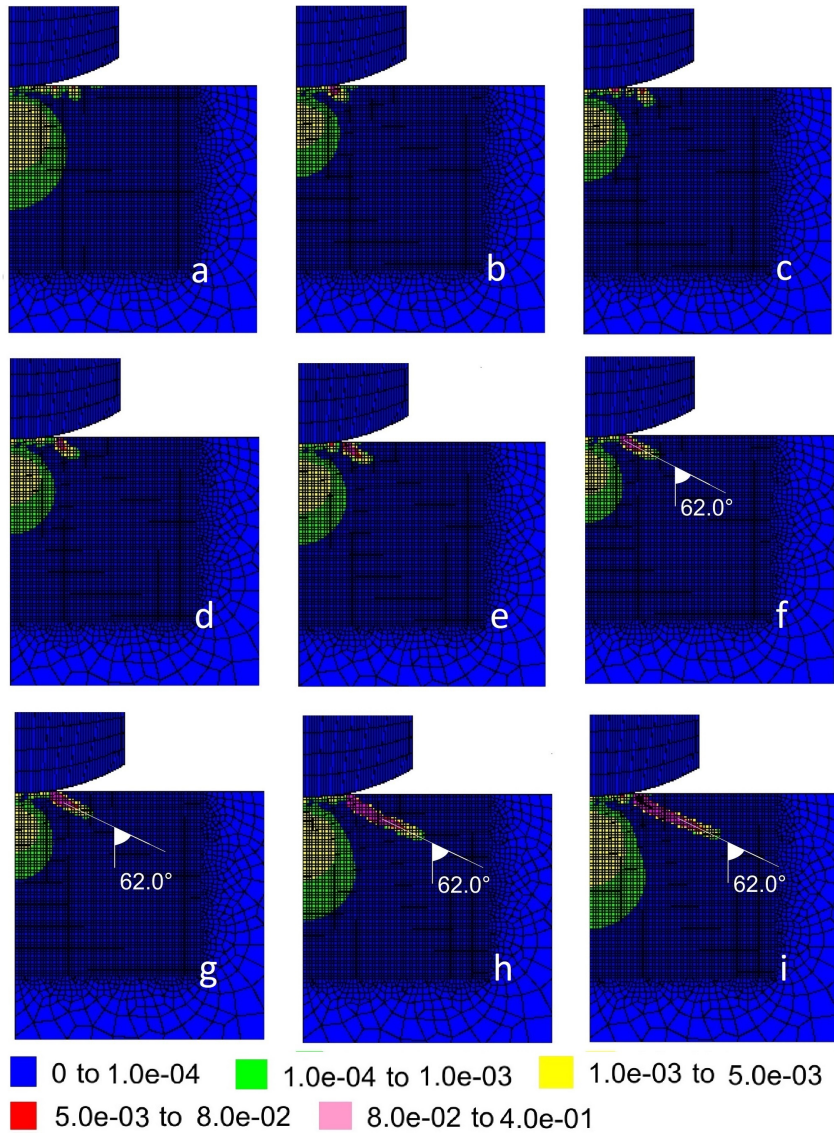
**Figure 2-19:** Force v/s Displacement plots for varying angle of dilatancy ( $\psi$ )



LABEL	DILATANCY ( $\psi$ )	Crack No	No. of mesh	Mesh size	Distance	Angle
(a)	0	1	14	0.034	0.476	
(b)	4	1	14	0.034	0.476	
(c)	8	1	16	0.034	0.544	
(d)	12	1	16	0.034	0.544	
(e)	16	-	-	-	-	-

**Figure 2-20:** Equivalent Plastic Strain for variation in  $\psi$  indentation depth of 25  $\mu\text{m}$

## 3. Softening



LABEL	SOFTENING h	Crack No	No. of mesh	Mesh size	Distance	Angle
(a)	-10	-	-	-	-	-
(b)	-20	-	-	-	-	-
(c)	-30	-	-	-	-	-
(d)	-40	1	18	0.034	0.612	-
(e)	-50	1	17	0.034	0.578	-
(f)	-60	1	16	0.034	0.544	62
(g)	-70	1	13	0.034	0.442	62
(h)	-80	1	13	0.034	0.442	62
(i)	-90	1	13	0.034	0.442	62

**Figure 2-21:** Equivalent Plastic Strain for variation in Softening at indentation depth of 25  $\mu\text{m}$

Softening controls, the rate of degradation of the material strength. The requirement of indentation depths for cone crack formation decreases as the softening increases. A linearly decreasing relationship is found between the indentation depth required for initiation of the major crack and the softening modulus. Convergence gets more difficult as softening increases for a constant indentation depth of  $40 \mu\text{m}$ . For values of softening larger than  $-50$ , local convergence is not achieved due to oscillating residual for the sub-increments of the stress integration at critical integration points. If the increment in load step is large, local divergence with anomalies in the  $L-\Delta$  graph is observed and the simulation terminates.

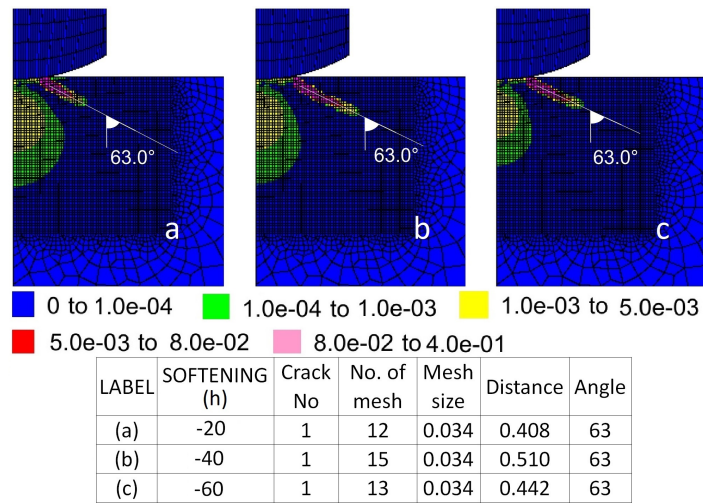


**Figure 2-22:** Maximum Equivalent Plastic Strain for variation in Softening at indentation depth of  $40 \mu\text{m}$

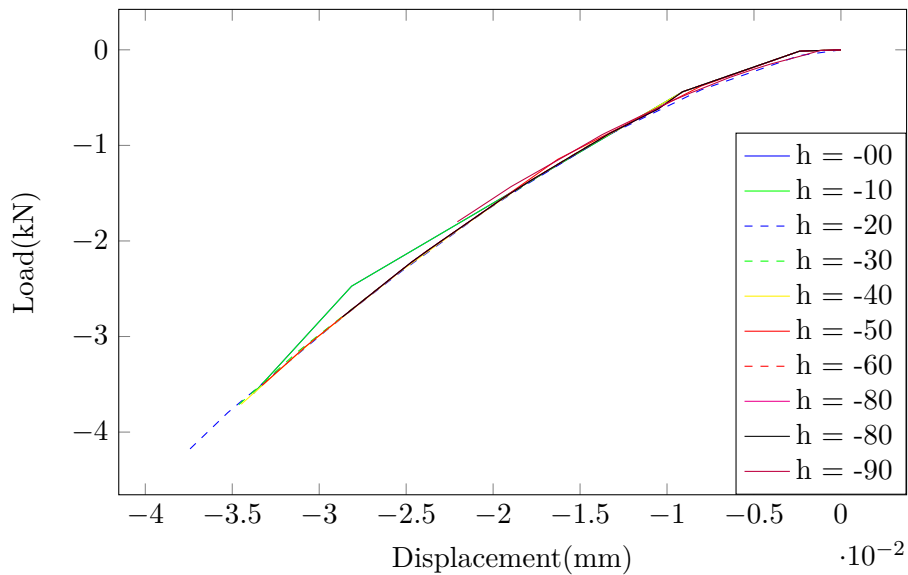
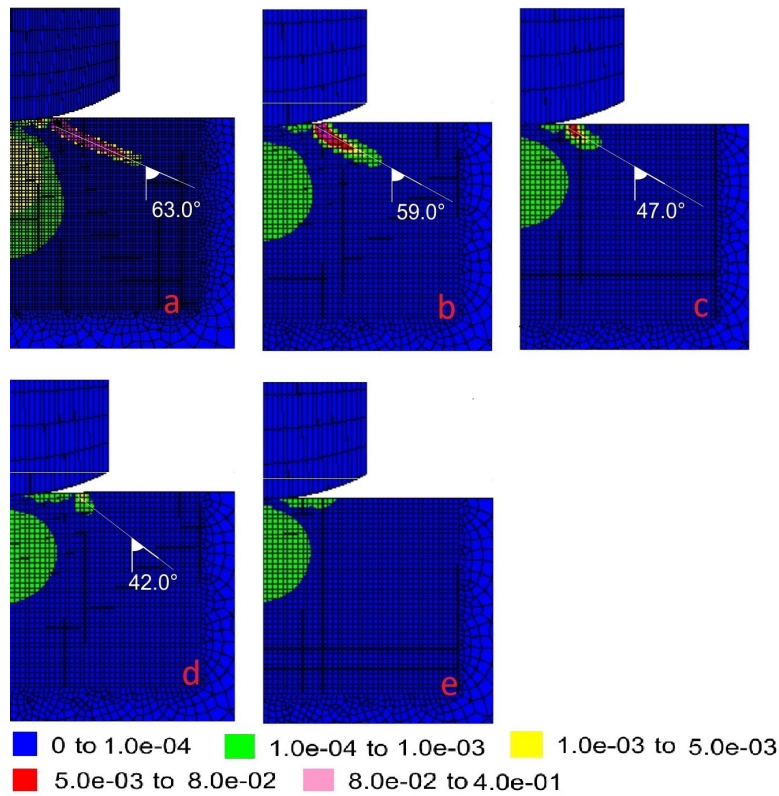


**Figure 2-23:** Force v/s Displacement plots for varying softening (h)

Figure 2-21, shows the contours of plastic strain for an indentation depth of 25  $\mu\text{m}$ . Well - developed cracks can be seen for  $h=50$  and larger values. Larger plastic strains are observed corresponding to higher values of softening. The quasi-plastic failure zone also increases as softening is increased. Figure 2-22 shows the plastic strains at an indentation depth of 40  $\mu\text{m}$ . The quasi-plastic zone in compression also increases with increase in indentation depth. From Figure 2-23, it is clear that the load-displacement response of all the simulations are similar.

4. Confinement

Confinement influences failure mechanism in ceramic. To study the effect of confinement on cone crack formation the ceramic target is restricted on the right edge as the most basic case. A compressive displacement of 0.5  $\mu\text{m}$  to 0.8  $\mu\text{m}$  in increments of 0.1  $\mu\text{m}$  is applied on the right edge to increase the degree of confinement. The increase in confinement eases convergence. Cone crack formation is hindered by confinement and is not observed altogether as the applied compressive displacement is increased to 0.8  $\mu\text{m}$ , as shown in Figure 2-24. The zones of compressive plastic strain corresponding to variable confinement do not show a change in size.



	CONFINEMENT $\mu\text{m}$	Crack No	No. of mesh	Mesh size	Distance	Angle
(a)	0.0	1	11	0.034	0.374	63
(b)	0.5	1	12	0.034	0.408	59
(c)	0.6	1	11	0.034	0.374	47
(d)	0.7	1	16	0.034	0.544	42
(e)	0.8	-	-	-	-	-

Figure 2-24: Equivalent Plastic Strain with variation in confinement

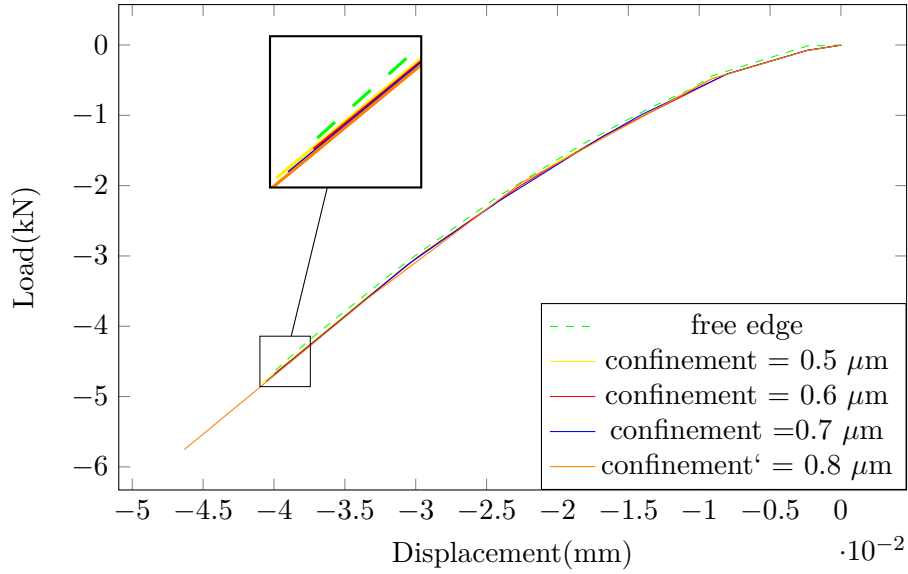


**Figure 2-25:** Force v/s Displacement plots for varying degree of confinement

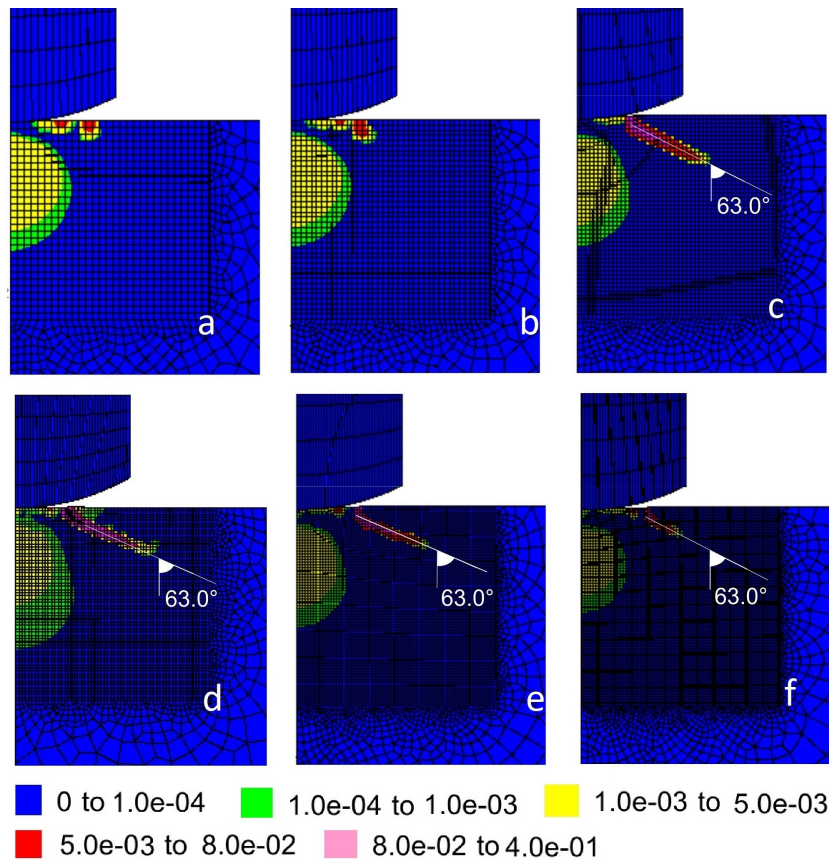
Force vs displacement plot is shown in Figure 2-25 projects an increase in force with an increase in the degree of confinement for any given depth of indentation.

#### 5. Mesh Sensitivity

Mesh sensitivity study is conducted by meshing the structured mesh of the block with 30, 40, 50, 60, 70 and 80 elements respectively. As the mesh size is decreased, achieving convergence becomes difficult. In order to achieve convergence during simulations, the contact stiffness multiplier needs to be increased to the orders of  $10^4$  for 40 element block and that of  $10^8$  for 70 element block, to avoid chances of large penetration in comparison to the size of elements. As the size of the element decreases, its becomes stiff and thus the penalty stiffness has to be increased. The position, orientation and growth of cone cracks depend on mesh size. As the mesh size is decreased the major cracks are formed further away from the origin, while the half apex angle of crack remains same as shown in Figure 2-26. Decreasing the mesh size has an insignificant effect on the load-displacement characteristics of the material as shown in the Figure 2-27.

**Table 2-2:** Computation time variation with mesh size

No. of Elements	No. of divisions	Computation time (s)	No. of Load Steps	Indentation depth
1367	30	49.5	14	0.0397
2163	40	108	17	0.0384
3200	50	725	32	0.04
4399	60	1061	111	0.036
5798	70	7873	160	0.037
7398	80	8688	299	0.033



LABEL	Mesh divisions	Crack No	No. of mesh	Mesh size	Distance	Angle
(a)	30	-	-	-	-	-
(b)	40	-	-	-	-	-
(c)	50	1	14	0.034	0.476	63
(d)	60	1	16	0.028	0.448	63
(e)	70	1	30	0.024	0.729	63
(f)	80	1	30	0.021	0.638	63

**Figure 2-26:** Equivalent Plastic Strain with variation in Mesh Size

There is also the issue of load sensitivity, as changing the mesh size warrants fine-tuning the adaptive load inputs to obtain convergence. Smaller mesh size requires smaller load increments for convergence, and therefore, computation time increases significantly to obtain an increase in indentation depth as seen in the summary given in table 2-2. The no. of load steps required for reaching the indentation depth of 40  $\mu\text{m}$  increases to nearly 300 for mesh with 70 and 80 elements. Mesh size with 50 divisions is found to be adequate for obtaining well-developed cracks. Reduction of mesh size does not necessarily result in easier cone crack development corresponding to an indentation depth of 40  $\mu\text{m}$ .

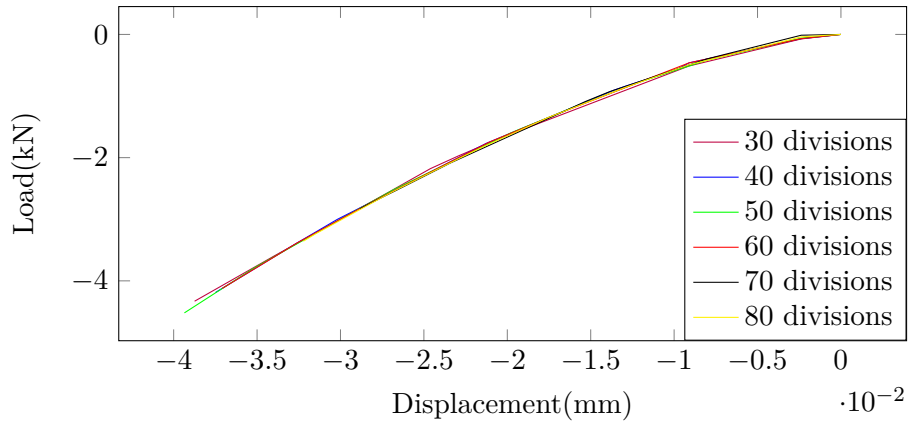


**Figure 2-27:** Force v/s Displacement plots for varying mesh size

## 2-4 Conclusion

A Mesh size with 60 divisions in the finely meshed zone has been found to be reasonable for simulation vis a vis computation time which increases by more than seven times with respect mesh size with 70 divisions. The variations in angles of friction and angle of dilatancy seem to affect the cone crack most. Large values of  $\phi \geq 60^\circ$  accompanied by low values of  $\psi < 15^\circ$  are observed to be favourable for crack development and propagation. As the indentation depth is increased, the distance of the point of crack initiation from the point of contact between indenter and ceramic target increases. But the cone crack undergoes little change in their shape or size at softening higher than that corresponding to the first appearance of cone crack. However, it influences the rate at which crack formation takes place. Confinement is observed to decrease the probability of crack formation. Mesh sensitivity is also encountered with the strain fields varying significantly with mesh size. It is concluded that alumina having low friction angle, high dilatant behavior and low softening modulus in confined conditions will be less prone to cone cracking.

# Pressure dependent softening

Softening is integrated with standard DP formulation vide equation 2-5, which states that the rate of decrease in material strength with respect to plastic strain is a constant i.e. softening is pressure independent. The parametric study discussed in chapter-2 is based on this postulate of Standard DP Model. Contrary to it, ceramic exhibiting brittleness undergoes non linear rapid degradation of strength post-elastic limit during indentation [28], [29], [30]. Evidently, softening of ceramic is pressure dependent rather than pressure independent. Hence appropriate modification to constitutive equations of standard DP model to account for pressure dependent softening is essential to evaluate the strength degradation and to understand plastic deformation of ceramic in a proper way. This objective is achieved in the following steps.

Step 1- Estimation of softening range applicable to the ceramic material: The range of softening applicable to ceramic is not directly available from the literature on experimental tests or standard material models developed in the past. However, Johnson and Holmquist (JH) model deals with the pressure dependent strength degradation. Therefore, JH model has been utilized to derive an approximate range of softening applicable to alumina.

Step 2- Simulation through modified Drucker Prager Model: The standard Drucker Prager (DP) model is calibrated and modified suitably to incorporate pressure dependent softening. The sets of pressure range and softening values obtained from step 1 above is fed to the modified DP model and simulation is carried out to determine the pressure dependent softening. The complete set of mathematical expressions describing the DP model on above lines and the results so obtained are presented in subsequent sections of this chapter.

### 3-1 Estimation of pressure - softening range

The range of softening applicable for ceramics is not directly available in the literature on experimental tests on ceramics, except models like Johnson Holmquist (JH2) model which

considers gradual pressure dependent strength degradation. The JH2 model is explained in detail in section 1-3-2. It is used to derive an approximate range of softening applicable for Alumina.

The yield function for the JH2 model

$$f = \sigma_{eq} - \sigma_c \quad (3-1)$$

where  $\sigma_{eq}$  is the equivalent stress. Strength of the material  $\sigma_c$  as defined in the JH2 model is

$$\sigma_c = \sigma_i - D(\sigma_i - \sigma_f) \quad (3-2)$$

where  $\sigma_i$  is the intact strength of the material and  $\sigma_f$  is the failed strength of the material. Both intact and failed strength are functions of pressure alone.  $D$  is damage variable and it is a measure of the level of fracture and has values ranging from 0 when the material is intact and 1 when the complete fracture has occurred.  $D$  is defined as

$$D = \Sigma \frac{\Delta \epsilon^p}{\epsilon_f^p} \quad (3-3)$$

where  $\Delta \epsilon^p$  and  $\epsilon_f^p$  stands for the change in plastic strain and the final plastic strain respectively. The softening modulus is defined as the derivative of yield function with respect to the plastic multiplier lambda ( $\lambda$ ).

$$h = -\frac{\partial f}{\partial \lambda} = \frac{\partial \sigma_c}{\partial \lambda} = -\left[ \frac{\partial D}{\partial \lambda} (\sigma_i - \sigma_f) \right] \quad (3-4)$$

Substituting D from equation 3-3

$$h = -\frac{\partial}{\partial \lambda} \Sigma \frac{\Delta \epsilon^p}{\epsilon_f^p} (\sigma_i - \sigma_f) \quad (3-5)$$

Substituting the value of final plastic strain ( $\epsilon_f^p$ )

$$\epsilon_f^p = D_1 (p^* + T^*)^{D_2} \quad (3-6)$$

in the equation 3-5, softening modulus is evaluated as

$$h = -\frac{1}{D_1 (P^* + T^*)^{D_2}} (\sigma_i - \sigma_f) \quad (3-7)$$

The  $P^*$  and  $T^*$  in equation 3-7 denote the normalized pressure and maximum tensile stress and have similar meanings as defined in equation 1-10. Substituting the values of  $\sigma_i$  and  $\sigma_f$  and assuming the value of constant  $C$  in  $\sigma_i$  and  $\sigma_f$  to be zero.

$$h = -\frac{1}{D_1 \left( \frac{p}{P_{HEL}} + \frac{T}{P_{HEL}} \right)^{D_2}} \left[ A \left( \frac{p}{P_{HEL}} + \frac{T}{P_{HEL}} \right)^N - B \left( \frac{p}{P_{HEL}} \right)^M \right] \quad (3-8)$$

where  $D_1$ ,  $D_2$ ,  $M$ ,  $N$ ,  $A$  and  $B$  are material constants for the JH2 model.  $p$  is the pressure,  $T$  is the maximum tensile hydrostatic pressure that the material can withstand and  $P_{HEL}$  is the pressure at the HEL (Hugoniot Elastic limit).

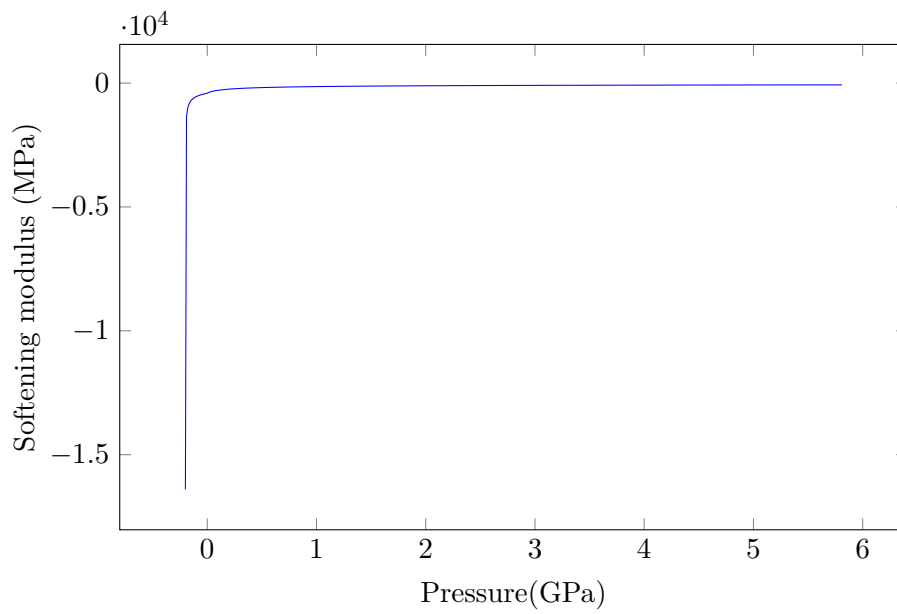


**Figure 3-1:** Softening modulus variation with pressure

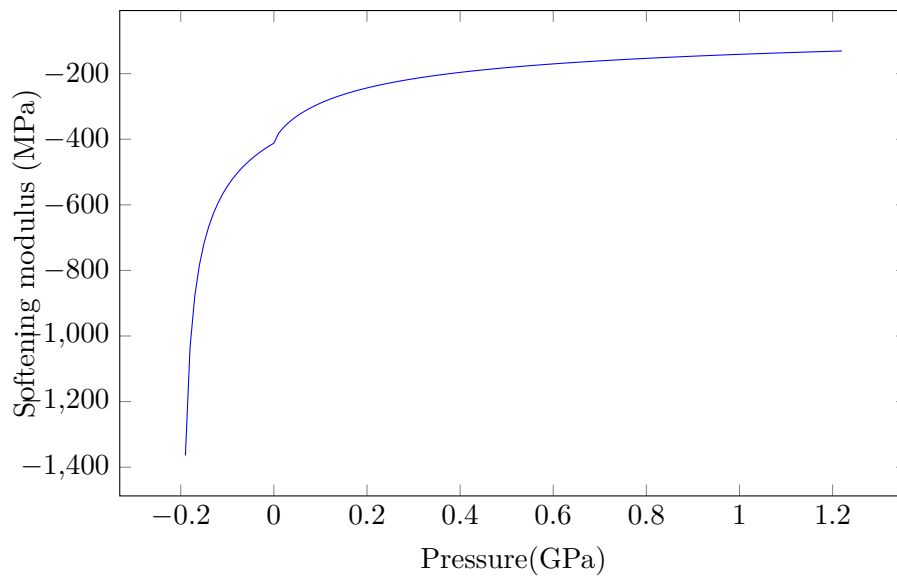


**Figure 3-2:** Softening modulus variation with pressure - zoomed

Figure 3-1 are the plots for the softening values found from equation 3-8 with  $D_1 = 0.005$ ,  $D_2 = 1.0$ ,  $T = 0.2$ ,  $C = 0$ ,  $B = 0.310$ ,  $M = 0.6$ ,  $A = 0.930$ ,  $N = 0.6$  and  $P_{HEL} = 1.460$  for Alumina [31]. The evaluation of equation 3-8 with above constants gives the magnitude of softening corresponding to pressure range of 0 to 1.2 GPa to be in range of 50 to 2000 MPa for JH2 model. The magnified plot corresponding to pressure range of 0 to 1.2 MPa is shown in Figure 3-2. It is observed that most of the softening occurs when the pressure is tensile, represented by negative values. The rate of increase in softening is steep till the pressure is negative, thereafter it is gradual within the pressure range of 0 to 0.2 GPa (Refer to 3-2). The rate of increase decreases further to low to very low for pressures larger than 0.2 GPa.

## 3-2 DP Model modified for pressure dependent softening

This section is about modification of standard DP model to incorporate the effects of pressure dependent softening. The governing equation for such a model is derived herein. Also, the associated numerical methods for the integration of the constitutive equations are described in detail.

### 3-2-1 Yield function

The shear strength of the material as considered in standard DP Model varies linearly with softening and plastic strain (Refer to equation 2-5). Hence, shear strength reduces by a constant rate ( $h$ ) with respect to the increase in plastic strain and is invariant on the stress state. In the modified DP model, the rate of degradation of shear strength is controlled via polynomial function  $h(\sigma)$  representing softening. The yield function for the modified DP yield formulation is

$$f = \sqrt{3J_2} - \eta p - \sigma^o (1 - \Sigma h(\sigma) \Delta \epsilon_{ps}), \quad (3-9)$$

where  $\sigma^o$  is shear strength of intact material defined as

$$\sigma^o = \frac{6 c' \cos \phi}{3 - \sin \phi} \quad (3-10)$$

The gradual softening is accounted for by the summation of plastic strain  $0 \leq \Sigma h(\sigma) \Delta \epsilon_{ps} \leq 1$ .  $J_2$  invariant of stress is defined as,

$$J_2 = \frac{1}{2} \sigma^T \mathbf{P} \sigma$$

$$p = -\frac{1}{3} I^T \sigma$$

where,  $\mathbf{P}$  and  $I$  are defined as

$$\mathbf{P} = \begin{bmatrix} \frac{2}{3} & -\frac{1}{3} & -\frac{1}{3} & 0 & 0 & 0 \\ -\frac{1}{3} & \frac{2}{3} & -\frac{1}{3} & 0 & 0 & 0 \\ -\frac{1}{3} & -\frac{1}{3} & \frac{2}{3} & 0 & 0 & 0 \\ 0 & 0 & 0 & -2 & 0 & 0 \\ 0 & 0 & 0 & 0 & -2 & 0 \\ 0 & 0 & 0 & 0 & 0 & -2 \end{bmatrix}, \quad I = \begin{bmatrix} 1 \\ 1 \\ 1 \\ 0 \\ 0 \\ 0 \end{bmatrix} \quad (3-11)$$

The rate of change of yield function is

$$\dot{f} = \frac{\partial f}{\partial \sigma} \dot{\sigma} + \frac{\partial f}{\partial \epsilon_{ps}} \frac{\partial \epsilon_{ps}}{\partial \lambda} \dot{\lambda} \quad (3-12)$$

$$\dot{f} = \mathbf{a}^T \dot{\boldsymbol{\sigma}} + \frac{\partial f}{\partial \epsilon_{ps}} \dot{\lambda} \quad (3-13)$$

where  $\lambda$  is the plastic multiplier and  $\mathbf{a}$  is the normal to the yield surface

$$\mathbf{a}^T = \frac{3}{2} \frac{\mathbf{P}\boldsymbol{\sigma}}{\sqrt{3J_2}} - \frac{1}{3} \eta \mathbf{I} + \frac{\partial h(\sigma)}{\partial \sigma} \sigma_0 \Delta \epsilon_{ps}$$

### 3-2-2 Plastic potential function

The plastic potential function is assumed similar to the one used in the standard DP model. The potential function for standard DP model is

$$g = \sqrt{3J_2} + \bar{\eta}p \quad (3-14)$$

$$(3-15)$$

The plastic strain is governed by the flow rule

$$\dot{\boldsymbol{\epsilon}}_p = \dot{\lambda} \frac{\partial g}{\partial \boldsymbol{\sigma}} = \dot{\lambda} \mathbf{b}. \quad (3-16)$$

Where  $\mathbf{b}$  is a vector normal to the potential function as given by,

$$\mathbf{b}^T = \frac{\partial g}{\partial \boldsymbol{\sigma}} = \frac{3}{2} \frac{\mathbf{P}\boldsymbol{\sigma}}{\sqrt{3J_2}} - \frac{1}{3} \eta \mathbf{I}$$

### 3-2-3 Stress Integration

In numerical modelling, the solution is computed incrementally, and the constitutive equations are integrated at each integration point for known stress, strain, plastic and trial strain. The first step is to use an elastic relationship to update the stress. If this updated stress is found to be within the yield surface, the material at the integration point is assumed to have either remained elastic or unloaded elastically from the yield surface, and there is no need to integrate the rate equation. However, if the calculated elastic stress lies outside the yield surface backward Euler algorithm or Apex return is used for stress integration to bring back the stress to the yield surface as shown in Figure 3-3. The resulting plastic strain is recorded.

### 3-2-4 Smooth return mapping formulation

The method is based on a one-step backward Euler integration of the evolution problem. Euler backward algorithm is unconditionally stable and provides very accurate results. However, it sometimes suffers from mesh sensitivity.

Figure 3-3 shows the trial stress and the return to current stress for the initial state either on the yield surface or inside the yield surface for Euler backward return. Previously converged

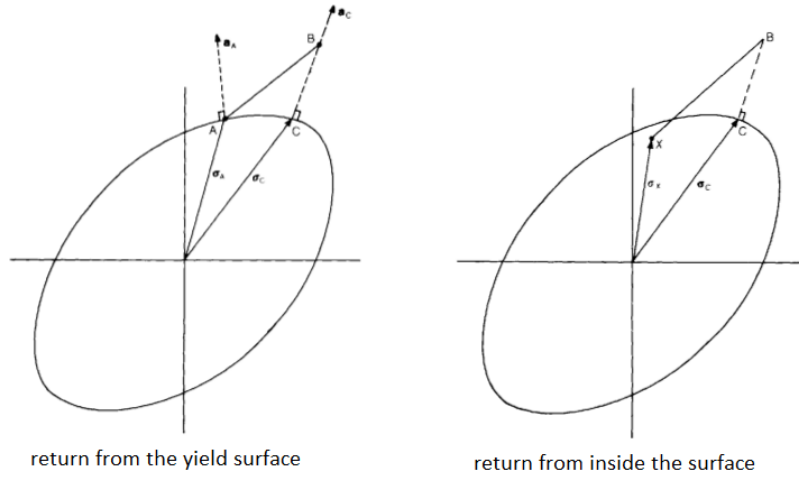


**Figure 3-3:** Euler backward return[6]

state is denoted by point  $A$ . The trial state is denoted by subscript  $B$ , while  $C$  stands for the current state. The current state of stress is calculated by subtracting the product of plastic multiplier ( $\lambda$ ), stiffness matrix  $\mathbf{C}$  and flow vector  $\mathbf{b}$  from the stress at trial state

$$\sigma = \sigma_{\mathbf{B}} - \Delta\lambda\mathbf{C}\mathbf{b} \quad (3-17)$$

The residual stress is calculated as

$$\mathbf{r} = \sigma - (\sigma_{\mathbf{B}} - \Delta\lambda\mathbf{C}\mathbf{b}) \quad (3-18)$$

From the truncated Taylor series for residual  $\mathbf{r}$

$$\Rightarrow \mathbf{r}_{\mathbf{n}} = \mathbf{r}_{\mathbf{0}} + \dot{\sigma} + \dot{\lambda}\mathbf{C}\mathbf{b} + \Delta\lambda\mathbf{C}\dot{\mathbf{b}} \quad (3-19)$$

where,

$$\dot{\mathbf{b}} = \frac{\partial\mathbf{b}}{\partial\sigma}\dot{\sigma} \quad (3-20)$$

Substituting  $\dot{\mathbf{b}}$  in previous equation

$$\mathbf{r}_{\mathbf{0}} + \dot{\lambda}\mathbf{C}\mathbf{b} = - \left( I + \Delta\lambda\mathbf{C}\frac{\partial\mathbf{b}}{\partial\sigma} \right) \dot{\sigma} \quad (3-21)$$

$$\Rightarrow \dot{\sigma} = - \left( I + \Delta\lambda\mathbf{C}\frac{\partial\mathbf{b}}{\partial\sigma} \right) (\mathbf{r}_{\mathbf{0}} + \dot{\lambda}\mathbf{C}\mathbf{b}) \quad (3-22)$$

$$\Rightarrow \dot{\sigma} = -\mathbf{Q}^{-1} (\mathbf{r}_{\mathbf{0}} + \dot{\lambda}\mathbf{C}\mathbf{b}) \quad (3-23)$$

where,

$$\mathbf{Q}^{-1} = \left( I + \Delta\lambda\mathbf{C}\frac{\partial\mathbf{b}}{\partial\sigma} \right)$$

Evaluating the derivative of the yield function

$$\dot{f} = f_{cn} - f_{c0} = \mathbf{a}^T \dot{\sigma} + \frac{\partial f}{\partial \epsilon_{ps}} \dot{\lambda} = 0 \quad (3-24)$$

$$\Rightarrow f_{cn} = f_{c0} + \mathbf{a}^T \dot{\sigma} + \frac{\partial f}{\partial \epsilon_{ps}} \dot{\lambda} \quad (3-25)$$

$\dot{\sigma}$  is substituted.

$$\Rightarrow f_{co} + \mathbf{a}^T \left( -\mathbf{Q}^{-1}r_0 - \mathbf{Q}^{-1}\dot{\lambda}\mathbf{C}\mathbf{b} \right) + \frac{\partial f}{\partial \epsilon_{ps}} \dot{\lambda} = 0 \quad (3-26)$$

Rearranging and simplifying plastic multiplier ( $\lambda$ ) is evaluated

$$\dot{\lambda} = \frac{f_{co} - \mathbf{a}^T \mathbf{Q}^{-1} r_0}{\mathbf{a}^T \mathbf{Q}^{-1} \mathbf{C} \mathbf{b} - \frac{\partial f}{\partial \Sigma \Delta \epsilon_{ps}}} \quad (3-27)$$

### 3-2-5 Consistent tangent matrix for smooth mapping return

The current stress is evaluated

$$\sigma = \sigma_B - \Delta \lambda \mathbf{C} \mathbf{b} \quad (3-28)$$

$$\Rightarrow \dot{\sigma} = \mathbf{C} \dot{\epsilon} - \Delta \lambda \mathbf{C} \frac{\partial \mathbf{b}}{\partial \sigma}, \dot{\sigma} - \dot{\lambda} \mathbf{C} \mathbf{b} \quad (3-29)$$

$$\Rightarrow \dot{\sigma} \left( I + \Delta \lambda \mathbf{C} \frac{\partial \mathbf{b}}{\partial \sigma} \right) = \mathbf{C} (\dot{\epsilon} - \dot{\lambda} \mathbf{b}) \quad (3-30)$$

$$\Rightarrow \dot{\sigma} = \mathbf{R} (\dot{\epsilon} - \dot{\lambda} \mathbf{b}) \quad (3-31)$$

Setting  $\mathbf{R}$  as,

$$\mathbf{R} = \left( I + \Delta \lambda \mathbf{C} \frac{\partial \mathbf{b}}{\partial \sigma} \right)^{-1} \mathbf{C} \quad (3-32)$$

Now the yield function is differentiated

$$\dot{f} = \mathbf{a}^T \dot{\sigma} + \frac{\partial f}{\partial \epsilon_{ps}} \dot{\lambda} = 0 \quad (3-33)$$

Again substituting  $\dot{\sigma}$

$$\Rightarrow \mathbf{a}^T \left( \mathbf{R} (\dot{\epsilon} - \dot{\lambda} \mathbf{b}) \right) + \frac{\partial f}{\partial \epsilon_{ps}} \dot{\lambda} = 0 \quad (3-34)$$

Rearranging to evaluate  $\dot{\lambda}$  and substituting in equation 3-31

$$\Rightarrow \dot{\lambda} = \left[ \frac{\mathbf{b} \mathbf{a}^T \mathbf{R}}{\mathbf{a}^T \mathbf{R} \mathbf{b} - \frac{\partial f}{\partial \epsilon_{ps}}} \right] \dot{\epsilon} \quad (3-35)$$

$$\Rightarrow \dot{\sigma} = \left[ \mathbf{R} - \frac{\mathbf{R} \mathbf{b} \mathbf{a}^T \mathbf{R}^{-1}}{\mathbf{a}^T \mathbf{R} \mathbf{b} - \frac{\partial f}{\partial \epsilon_{ps}}} \right] \dot{\epsilon} = 0 \quad (3-36)$$

Hence the Consistent Tangent Matrix is

$$\mathbf{C}_{ct} = \left[ \mathbf{R} - \frac{\mathbf{R} \mathbf{b} \mathbf{a}^T \mathbf{R}}{\mathbf{a}^T \mathbf{R} \mathbf{b} - \frac{\partial f}{\partial \epsilon_{ps}}} \right] \quad (3-37)$$

### 3-2-6 Apex return formulation

When the trial stress is within Zone 2 as shown in Figure 3-4, the differentiation of the yield surface does not have a unique direction. Apex return scheme is adopted from section 8.3 of the textbook by de Souza and Owens [7]. The selection of Apex return is done when the residual pressure is found negative. Residual pressure is found by summing up the trial pressure and the projection of the current cohesion on the pressure axis. The current state of pressure is brought to the apex of the DP cone by bringing the residual pressure to zero inside a Newton Raphson scheme as shown in Figure 3-4. The Newton Raphson scheme also updates the strain and pressure. Pressure is defined in terms of cohesion

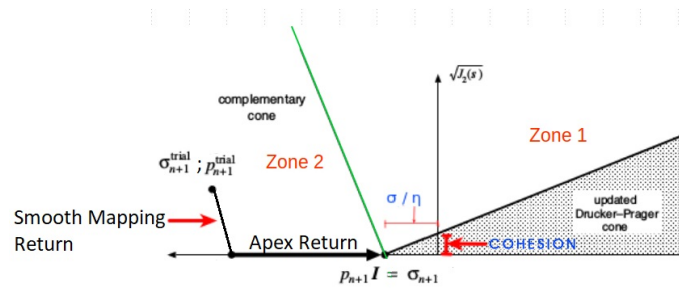


Figure 3-4: Apex return for Drucker Prager model [7]

$$p = \frac{c(\epsilon)}{\eta}. \quad (3-38)$$

$$p_{APEX} = -c(\epsilon_{ps} + \Delta\epsilon_{ps}) \quad (3-39)$$

where cohesion  $c$

$$c = \sigma^o (1 - \Sigma h(\sigma) \Delta\epsilon_{ps}) \quad (3-40)$$

Hence, Apex Pressure

$$p_{APEX} = -\sigma^o (1 - \Sigma h(\sigma) \Delta\epsilon_{ps}) \frac{1}{\eta} \quad (3-41)$$

Substituting the plastic strain with the volumetric plastic strain using the relation

$$\dot{\epsilon}_{ps} = \frac{\dot{\epsilon}_v^p}{\eta}$$

Apex pressure is defined as

$$p_{APEX} = -\sigma^o (1 - \Sigma h(\sigma) \Delta\epsilon_{ps}) \frac{1}{\eta} \quad (3-42)$$

The residual pressure is computed,

$$\mathbf{r} = \mathbf{p}_{n+1} - p_{APEX} \quad (3-43)$$

Substituting the current pressure

$$\mathbf{p}_{n+1} = \mathbf{p}^{trial} + K \Delta\epsilon_v^p \quad (3-44)$$

The residual pressure is evaluated as

$$\mathbf{r} = \mathbf{p}_{n+1}^{trial} - p_{APEX} + K \Delta \epsilon_v^p \quad (3-45)$$

$$\mathbf{r} = \mathbf{p}_{n+1}^{trial} + \sigma^o \left( 1 - h(\sigma) \frac{\epsilon_p^v}{\bar{\eta}} \right) \frac{1}{\eta} + K \Delta \epsilon_v^p \quad (3-46)$$

Derivative of residual pressure with respect to plastic strain

$$d = \frac{dr}{d\Delta \epsilon_v^p} \frac{d\Delta \epsilon_v^p}{d\epsilon} \quad (3-47)$$

$$\Rightarrow d = \left( \frac{1}{\bar{\eta}\eta} \frac{\partial h(\sigma)}{\partial \Delta \epsilon_v^p} \right) + K \quad (3-48)$$

The change in the volumetric plastic strain

$$\Delta \epsilon_p^v = \Delta \epsilon_p^v - \frac{r}{d} \quad (3-49)$$

The current plastic strain

$$\epsilon_{n+1}^p = \epsilon_n^p(0) + \Delta \epsilon_p^n = \epsilon_n^p(0) + \frac{\Delta \epsilon_p^v}{\bar{\eta}} \quad (3-50)$$

The updated current pressure

$$\mathbf{p}_{n+1} = \mathbf{p}_{n+1}^{trial} + K \Delta \epsilon_v^p \quad (3-51)$$

The updated residual pressure

$$\mathbf{r} = \mathbf{p}_{n+1} + \sigma^o \left( 1 - h(\sigma) \frac{\Sigma \Delta \epsilon_p^v}{\bar{\eta}} \right) \frac{1}{\eta} \quad (3-52)$$

The residual pressure is brought down within the tolerance and the current stress

$$\sigma = \mathbf{p}_{n+1} I \quad (3-53)$$

For non-dilatant flow ( $\psi = 0$ ), the return to apex does not make sense in the present formulation.

### 3-2-7 Consistent tangent matrix for apex return

The consistent tangent matrix defines the relation between the rate of stress and strain

$$\mathbf{C}^{ct} = \frac{\partial \sigma_{n+1}}{\partial \epsilon_{n+1}^e} = I \otimes \frac{\partial \mathbf{p}_{n+1}}{\partial \epsilon_{n+1}^{e\,trial}} \quad (3-54)$$

The current pressure is

$$\mathbf{p}_{n+1} = \mathbf{p}_{n+1}^{trial} + K \Delta \epsilon_v^p \quad (3-55)$$

$$d\mathbf{p}_{n+1} = K I : d\epsilon_{n+1}^{e\,trial} + K \Delta \epsilon_v^p. \quad (3-56)$$

The residual pressure is evaluated

$$dr = \left( \frac{\partial f}{\partial \epsilon_{ps}} + K \right) d\Delta \epsilon_v^p - K I : d\epsilon_{n+1}^{e\,trial} = 0 \quad (3-57)$$

$$\Rightarrow \frac{K}{\left( \frac{\partial f}{\partial \epsilon_{ps}} + K \right)} I : \epsilon_{n+1}^{e\,trial} = d\Delta \epsilon_v^p \quad (3-58)$$

Substituting the expression for residual pressure in change in pressure

$$\Rightarrow d\mathbf{p}_{n+1} = K I d\epsilon_{n+1}^{e\,trial} - K \frac{K}{\left( \frac{\sigma^o \partial f}{\partial \epsilon_{ps}} \eta + K \right)} I : d\epsilon_{n+1}^{e\,trial} \quad (3-59)$$

Hence, the consistent tangent matrix for the Apex return is ,

$$\mathbf{C}_{ct} = K \left( 1 - \frac{K}{\left( \frac{\partial f}{\partial \epsilon_{ps}} + K \right)} \right) I \otimes I \quad (3-60)$$

In the absence of hardening ( $h = 0$ ) the above tangent operator vanishes.

### 3-3 Verification

The verification of modified DP material formulation is done through unit cube test. The tensile force is induced via prescribed displacements. Values of material parameters except softening modulus is kept same as those for the standard DP material model. Pressure vs equivalent stress plot for the simulations is obtained to understand the effect of pressure dependent softening modulus. The softening of the material is defined as a cubic polynomial function of the pressure as shown in Figure 3-5.

$$h(\sigma) = a + bp + cp^2 + dp^3 \quad (3-61)$$

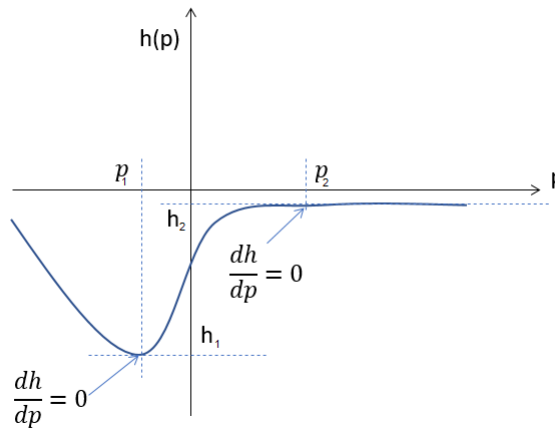


**Figure 3-5:** Cubic Polynomial function for pressure dependent strength

where the a, b, c and d are coefficients given as

$$a = \frac{3h_1p_1p_2^2 - h_1p_2^3 + h_2p_1^3 - 3h_2p_1^2p_2}{(p_1 - p_2)(r^2 - 2p_1p_2 + p_2^2)}$$

$$b = \frac{6p_1p_2(h_1 - h_2)}{(p_1 - p_2)(p_1^2 - 2p_1p_2 + p_2^2)}$$

$$c = \frac{3(h_1 - h_2)(p_1 + p_2)}{(p_1 - p_2)(p_1^2 - 2p_1p_2 + p_2^2)}$$

$$d = \frac{2(h_1 - h_2)}{p_1^3 - 3p_1^2p_2 + 3p_1p_2^2 - p_2^3}$$

where  $p_1$  and  $p_2$  are pressures corresponding to the maximum ( $h_1$ ) and minimum ( $h_2$ ) values of softening modulus as shown in Figure 3-5.

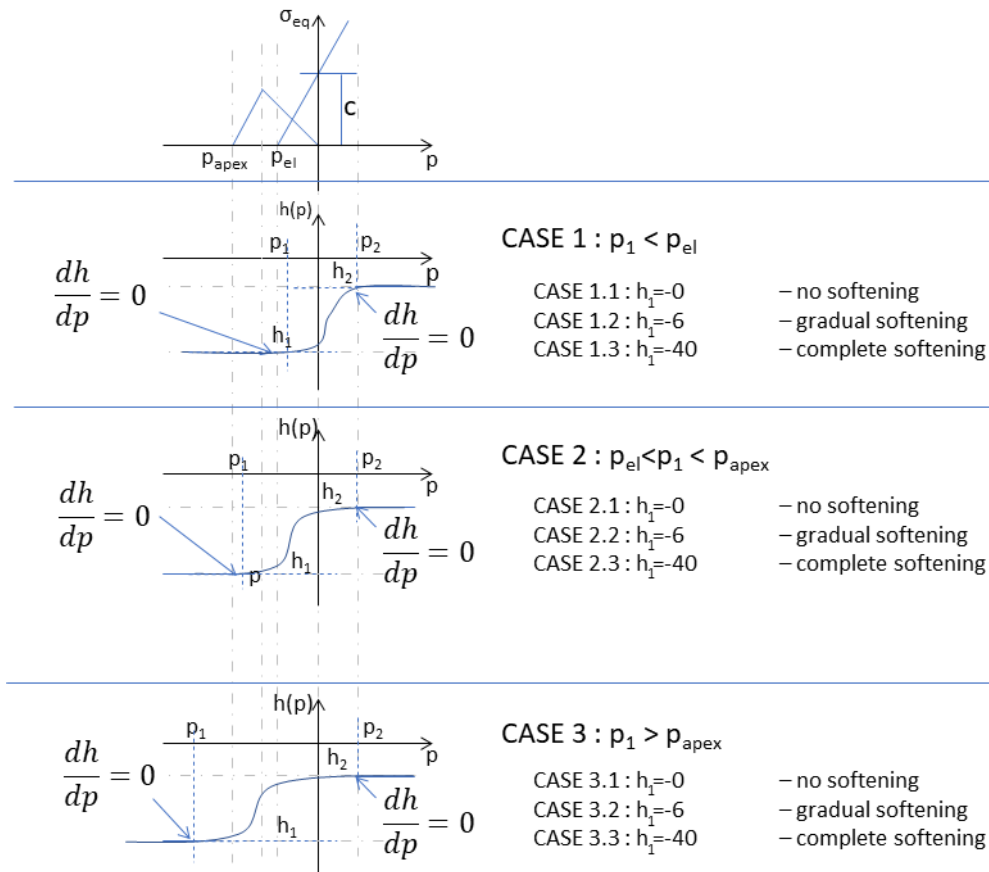


**Figure 3-6:** Cubic Polynomial function for pressure dependent strength

Based on the position of occurrence of maximum softening modulus with respect to  $p_{el}$  and  $p_{apex}$ , three distinct scenarios as presented in Figure 3-6, can be broadly thought of. These are as under:

1. Case-1 ( $p_{el} > p_1 > 0$ ): The maximum softening modulus is reached corresponding to a

tensile pressure value ( $p_1$ ) which is smaller than  $p_{el}$ . The material is yet to undergo plastic deformation at the time of occurrence of maximum softening. The output is nearly replicated to that of standard DP Model.

2. Case-2 ( $p_{apex} \geq p_1 \geq p_{el}$ ): The softening modulus attains its maximum within the pressure range of  $p_{el}$  to  $p_{apex}$ . At  $p_1 = p_{apex}$ , the softening curve approximates to the curve arrived through JH2 Model vide Figure 3-1.
  
3. Case-3 ( $p_{apex} > p_1$ ): Softening modulus reaches maximum value at pressures beyond  $p_{apex}$ . Since the pressure exceeds its limit  $p_{apex}$ , this case is physically improbable.

**Table 3-1:** Co-efficient for cubic polynomial

	<b>CASE 1.2</b>	<b>CASE 2.2</b>	<b>CASE 2.3</b>	<b>CASE 3.2</b>	<b>CASE 3.2a</b>	<b>CASE 3.3</b>
$p_2$	-0.5	-2.0	-2.0	-5.0	-5.0	-5.0
$p_1$	1.0	1.0	1.0	1.0	1.0	1.0
$h_1$	-6.0	-6.0	-40.0	-6.0	-40.0	-60.0
$h_2$	-0.5	-0.5	-0.5	-0.5	-0.5	-0.5
<b>a</b>	-4.6	-1.9	-10.7	-0.9	-3.4	-4.9
<b>b</b>	4.9	2.4	17.6	0.8	5.5	8.3
<b>c</b>	2.4	-0.6	-4.4	-0.3	-2.2	-3.3
<b>d</b>	-3.3	-0.4	-2.9	-0.1	-0.4	-0.6

The aforesaid scenarios are further subdivided into three subcases with respect to no softening, intermediate softening and large softening. Since all coefficients mentioned in equation 3-61 are zero for  $h_1 = h_2 = 0$ , therefore, sub-cases pertaining to intermediate and large softening, leaving the subcase related to no softening, are taken up for further studies. The computed values of coefficients  $a$ ,  $b$ ,  $c$  and  $d$  in polynomial function (equation 3-61) corresponding to intermediate and large softening for each of three cases mentioned earlier are presented in the Table 3-1.

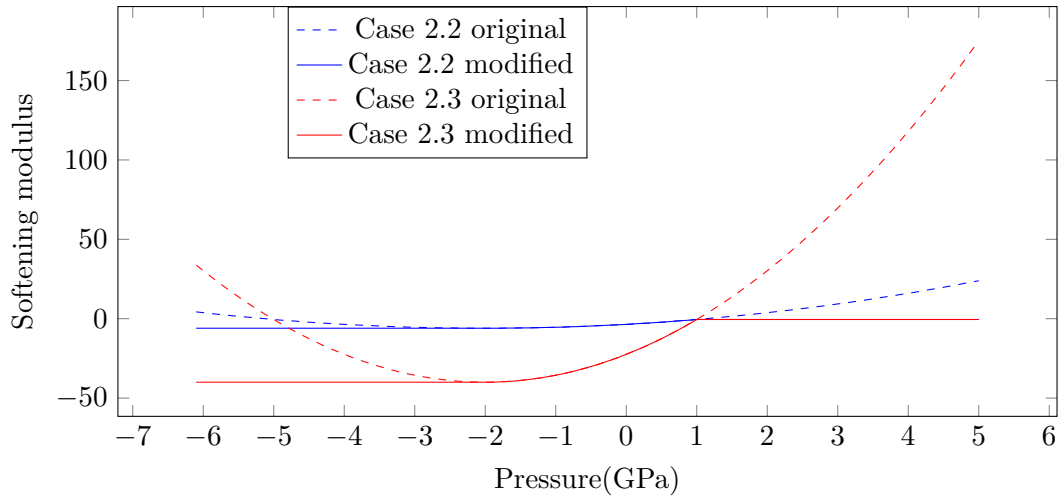


**Figure 3-7:** softening modulus vs pressure for Case 2

The equation 3-61 is depicted exactly by the softening versus pressure plot presented in Figure 3-5 and it is termed as 'original' hereinafter. The Figure 3-6 shows modified plots in which the original plots are tweaked to the extent that softening modulus is made constant for pressures larger than  $p_2$  and  $p_1$  in the domains of compression and tension respectively. The remaining part of the plot between pressure range  $p_1 - p_2$  is in accordance with equation 3-61. This modification in the plot is necessary to simulate the real behaviour of brittle material like ceramics which show large softening in tension.

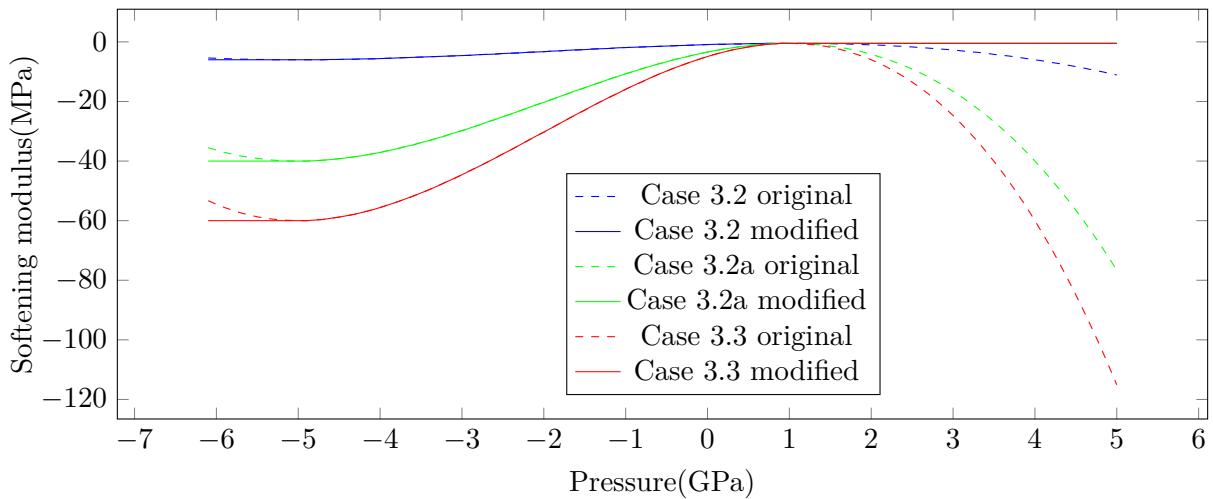


**Figure 3-8:** softening modulus vs pressure for Case 3

The original and modified plots corresponding to case-2 and 3 are presented in Figures 3-7 and 3-8 respectively with regards to intermediate and large softening. The values of coefficients  $a$ ,  $b$ ,  $c$  and  $d$  in respect of various subcases as presented in Table 3-1 are utilized to generate the respective plots. Subcases 2.2, 3.2 and 3.2a represent intermediate softening while subcases

2.3 and 3.3 represent large softening. Large softening is noticed at  $h_1 = -40$  for situation under case-2 but a similar value of softening is found to be in intermediate range for case-3. A larger value of  $h_1 = -60$  is observed to satisfy the conditions for large softening in respect of case-3.

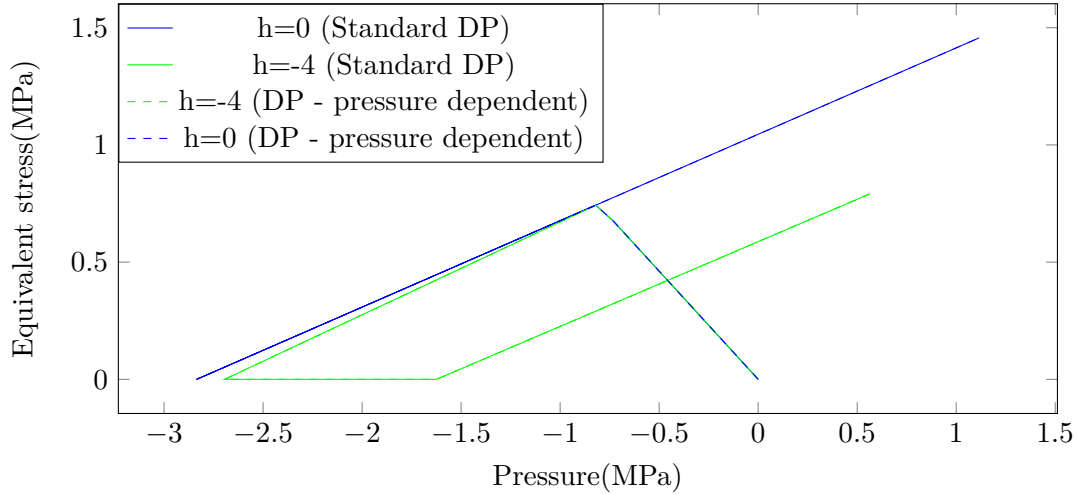


Figure 3-9: Equivalent stress vs pressure

The pressure dependent DP model is verified by plotting the limiting case pertaining to  $h = 0$  and  $-4$ . The plots so obtained is compared with the plots obtained from unit test explained in section 2-1 for Standard DP model keeping the values of softening ( $h$ ) same. The plots are shown in Figure 3-9. The plots are exact match and thus the pressure dependent DP model is verified.

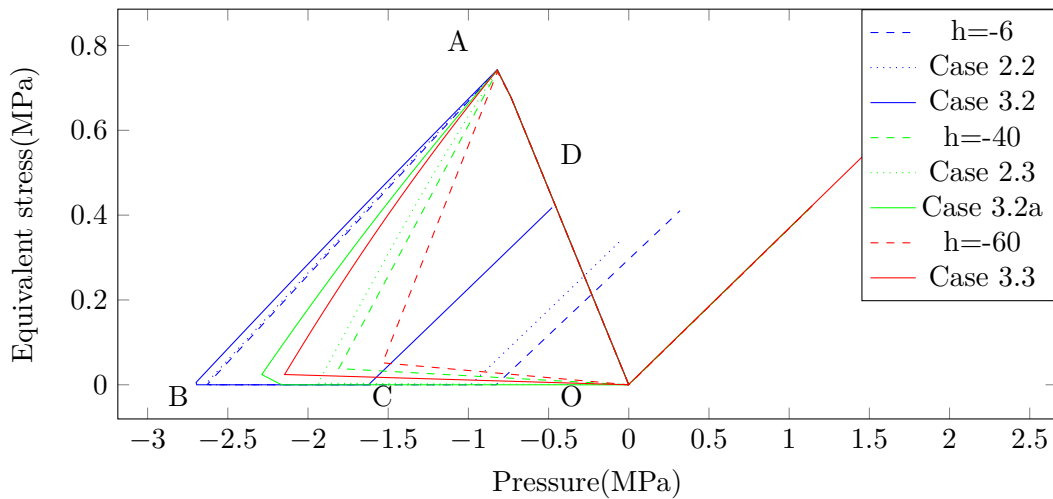
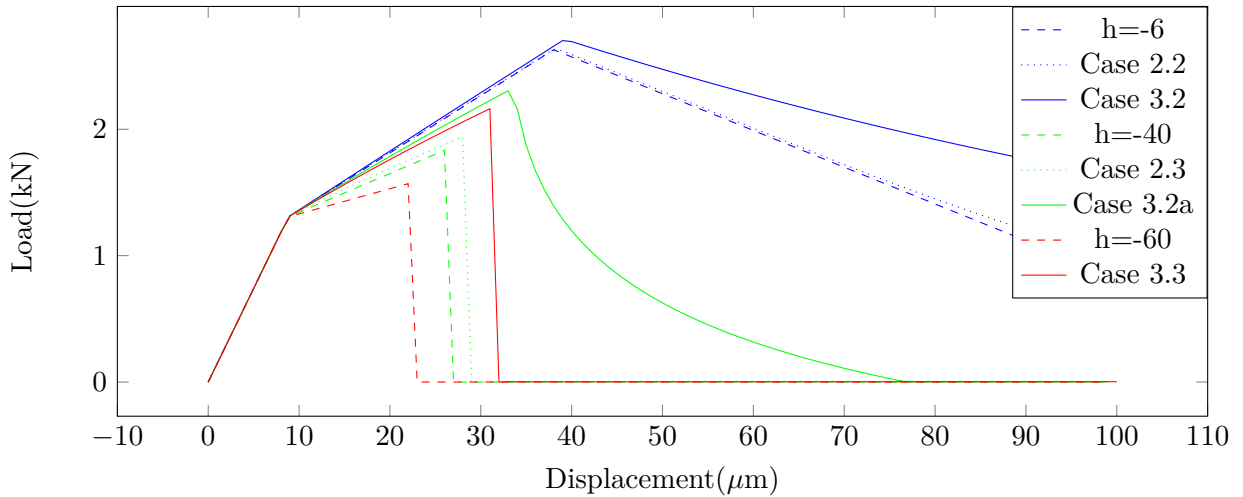


Figure 3-10: Equivalent stress vs pressure

Furthermore, to understand the effects of pressure dependent softening, unit cube tests corre-

sponding to a range of softening described by the pressure versus softening plots presented in Figure 3-7 and 3-8 are carried out. The pressure versus equivalent stress plots as outputs of unit cube tests corresponding to varying softening regimes are presented in Figure 3-10. The dashed lines show plots with respect to pressure independent softening represented by  $h_1 = -6, -40$  and  $-60$  in the legend. The plots pertaining to pressure dependent softening case-2 and 3 are in dotted and firm lines respectively. The plots within the elastic range OA remains the same for all. However, they start deviating beyond point A in the zone of plastic deformation. Reverse loading at the origin starts corresponding to large softening ( $h_1 = -60$  and case 2.3 and 3.3a) signaling complete degradation of the material. The apex pressure increases from case-2 to case-3.



**Figure 3-11:** Load v/s Displacement

The Figure 3-11 shows load v/s displacement diagram for only the loading cycle under prescribed tensile displacement. The material starts to show strength degradation for small and intermediate softening ( $h_1 = -6, \text{ case-2-2}$  and  $3-2$ ) at very large displacements as shown in the load-displacement diagrams (Figure 3-11). However, complete strength loss occurs at comparatively much smaller displacements for large softening irrespective of it being pressure dependent or not. But the displacement corresponding to complete strength loss under pressure dependent softening having its maximum value  $h_1$  is larger than that for pressure independent softening of magnitude equaling  $h$ . During the yielding process, the plot for case 3.2a shows the gradual decrease in the rate of softening unlike pressure independent softening plots, represented by  $h_1 = -8, -40$  and  $-60$ , which have constant slopes. The cases pertaining to very large softening show a sudden dip in the force implying that material has lost its entire strength. The effect of pressure dependent softening is more pronounced at intermediate magnitude of softening.

### 3-4 Indentation

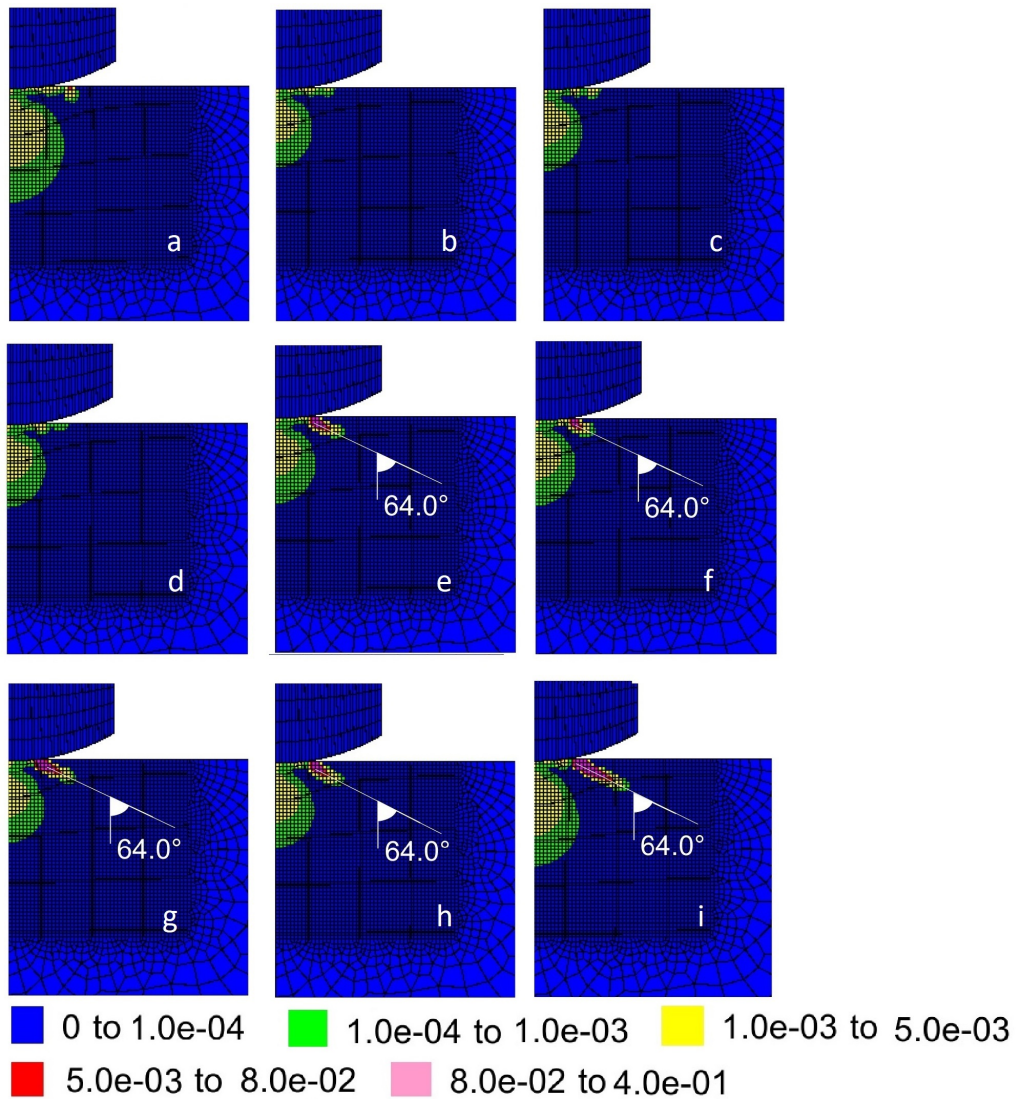


**Figure 3-12:** Equivalent Plastic Strain to variable softening - Indentation depth 25  $\mu\text{m}$

The indentation studies are carried out while keeping softening to be pressure dependent. The mesh, material properties, loading and boundary conditions etc. are similar to those considered for indentation under constant softening discussed in Chapter-2. The indentation depths of 25 and 40 micrometers are taken up for present studies. Indentation is done for each of the maximum softening ( $h_1$ ) values starting from -10 MPa to -90 MPa at intervals of -10 MPa while minimum softening ( $h_2$ ) is fixed at -0.5 MPa for all values of  $h_1$ . The meaning of  $h_1$  and  $h_2$  is the same as that explained in Figure 3-6. The pressure range  $p_{apex} = p_1$  (Case-2, Figure 3-6) is considered during indentation. The results of indentation so obtained are presented in Figures 3-12 and 3-13 for depths of 25 and 40 micrometers respectively.

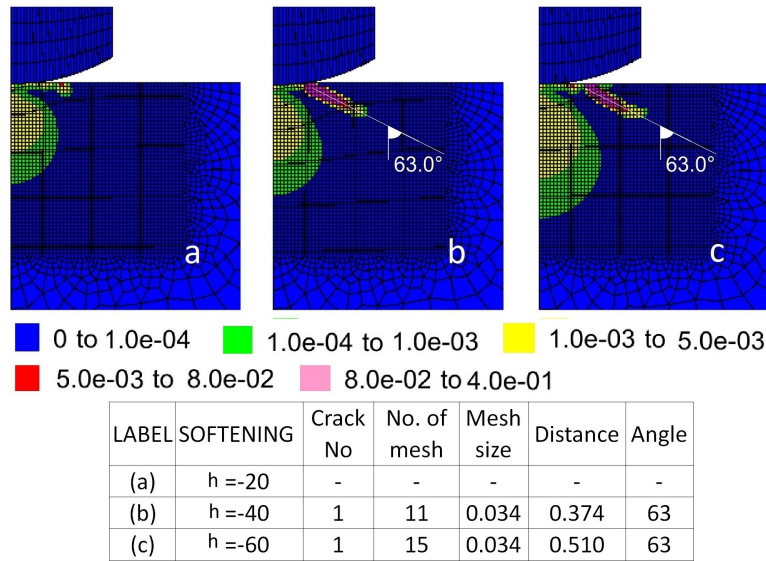


Figure 3-13: Equivalent Plastic Strain to variable softening - Indentation depth 40  $\mu\text{m}$

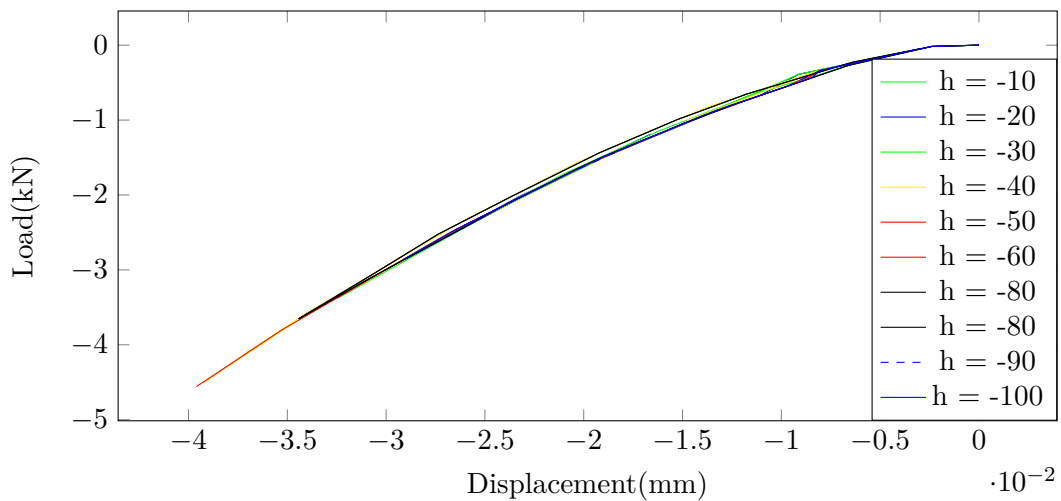


Figure 3-14: Force v/s Displacement plots for varying softening (h)

The half apex angle of cone crack is  $64^\circ$  for  $h_1 = -50$  and onwards for indentation depth of  $25 \mu\text{m}$ . However, The cracks form at lower softening of  $h_1 = -40$  for indentation depth of  $40 \mu\text{m}$ . The inclination of cracks decreases marginally to  $63^\circ$ . The distance of crack initiation point increases from  $0.374 \text{ mm}$  at  $h_1 = -50$  to  $0.476 \text{ mm}$  at  $h_1 = -90$  for indentation depth of  $25 \mu\text{m}$ . The increase in distance is more pronounced for indentation depth of  $40 \mu\text{m}$  and it occurs from  $0.374\text{mm}$  at  $h_1 = -40$  to  $0.510 \text{ mm}$  at  $h_1 = -60$ . The convergence is not achieved for softening values beyond  $h_1 = -90$  and the simulation terminates. The force displacement plots shown in Figure 3-14 are similar to that for standard DP model.

The results obtained for pressure independent softening (Figure 2-22) and pressure dependent softening (Figure 3-12) corresponding to indentation depth of  $25 \mu\text{m}$  are presented in the Table 3-2. Some interesting facts emerge out of the comparison of the two results. These are as follows:

**Table 3-2:** Comparative details of cone cracks for constant and pressure dependent softening

Label	h	No. of Mesh		Mesh Size		Distance		Angle	
		SDP	MDP	SDP	MDP	SDP	MDP	SDP	MDP
a	-10	-	-	-	-	-	-	-	-
b	-20	-	-	-	-	-	-	-	-
c	-30	-	-	-	-	-	-	-	-
d	-40	18	-	0.034	-	0.612	-	-	-
E	-50	17	11	0.034	0.034	0.578	0.374	-	-
F	-60	16	11	0.034	0.034	0.544	0.374	62	64
G	-70	13	11	0.034	0.034	0.442	0.374	62	64
H	-80	13	11	0.034	0.034	0.442	0.374	62	64
I	-90	13	14	0.034	0.034	0.442	0.476	62	64

1. The crack initiation and propagation is hindered by pressure dependent softening. The cone crack size decreases during indentation associated with pressure dependent softening when compared with constant softening. This contention is further supported by the indentation results obtained by simulation of standard DP Model based on pressure independent softening at  $h = -20$  and DP model modified to account for pressure dependent softening at  $h_1 = -20$  presented in Figure 3-15. The indentation depths during both simulations is  $40 \mu$  meter.

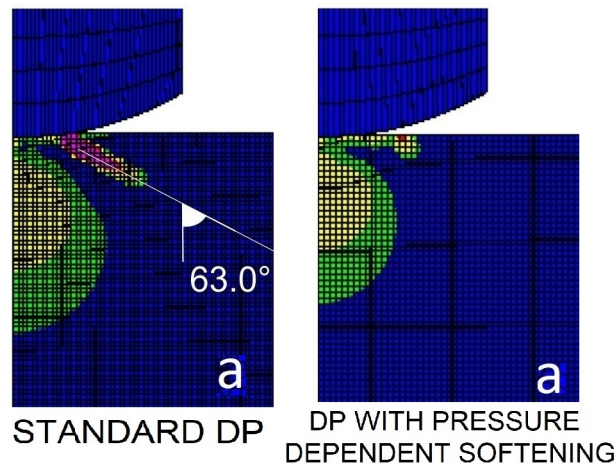


**Figure 3-15:** Equivalent Plastic Strain at Indentation depth  $40 \mu\text{m}$

2. The crack development is noticed at  $h_1 = -50$  for pressure dependent softening. This occurs at  $h = -40$  for constant softening
3. The distance of crack from the contact point decreased. The half cone apex angle increases marginally from  $62^\circ$  for pressure independent softening to  $64^\circ$  for pressure dependent softening.

### 3-5 Conclusion

The unit test results of modified DP model show that there is an increase in plasticity before strength degradation. This is based on the fact that displacement corresponding to complete strength loss under pressure dependent softening is more than that for pressure independent softening. Crack formation during indentation is delayed in the pressure-dependent regime of softening. Besides this, cracks initiation and propagation require larger pressure dependent softening in comparison to pressure independent softening. Both the increase in softening and indentation depth required for crack formation indicates towards the brittle behaviour of the material. Pressure dependent nature of ceramic has thus positive influence on its ability to become good armor protection. The addition of pressure dependent softening in the standard DP model is a step forward in numerically implementing the failure in ceramics. At very large softening ( $h_1 > -90$ ) convergence is not achieved.



# Modified Yield Function

The yield functions within the positive pressure range are linear for both Standard and Modified DP Models discussed in Chapters 2 and 3 respectively. This implies that the material strength keeps on increasing without any limit with the rise in pressure. But this is not true for real materials including ceramics [32], [9]. The material models developed by Walker and Anderson as well as Johnson, Holmquist and Biessel (JHB) impose a limit on the compressive strength of the material to overcome the problem of infinite strength. The Walker and Anderson model utilizes different functions for different pressure ranges to attain this objective. But the use of multiple yield functions results in the multiplicity of normals to the yield functions at the points of discontinuities of the derivatives of the yield function. The JHB model limits the strength through a continuous exponential function of intact and failed material strengths. This allows the JHB model to avoid the difficulties encountered in Walker and Anderson Model. The JHB model is discussed at length in Section 1-4. In view of the obvious advantage of JHB approach, an attempt is made in the present study to develop a continuous yield function on basic principles suggested by Drucker Prager (DP) but equipped to deal with the issue of infinite strength by developing and incorporating a suitable limiting mechanism to it.

### 4-1 Yield function

A typical yield surface considered for further studies is shown in Figure 4-1. It has three segments which are as follows:

(a) A straight line from its point of intercept  $(p_{apex}, 0)$  with pressure axis to the point  $(p_1, \sigma_1)$ : This part of yield surface is similar to the one adopted in standard DP model. (b) A parallel line to pressure axis at equivalent stress equal to limiting stress  $\sigma_{lim}$ : This line starts from point  $(p_2, \sigma_{lim})$ . (c) The transition between points  $(p_1, \sigma_1)$  and  $(p_2, \sigma_{lim})$  is achieved through an exponential function.

An attempt is made to develop a single equation to describe all three segments of yield surface with the objective that the three segments are parts of a continuous curve. In this backdrop,

a typical continuous yield function is presented in Equation 4-1. It has been derived by modifying DP yield function suitably by introducing new variables to account for the lim on compressive strength. Subsequently, the modified yield function is put to tests for validation.

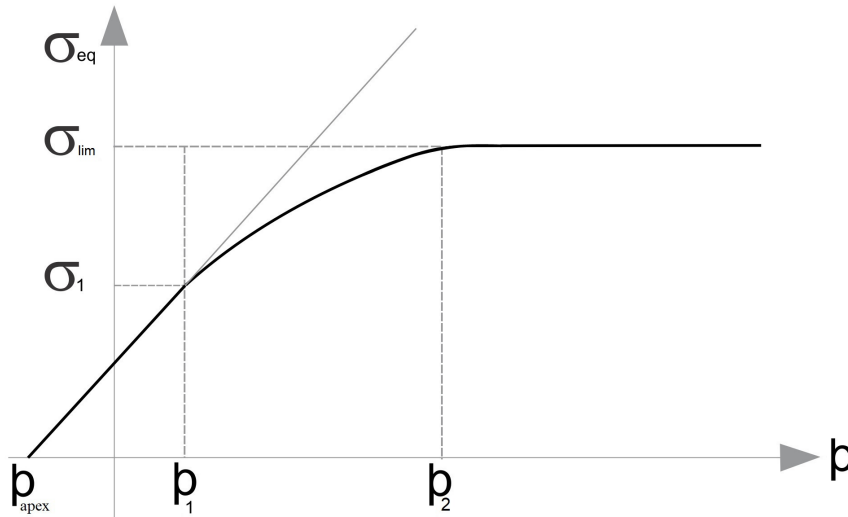


Figure 4-1: Modified Yield function

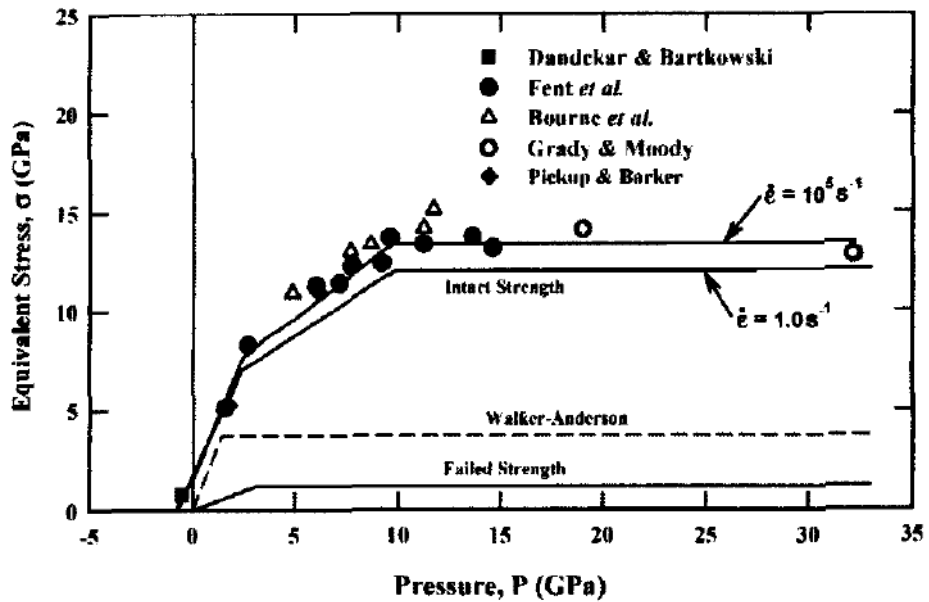


Figure 4-2: Original JHC model with Walker and Anderson failure surface [8]

The yield function modified as above is defined as a function of the limiting stress ( $\sigma_{lim}$ ),

limiting minimum value of pressure ( $p_{apex}$ ), stress and pressure at the point of deviation from linearity ( $\sigma_1, p_1$ ).

$$f_{mod} = \sigma_1 + (\sigma_{lim} - \sigma_1) \exp [1.0 - \alpha (p - p_1)] \quad (4-1)$$

where alpha is

$$\alpha = \frac{\sigma_1}{(\sigma_{lim} - \sigma_1)(p_1 - p_{apex})} \quad (4-2)$$

and  $\sigma_1$  is defined as,

$$\sigma_1 = -\eta p_1 - \zeta, \quad (4-3)$$

with  $\eta$  and  $\zeta$  defined the same as in chapter 2.

$$\eta = \frac{6 \sin \phi}{3 - \sin \phi} \quad \text{and} \quad \zeta = \frac{6 c \cos \phi}{3 - \sin \phi}. \quad (4-4)$$

The yield surface adopted in Walker and Anderson model [8] presented in Figure 4-2 provides a rough indication of the range of values for the  $p_1$  and  $\sigma_{lim}$  for silicon carbide. Similar values can also be assumed for alumina as a starting point as both have similar mechanical properties and failure mechanism and relevant data are not available in the literature for Alumina. The value of limiting stress is taken as 5.4 GPa for all the simulation in the next section on verification unless otherwise mentioned.

## 4-2 Verification

### 4-2-1 Cohesion

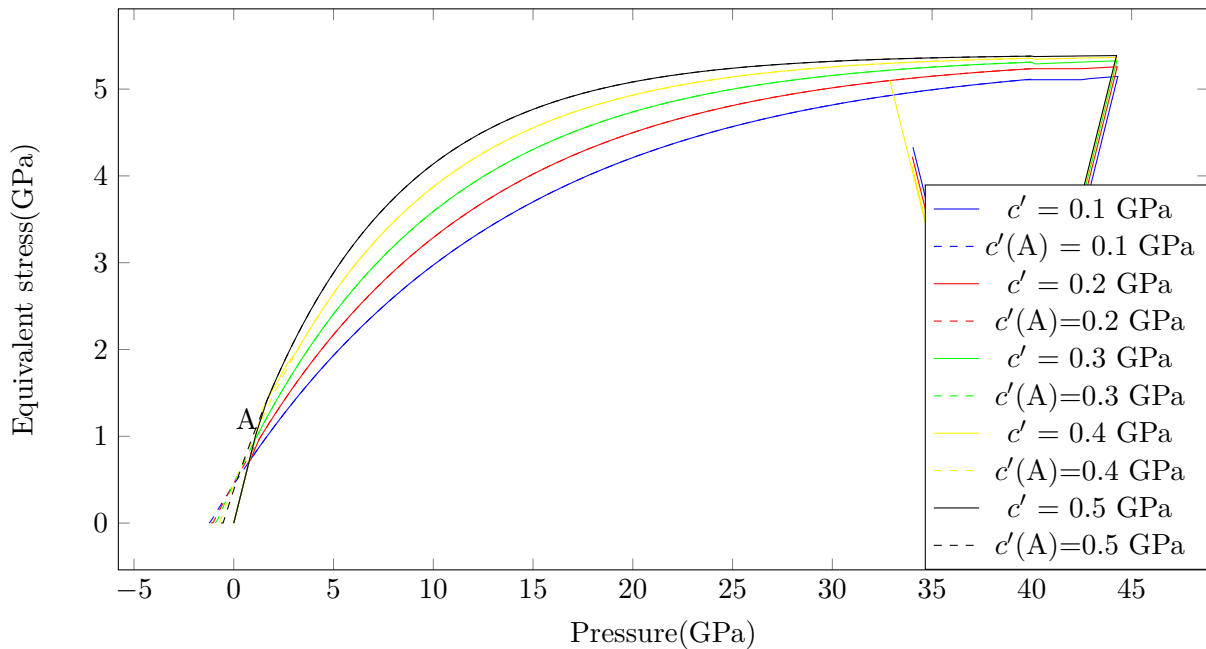


**Figure 4-3:** Unit load test on single cell (1 integration point) for varying cohesion and zero softening

The verification of modified yield function represented by Equation 4-1 is done through the unit test. The mesh, material properties, boundary condition (BC) and loading remains same as adopted in chapter 2. Since cohesion and angle of friction influence the yield surface primarily, compressive loading while varying these two parameters, is used for simulation as a tool for verification of yield function proposed vide Equation 4-1.

The analytical (vide equation 4-1) and simulated yield surfaces corresponding to different cohesion are presented in Figure 4-3. The softening is assumed to be absent for simplicity. The value of both angle of friction and dilatancy are taken as  $10^\circ$ . The analytical yield surfaces are in dashed lines and the simulated types are in firm lines for different cohesion values. Cohesion is directly proportional to limiting pressure ( $p_{apex}$ ) as per Equation 2-7, which governs the relationship between the two.

The analytical yield surfaces presented in Figure 4-3 are observed to follow this relationship as the points of intercepts of analytical yield surfaces on pressure axis are different for different cohesion values. These points of intercepts denote the limiting pressures ( $p_{apex}$ ). The intercepts corresponding to larger cohesions are farther from the origin i.e.  $p_{apex}$  increases with increase in cohesion. The intercepts of yield surfaces with the axis representing equivalent stress reflect the respective cohesions. Point A in Figure 4-3 represents the elastic limit on the yield surface. The analytical yield surfaces beyond elastic limit and within the plastic domain are curvilinear and deviate from the linear yield surface adopted in Standard DP Model shown in Figure 2-1. While equivalent stress (material strength) approaches  $\sigma_{lim}$ , the yield surfaces become near parallel to the pressure axis at high values of pressure. Thus the first objective of determining a function defining the continuous yield surface with limiting mechanism is achieved through Equation 4-1.

Beyond elastic limit and within the plastic domain, the simulated yield surfaces shown in firm lines are near match with analytical yield surfaces for respective cohesion. A small deviation between the two surfaces is observed between the pressure range corresponding to the elastic limit and  $\sigma_{lim}$ . This can be attributed to the snowball effect of the different degrees of precision considered for the analytical and simulation approaches. Nevertheless, the second objective of verification of Equation 4-1 is achieved.

#### 4-2-2 Angle of friction

The cohesion of the set of simulations to understand the effect of  $\phi$  is taken as 0.5 MPa.  $\phi$  is varied from  $0^\circ$  to  $30^\circ$  with an increment of  $10^\circ$ . Material strength increases as  $\phi$  increases, as a result, elasticity is prolonged and finally for  $\phi = 30^\circ$  plastic flow ceases completely as shown in black in Figure 4-4. The material yields completely at  $\phi = 0^\circ$  shown in blue and continues to deform with very little increase in stress.

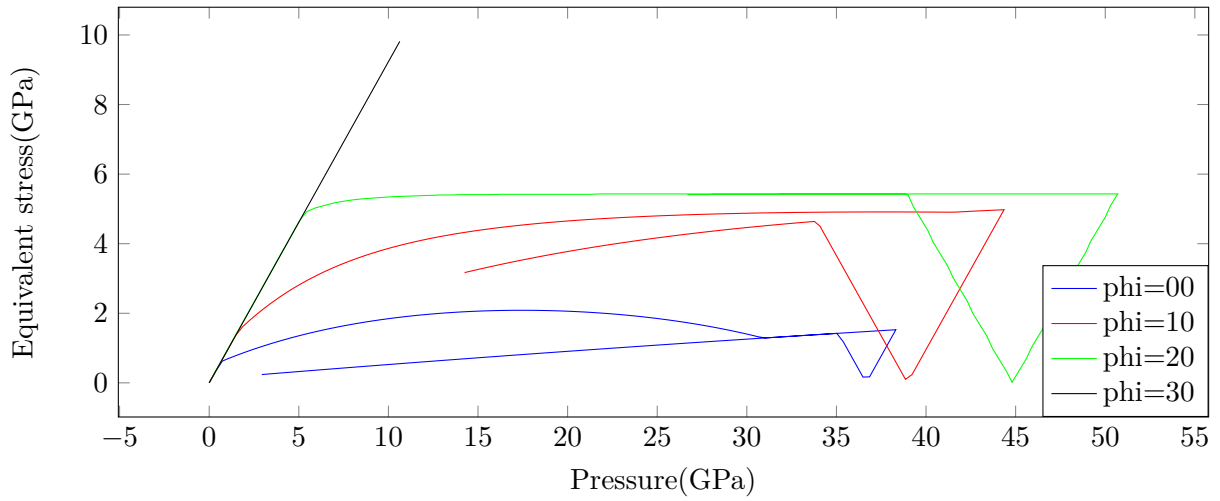


Figure 4-4: Unit load test for varying angle of friction( $\phi$ )

### 4-3 Yield Surface Comparison

The yield surfaces pertaining to models after Standard DP, JH, Walker and Anderson and Fent et. al besides the modified surfaces as per Equation 4-1 are presented in the Figure 4-5 [9]. The straight line in green represents the yield surface after Standard DP model. Yield surfaces corresponding to all models except Standard DP model have similar profiles. The two yield surfaces namely modified DP (1) and (2) are manifestation of Equation 4-1 pertaining to mimic failed and intact states respectively. The modified DP (1) and (2) surfaces follow Walker and Anderson surfaces for failed and intact states closely.

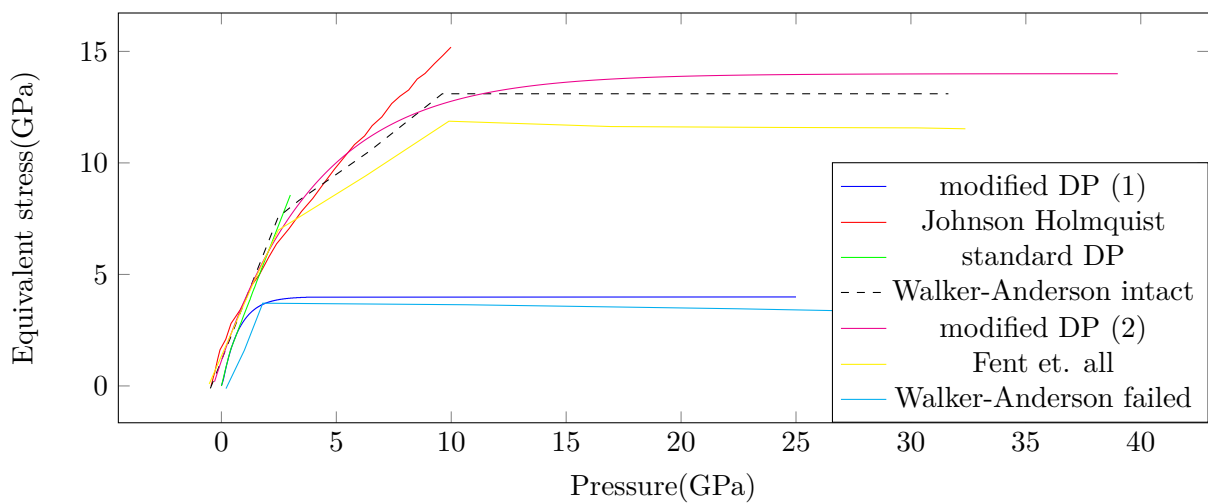
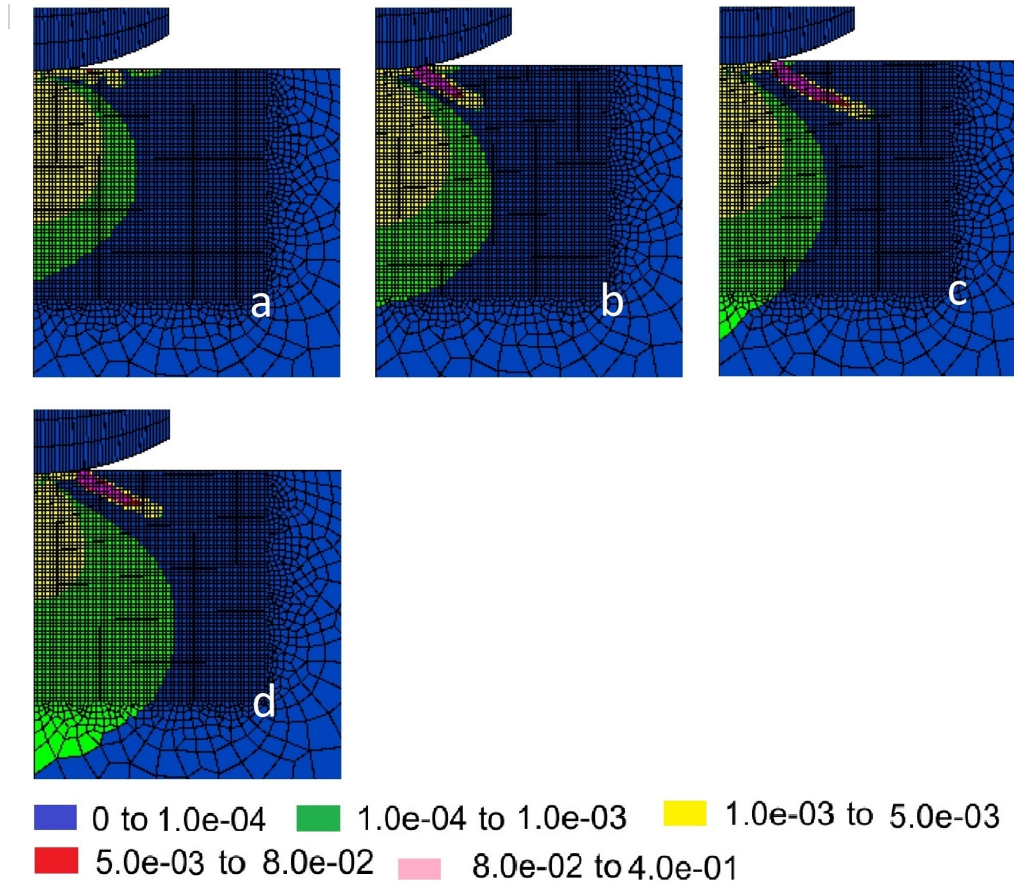


Figure 4-5: Yield function comparison between Literature and simulation[9]

#### 4-4 Indentation



LABEL	SOFTENING (h)	Crack No	No. of mesh	Mesh size	Distance	Angle
(a)	- 00	-	-	-	-	-
(b)	- 20	1	16	0.034	0.541	-
(c)	- 40	1	18	0.034	0.612	63
(d)	- 60	1	16	0.034	0.541	63

**Figure 4-6:** Indentation with varying softening for the modified yield surface DP(2)

In the present indentation study based on DP(2) yield function, the material properties, loading, boundary conditions etc. are kept the same as in the simulation for cone crack propagation by way of standard DP model presented in Chapter-2. The simulated plastic strain contours generated for an indentation depth of  $40 \mu\text{m}$  are presented in Figure 4-6. Softening is varied from 0 to -60 MPa at intervals of -20 MPa. The bulbous compressive plastic strain zone is seen to grow in size with increase in softening. This is a direct consequence of limit imposed on the material compressive strength through  $\sigma_{lim}$ .

The results of the present study are compared with those obtained through standard DP yield function presented in Figure 2-21. It is observed that there is little change in the extent of cone cracks or magnitude of the zone of plastic tensile strain. Convergence for  $h = -80$  could not be achieved. Same was the case with standard DP yield function discussed in Chapter-2 at an indentation depth of  $40 \mu\text{m}$ . To further understand the effect the current modification, simulation with same variations in softening is done with modified DP(1) yield function. The plastic strain contours are shown in Figure 4-7. The limiting value for the second yield function is much lower than the first one. Traces of ring crack are observed and cone cracks are completely absent. Since there is a significant reduction in strength, material yields in compression before tension. The failure is rather of ductile nature than Brittle.

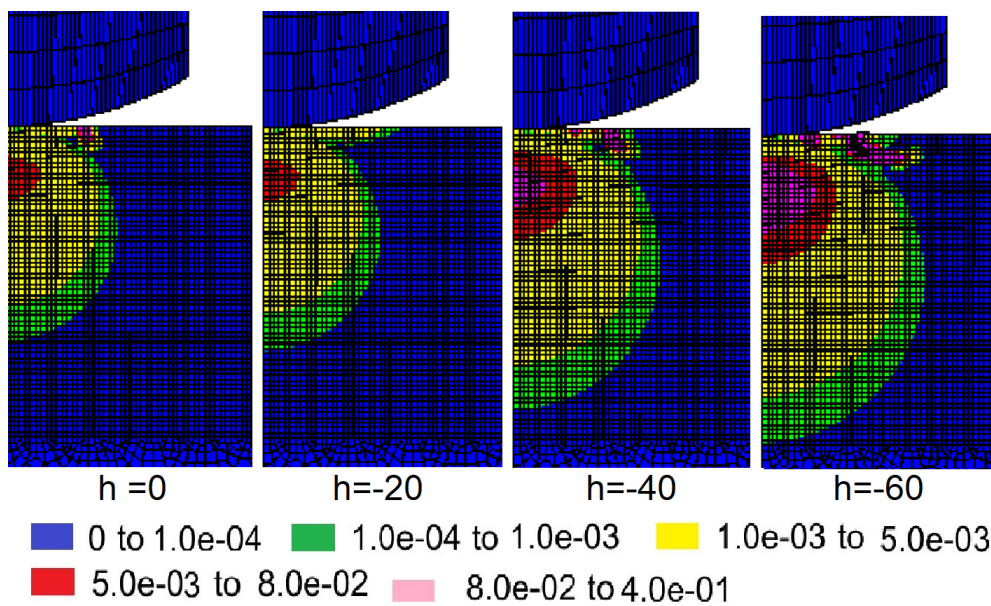


**Figure 4-7:** Indentation with varying softening for the modified yield surface DP(1)

## 4-5 Conclusion

The yield function vide equation 4-1 limiting the compressive strength to a finite value in conformity with the strength of real materials. It also gives results comparable to analytical formulas. The simulation results indicate that the modified DP(2) yield function does not affect the crack initiation and propagation in any different manner while compared with yield function of standard DP model. The major impact of the yield function DP(2) is observed on the size of the compressive plastic zone which grows bigger. However, upon using the modified DP(1) yield surface, which is essentially the yield surface for failed material, no crack is observed. This happens because the comparatively bigger volume of material is subjected to compressive stresses larger than material strength  $\sigma_{lim}$  vide equation 4-1, and thus the material yields in compression before failing in tension. Modifications to the yield surface

of the standard DP model allows the numerical model to be more accurate at simulating material behaviour.

# Mesh Sensitivity

The results obtained so far through DP based material model in the parametric study (section 2-3) are found to be mesh sensitive. Large variation in the sizes of zones of plastic strains pertaining to mesh divisions ranging from 30 to 80 at intervals of 10 is noticed in Figure 2-26. The cone crack sizes are also variable. Inconsistency of similar nature is most likely to occur in the results obtained from simulations of DP models modified for pressure dependent softening and modified yield function. Larger mesh sizes require less computation time but the accuracy of the results may be compromised. Smaller mesh size sometimes do not allow convergence during the simulation. Hence judging the results pertaining to a particular mesh size or division becomes a tricky affair. The selection of appropriate mesh size/division becomes too important. Studies done by Wang, Sluys and Borst [33], [34] predict that incorporation of viscoplasticity parameters in the material model can solve mesh sensitivity and provide a uniform and consistent solution across the mesh size.

### 5-1 Viscoplasticity

Materials undergo permanent deformation during plastic state under the influence of external loads. Plastic deformation coupled with creep flow on application of load is defined as viscoplasticity. The rate of change of plastic strain with respect to time is a key parameter to understand viscoplasticity. In other words, it is a concept based on rate dependent plastic behaviour of solids. A combination of sliding frictional element and non linear dashpot describes viscoplasticity well. The former represent plasticity while the rate dependent characteristics are attributed to the later.

### 5-2 Integration of Viscoplasticity in DP Model

Time dependent viscosity coefficient introduced by Perzyna, has been integrated with the basic formulation of standard DP Model in the present study. The algorithm based on the

works of Sluys and Wang [33] is utilized for integration of viscosity coefficient with standard DP material model. The response of ceramics is evaluated by the techniques of rate independent plasticity after adding strain rate dependence to the yield stress. The constitutive equations are derived as follows:

Rate of change of total strain with respect to time is the sum of rates of change in elastic and viscoplastic strains.

$$\dot{\epsilon} = \dot{\epsilon}^e + \dot{\epsilon}^{vp} \quad (5-1)$$

$\epsilon^{vp}$  denotes the viscoplastic component of strain and  $\dot{\epsilon}^{vp}$  is the rate of change viscoplastic strain. Subsequently, rate of change of stress is calculated as

$$\dot{\sigma} = \mathbf{D}^e (\dot{\epsilon} - \dot{\epsilon}^{vp}) \quad (5-2)$$

The rate of change of plastic strain  $\dot{\epsilon}^{vp}$  is defined as

$$\dot{\epsilon}^{vp} = \dot{\lambda} \mathbf{m} \quad (5-3)$$

where the rate of change of plastic multiplier  $\dot{\lambda}$  is defined as

$$\dot{\lambda} = \mu \langle \phi(f) \rangle \quad (5-4)$$

where  $\lambda$  is the plastic multiplier and  $m$  is defined as the derivative of viscoplastic potential function ( $g$ ).

$$\mathbf{m} = \frac{\partial g^{vp}}{\partial \sigma} \quad (5-5)$$

Furthermore,  $\phi$  determines the regularizing effect of the viscoplastic model.  $\phi$  is defined as

$$\phi(\sigma) = \left[ \frac{\langle f \rangle}{\sigma_o} \right]^N \quad (5-6)$$

$\langle \rangle$  represents the ramp function. The value of constant  $N$  is taken 1 for simplicity. The change in stress is calculated by the product of the elastic stiffness matrix and the change in elastic strain.

$$\Delta\sigma = \mathbf{D}^e (\Delta\epsilon - \Delta\epsilon^{vp}) \quad (5-7)$$

The viscoplastic flow is determined by the gradient of the yield surface at time  $t + \Delta t$ . The incremental viscoplastic strain is defined as,

$$\Delta\epsilon^{vp} = \Delta\lambda \mathbf{m}_{t+\Delta t} \quad (5-8)$$

Substituting the incremental viscoplastic strain in incremental stress

$$\Delta\sigma = \mathbf{D}^e [\Delta\epsilon - \Delta\lambda \mathbf{m}_{t+\Delta t}] \quad (5-9)$$

The Newton Raphson scheme is controlled by the residual  $r$  calculated as

$$r = \phi - \frac{\Delta\lambda}{\mu\Delta t} \quad (5-10)$$

Differentiating the equation 5-9 and getting rid of the subscripts

$$\delta\sigma = \mathbf{P}\delta\epsilon - \mathbf{P} \left[ \mathbf{m} + \Delta\lambda \frac{\partial \mathbf{m}}{\partial \lambda} \right] \delta\lambda \quad (5-11)$$

The incremental strain  $\delta\epsilon$  is zero in the local iteration.  $\mathbf{P}$  is defined as

$$\mathbf{P} = \left[ (\mathbf{D}^e)^{-1} + \Delta\lambda \frac{\partial \mathbf{m}}{\partial \sigma} \right]^{-1} \quad (5-12)$$

Differentiating the residual of Newton Rapshon control loop

$$\delta r = \left[ \frac{\partial \phi}{\partial \sigma} \right]^T \delta\sigma + \left[ \frac{\partial \phi}{\partial \lambda} - \frac{1}{\eta \Delta t} \right] \delta\lambda \quad (5-13)$$

Substituting the incremental stress  $\delta\sigma$  from equation 5-11 and rearranging to evaluate  $\lambda$

$$\delta\lambda = \frac{1}{\alpha} \left[ \left( \frac{\partial \phi}{\partial \sigma} \right)^T \mathbf{P} \delta\epsilon - \delta r \right] \quad (5-14)$$

Where  $\alpha$  is defined as

$$\alpha = \left[ \frac{\partial \phi}{\partial \sigma} \right]^T \mathbf{P} \left[ \partial \mathbf{m} + \Delta\lambda \frac{\partial \mathbf{m}}{\partial \lambda} \right] + \frac{1}{\mu \Delta t} - \frac{\partial \phi}{\partial \lambda} \quad (5-15)$$

where,

$$\begin{aligned} \frac{\partial \phi}{\partial \lambda} &= \frac{h}{\sigma_0} \\ \frac{\partial \phi}{\partial \sigma} &= n \\ \frac{\partial m}{\partial \lambda} &= 0 \end{aligned}$$

with  $m$  a function of only stress. Substituting values,

$$\alpha = n^T \mathbf{P} \mathbf{m} + \frac{1}{\mu \Delta t} - \frac{h}{\sigma_0} \quad (5-16)$$

The tangent stiffness matrix is evaluated by substituting  $\delta\lambda$  in equation 5-11

$$\mathbf{D}^{vp} = \mathbf{P} - \frac{1}{\alpha} \mathbf{P} \mathbf{m} n^T \mathbf{P} \quad (5-17)$$

### 5-3 Verification

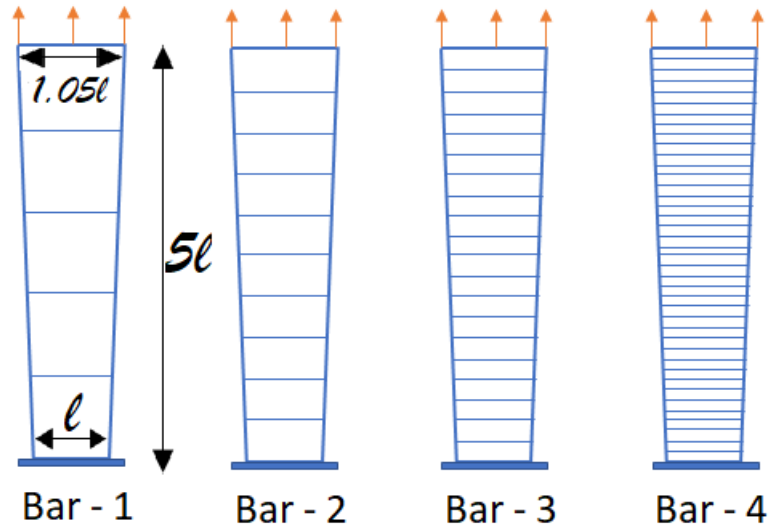


Figure 5-1: Mesh for bar in tension

The performance of viscoplasticity integrated DP model is examined by comparison of its results with those of standard DP model for a tapered bar in tension. The basic material properties of the tapered bar are the same as considered in previous chapters. The dimension  $l$  shown in Figure 5-1 is 1 mm. Top edge width of the tapered bar is 1.05 times the bottom edge. The bar is meshed in four different ways as shown in Figure 5-1. Bar-1 has five divisions which,

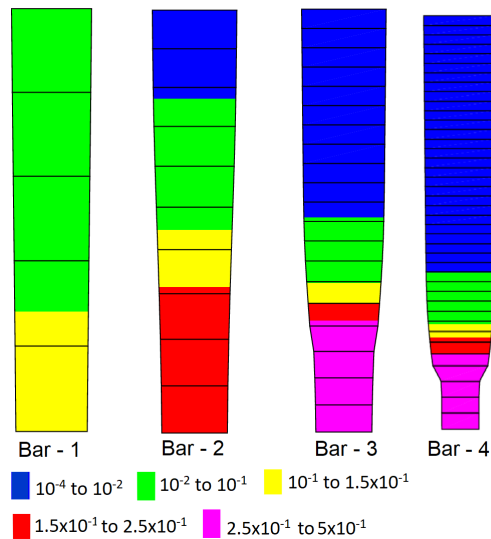
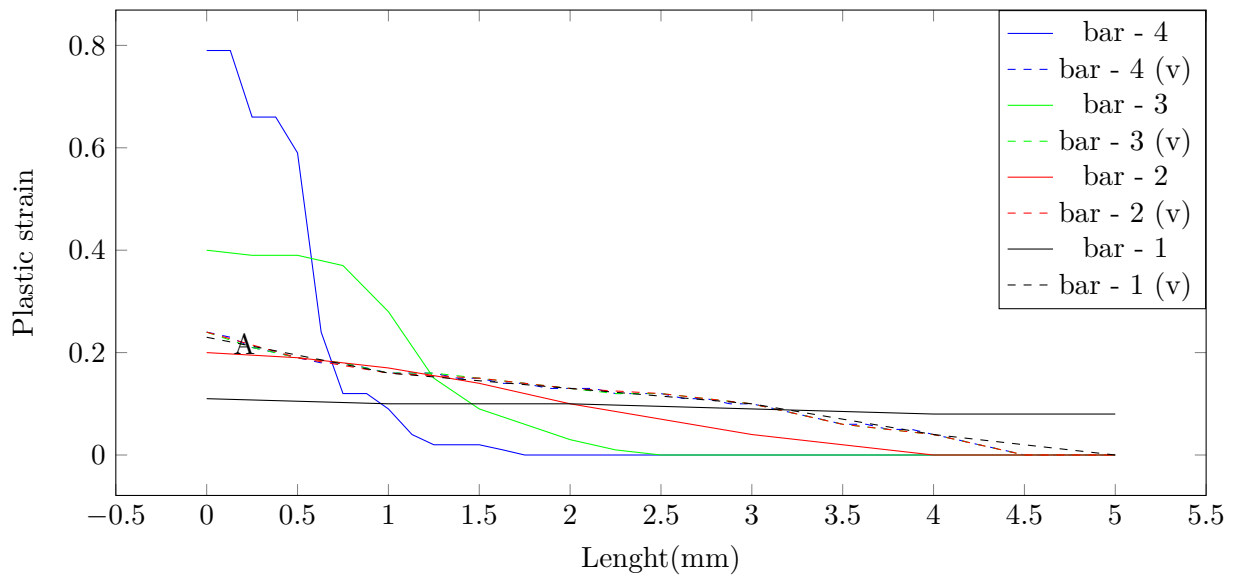


Figure 5-2: plastic strain for tension bar with standard DP model

are doubled in every next bar. The no. of divisions in bar-4 thus reaches to 40 following this

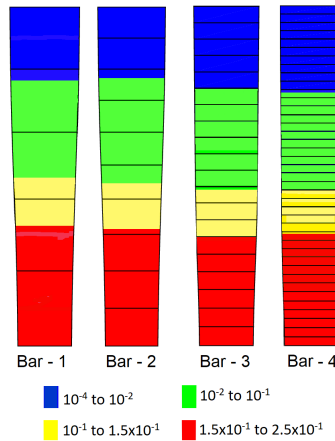
rule. The comparison is made for associative plasticity at  $\phi = \psi = 10^\circ$  and softening  $h = -2$  GPa. The viscosity coefficient  $\mu$  is taken as 10 MPa.s and  $\Delta t$  as 0.09s.

Figure 5-2 shows the plots of plastic strain for bar-1 to bar-4. The variations in plastic strain undergone by the bar no. 1 to 4 are very high. Bar with smaller mesh size develops a larger plastic strain for a given loading history. There are also large variations in the magnitudes of maximum strain. The strain in bar-4 is four higher times than that in bar-1 indicating lack of uniformity in deformation patterns of bars-1 to 4. Above all, convergence is not achieved for bar-4 during simulation for entire 100 load steps and the plastic strain contour with a local failure shown in Figure 5-2 is at load step 91.



**Figure 5-3:** Plastic strain variation along the length of tension bar

The plots showing variation of plastic strain as arrived through standard DP and viscoplastic DP models, over the bar length are presented in Figure 5-3 for comparative study. The firm and dashed lines represent the outputs of standard and viscoplastic DP models respectively. The deformation profiles of the tapered bars in tension through viscoplasticity integrated DP model are shown in Figure 5-4. Though the properties and load conditions are the same for all the bars, the strains developed in each bar as determined through standard DP Model have very large variations particularly in the bottom half of bar lengths. The standard DP plot pertaining to bar-4, which has largest no. of division, indicates local failure slightly above the bottom. The bar-1 with least divisions seems to undergo gradual strain change along its length. These outcomes highlight the limitations of standard DP model with regards to mesh sensitivity. On the other hand, the simulated plastic strain profiles as arrived through viscoplasticity integrated DP model as shown in Figure 5-4 almost overlap each other, exhibiting uniformity in the magnitudes of strains and deformations (Figure 5-3) undergone by each of the four bars irrespective of mesh size or division.



**Figure 5-4:** plastic strain for tension bar with standard DP model

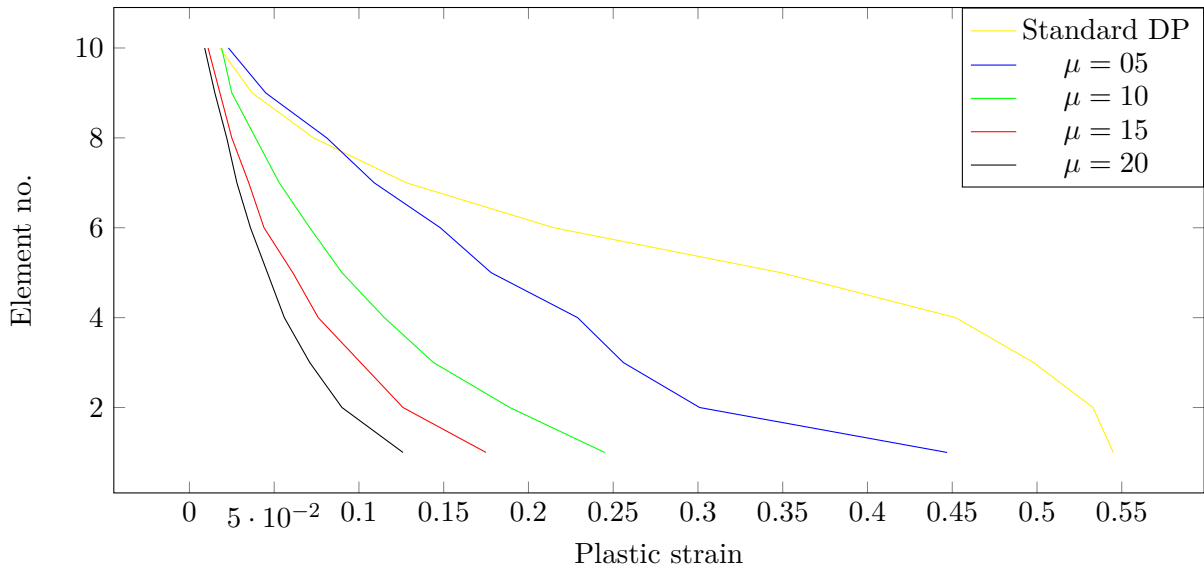


**Figure 5-5:** Max plastic strain along the height of bar.

The outputs presented in Figures 5-2 to 5-4, are based on a constant viscosity of 10 MPa.s. Therefore, it is important to understand the effect of varying viscosity on mesh sensitivity. Accordingly, simulations are carried out corresponding to viscosity coefficients ranging from 0 to 20 MPa.s at intervals of 5 MPa.s for bar-2, which has 10 divisions. The bottom-most element in contact with the support is designated as element number 1. Other elements are assigned numbers in increasing order going up to 10 for the uppermost element. The plastic strain plotted is average of plastic strains across the 4 nodes constituting the element. Figure 5-5 shows the profiles of plastic strain and respective element number. Viscosity coefficient equaling to zero corresponds to the standard DP model. The profile corresponding to standard DP model ( $\mu = 0$ ) show largest of plastic strains in all elements, while the profile of  $\mu = 20$  MPa.s shows the smallest strain. The explanation lies in the fact that viscosity coefficient controls the dissipation and its increase causes a decrease in the plastic strain. The plots

pertaining to  $\mu = 0$  and 5 MPa.s reveals that the strain change along the elements is large. But it is somewhat gradual for  $\mu = 10$  MPa.s or more, exhibiting gradual strain change. Among gradually changing profiles, it is the closest to the standard DP profile.

## 5-4 Indentation

The focus of this section is to ascertain the performance of the viscoplasticity based model in solving mesh sensitivity. Simulation of indentation of the target with mesh structures of 40, 50, 60 and 70 divisions is performed. The inputs are softening  $h = -30$  MPa, friction angle =  $70^\circ$ , dilatancy =  $15^\circ$  and viscosity coefficient  $\mu = 10$  MPa.s. The loading and boundary conditions are kept the same as in the section 2-3-4. Among the simulated results corresponding to  $\mu = 5, 10, 15$  MPa.s, those related with  $\mu = 10$  MPa.s was found to be most promising during preliminary studies. Therefore, it was chosen for taking up further works in the current studies. The outputs of indentation tests simulated through viscoplastic DP model are presented in respect of mesh divisions from 40 to 70 at intervals of 10 in Figure 5-6. All simulations reach the approximately same indentation depth close to  $40 \mu\text{m}$ , and the compressive strain zones below indenter are fairly consistent in size. The variation in crack sizes corresponding to different mesh divisions is also marginal, if compared with outputs presented in Figure 2-26 (Standard DP model). However, there is variation in crack shape. The crack for mesh with 70 divisions is narrow compared to the rest. No clear pattern could be identified in respect of crack orientation. Figure 5-7 shows the plastic strain contours for mesh with 40 divisions for standard DP model and viscoplastic DP model. The cone crack is observed to form through the later but is missing through the former. The plastic strain in the bulbous zone is also significantly larger for the viscoplastic DP model.

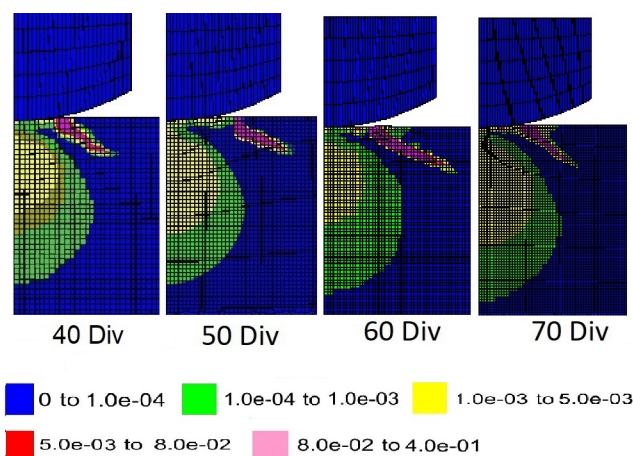


**Figure 5-6:** plastic strain for variation in mesh size

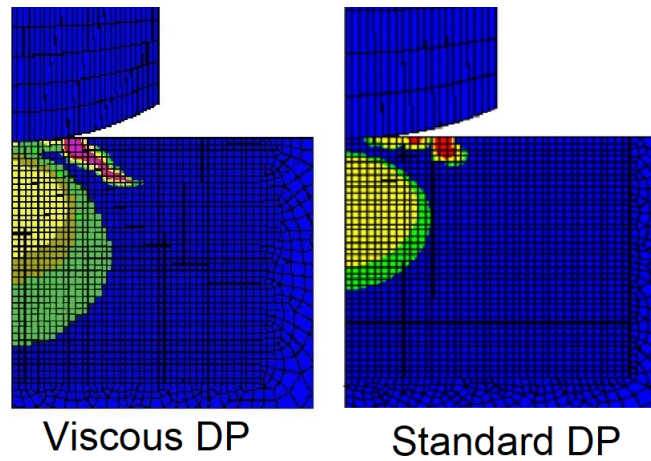


**Figure 5-7:** plastic strain for variation in mesh size with 40 divisions

## 5-5 Conclusion

The integration of viscoplasticity with standard DP model overcomes the mesh sensitivity to a large extent, and produces acceptable results for the tension bar. There is consistency in the cone crack size during indentation at variable mesh divisions but crack shapes vary. It is concluded that integration of viscoplasticity to the standard DP model is a positive step in mitigating mesh sensitivity. Further study is needed in order to manage mesh sensitivity within acceptable limits especially for the indentation.

# Conclusion and Recommendation

## 6-1 Conclusion

The failure behavior of ceramics with special emphasis on cone cracking is the subject of the thesis. Simulated indentation by a suitable numerical model using JEM JIVE FEM library is proposed to be employed to understand failure by cone cracks. A numerical model provides insight into cone cracking and facilitates to investigate the effects of key parameters such as internal friction, dilatancy and softening. A number of material models are available to study ceramic failure. The Drucker Prager (DP) model, which was developed for the study of failure behavior of rock and soil, is employed in present work on two considerations. One, it is easy to use and implement in FEM framework and two, ceramic is also a brittle material like rock and soil. It also considers the effect of plasticity flow and the strength of the comminuted particles, which are relevant to ceramic also. Verification of model is carried out through simulation of unit cubes subjected to unidirectional loads subjected prescribed displacements.

The DP model formulation is based on the assumption that softening is pressure independent unlike pressure dependent softening observed in ceramics. Furthermore, material strength keeps on increasing without limit with the rise in pressure as per DP yield function. But ceramic has finite strength like any other real material. In order to overcome these limitations of the DP model, suitable modifications are required to be incorporated in its formulation. It was also observed during the studies that the results are mesh sensitive. Viscoplasticity, which was found to overcome mesh sensitivity by scholars working on numerical modeling in the past, is integrated to the standard DP model in order to find a solution. The following is summary of the major conclusions of the present thesis

1. Parametric Study: The effects of material parameters e.g. friction angle, dilatancy and softening were extensively studied by simulating indentation through Standard DP Model. The indentation depth is 40  $\mu\text{m}$  unless specified otherwise. The major findings are as under:

- (a) Well developed cone cracks were observed at friction angles greater than or equal to  $60^{\circ}$ . Cone crack grows with increase in the angle of friction,
- (b) Cone crack formation stops at dilatancy angles greater than  $20^{\circ}$ . It decreases to  $16^{\circ}$  corresponding to lower indentation depth of  $25 \mu\text{m}$ . Cracks grew in size at smaller dilatancies. The cracks were found to be large at zero dilatancy indicating instantaneous failure.
- (c) Increase in softening stimulates the crack formation and its propagation,
- (d) The increase in confinement reduced crack formation,
- (e) Convergence could not be achieved for very small mesh sizes as well as for large values of softening and
- (f) The simulations were also found to be mesh sensitive.

Ceramic having low friction angle and softening modulus coupled with high dilatancy under confined conditions is less prone to cone cracking and suitable for armor protection.

2. Pressure Dependent Softening: Ceramic undergoes non linear rapid degradation of strength post-elastic limit. This is suggestive of softening behavior of ceramic being pressure dependent. The prescribed displacement corresponding to complete strength loss under pressure dependent softening is more than that for pressure independent softening. Crack formation during indentation is delayed in the pressure-dependent regime of softening. Thus the pressure dependent softening nature of ceramic has positive influence on its ability to become good material for armor protection.
3. Yield Function with procedure to limit material strength: A limiting feature was applied to the yield function adopted in Standard DP model to restrict compressive strength to a finite value in conformity with the strength of real materials. Limiting the yield function to the value of failed material (DP1) completely stopped crack initiation and propagation. However, the zone of compressive plastic strain below indenter grew in size and is indicative of compressive failure of material.
4. Mesh Sensitivity: The integration of viscoplasticity with standard DP model overcomes the mesh sensitivity to a large extent, and produces acceptable results for the tension bar. There is consistency in the cone crack size during indentation at variable mesh divisions but crack shapes vary. It is concluded that integration of viscoplasticity to the standard DP model is a positive step in mitigating mesh sensitivity. Further study is needed in order to manage mesh sensitivity within acceptable limits especially for the indentation.

## 6-2 Recommendation

1. Development of a DP formulation as a single integrated model capturing the effects of pressure dependent softening, finite material strength and viscoplasticity to study cone cracks.

2. Explore DP model for dynamic indentation of ceramics to study complex failure parameters like dwell, strain energy absorption, erosion of material, etc.
3. The integration of viscoplasticity was found to be promising for solving the mesh sensitivity. This aspect needs to be investigated in more detail to minimize the effect of mesh sensitivity within manageable limits.
4. An alternate stress driven formulation based on works by Aliguer, Carol and Ignasi [35] can be probed to improve the robustness of the model.



---

# Bibliography

- [1] B. Lawn and R. Wilshaw, "Indentation fracture: principles and applications," *Journal of materials science*, vol. 10, no. 6, pp. 1049–1081, 1975.
- [2] J. Chen, "Indentation-based methods to assess fracture toughness for thin coatings," *International Journal of physics*, 2012.
- [3] V. S. Deshpande, E. Gamble, B. G. Compton, R. M. McMeeking, A. G. Evans, and F. W. Zok, "A constitutive description of the inelastic response of ceramics," *Journal of the American Ceramic Society*, vol. 94, no. s1, 2011.
- [4] A. Lamberts, "Numerical simulation of ballistic impact on ceramic materials," Master's thesis, Eindhoven University of Technology, 2007.
- [5] "ppt - finite element analysis of contact problem."
- [6] *Non-linear Finite Element Analysis of Solids and Structures* by M. A. Crisfield. JOHN WILEY and SONS, 2000.
- [7] *Computational methods for plasticity* by EA de Souza Neto, D Peric and DRJ Owen. JOHN WILEY and SONS, 2008.
- [8] J. Walker and C. Anderson, "An analytical model for ceramic-faced light armour," *Int. Symp. on Ballistics*, vol. 3, no. 289-298, 1996.
- [9] C. E. Anderson Jr, "A review of computational ceramic armor modeling," *Proceedings of the 30*, 2007.
- [10] E. Carton, G. Roebroeks, J. Weerheijm, A. Diederer, and M. Kwint, "Tno's research on ceramic based armor," in *Advances in Ceramic Armor XI: A Collection of Papers Presented at the 39th International Conference on Advanced Ceramics and Composites*, pp. 1–18, John Wiley & Sons, Inc., 2015.
- [11] J. C. LaSalvia and J. W. McCauley, "Inelastic deformation mechanisms and damage in structural ceramics subjected to high-velocity impact," *International journal of applied ceramic technology*, vol. 7, no. 5, pp. 595–605, 2010.

- [12] G. Anstis, P. Chantikul, B. R. Lawn, and D. Marshall, "A critical evaluation of indentation techniques for measuring fracture toughness: I, direct crack measurements," *Journal of the American Ceramic Society*, vol. 64, no. 9, pp. 533–538, 1981.
- [13] "Cermics - wikipedia."
- [14] *Ceramic Innovations in the 20th century*. The American Ceramic Society, 1999.
- [15] R. F. Cook and G. M. Pharr, "Direct observation and analysis of indentation cracking in glasses and ceramics," *Journal of the American Ceramic Society*, vol. 73, no. 4, pp. 787–817, 1990.
- [16] G. R. J. Timothy J. Holmquist, "A improved computational model for brittle materials," *International Journal of Applied Ceramic Technology*, 1996.
- [17] T. J. Holmquist and G. R. Johnson, "Characterization and evaluation of silicon carbide for high-velocity impact," *Journal of applied physics*, vol. 97, no. 9, p. 093502, 2005.
- [18] L. Mishnaevsky Jr, "Physical mechanisms of hard rock fragmentation under mechanical loading: a review," in *International journal of rock mechanics and mining sciences & geomechanics abstracts*, vol. 32, pp. 763–766, Elsevier, 1995.
- [19] P.-A. Lindqvist, *Rock fragmentation by indentation and disc cutting: some theoretical and experimental studies*. PhD thesis, Luleå tekniska universitet, 1982.
- [20] L. Mishnaevsky, "A brief review of soviet theoretical approaches to dynamic rock failure," *INTERNATIONAL JOURNAL OF ROCK MECHANICS AND MINING & GEOMECHANICS ABSTRACTS*, vol. 30, no. 6, 1993.
- [21] D. C. Drucker and W. Prager, "Soil mechanics and plastic analysis or limit design," *Quarterly of applied mathematics*, vol. 10, no. 2, pp. 157–165, 1952.
- [22] G. d. S. M. Hjjaj, J. Fortin b, "A complete stress update algorithm for the non-associated druckerprager model including treatment of the apex," *International Journal of Engineering Science*, vol. 41, no. 1109-1143, 2002.
- [23] K. O. . Mijangos, "Drucker-prager finite element constitutive model of microindentation in polycrystalline alumina," *SEM Annual Conference*, 2009.
- [24] F. Z. E.A. Gamble, B.G. Compton, "Impact response of layered steelalumina targets," *Journal of Mechanics of Materials*, vol. 60, no. 80-92, 2013.
- [25] A. A. W. Timothy J. Holmquist, "Using hertzian indentation to understand the strength and ballistic resistance of silicon carbide," *International Journal of Applied Ceramic Technology*, vol. 7, no. 5, 2010.
- [26] T. J. Holmquist, "Modelling spherical indentation experiments onto silicon carbide," *International Journal of Applied Ceramic Technology*, 2005.
- [27] R. L. Woodward, "A basis for modelling ceramic composite armour defeat," tech. rep., MATERIALS RESEARCH LABS ASCOT VALE (AUSTRALIA), 1989.

- 
- [28] X. Chen, *Investigation on the impact damage of glass using the combined finite/discrete element method*. PhD thesis, University of Birmingham, 2013.
- [29] T. J. Holmquist, “Some observations on the strength of failed ceramic,” in *Advances in Ceramic Armor: A Collection of Papers Presented at the 29th International Conference on Advanced Ceramics and Composites, Jan 23-28, 2005, Cocoa Beach, FL*, vol. 296, p. 3, John Wiley & Sons, 2009.
- [30] B. Lawn, *Fracture of brittle solids*. Cambridge university press, 1993.
- [31] D. S. Cronin, K. Bui, C. Kaufmann, G. McIntosh, T. Berstad, and D. Cronin, “Implementation and validation of the johnson-holmquist ceramic material model in ls-dyna,” in *4th European LS-dyna users conference*, pp. 47–59, 2003.
- [32] C. E. Anderson Jr and S. A. Royal-Timmons, “Ballistic performance of confined 99.5%-al203 ceramic tiles,” *International journal of impact engineering*, vol. 19, no. 8, pp. 703–713, 1997.
- [33] W. Wang, L. Sluys, and R. De Borst, “Viscoplasticity for instabilities due to strain softening and strain-rate softening,” *International Journal for Numerical Methods in Engineering* 40 (20), 3839-3864.(1997), 1997.
- [34] W. Wang and L. Sluys, “Formulation of an implicit algorithm for finite deformation viscoplasticity,” *International Journal of Solids and Structures*, vol. 37, no. 48, pp. 7329–7348, 2000.
- [35] I. Aliguer, I. Carol, and S. Sture, “Stress-driven integration strategies and m-agc tangent operator for perzyna viscoplasticity and viscoplastic relaxation: application to geomechanical interfaces,” *International Journal for Numerical and Analytical Methods in Geomechanics*, vol. 41, no. 6, pp. 918–939, 2017.

